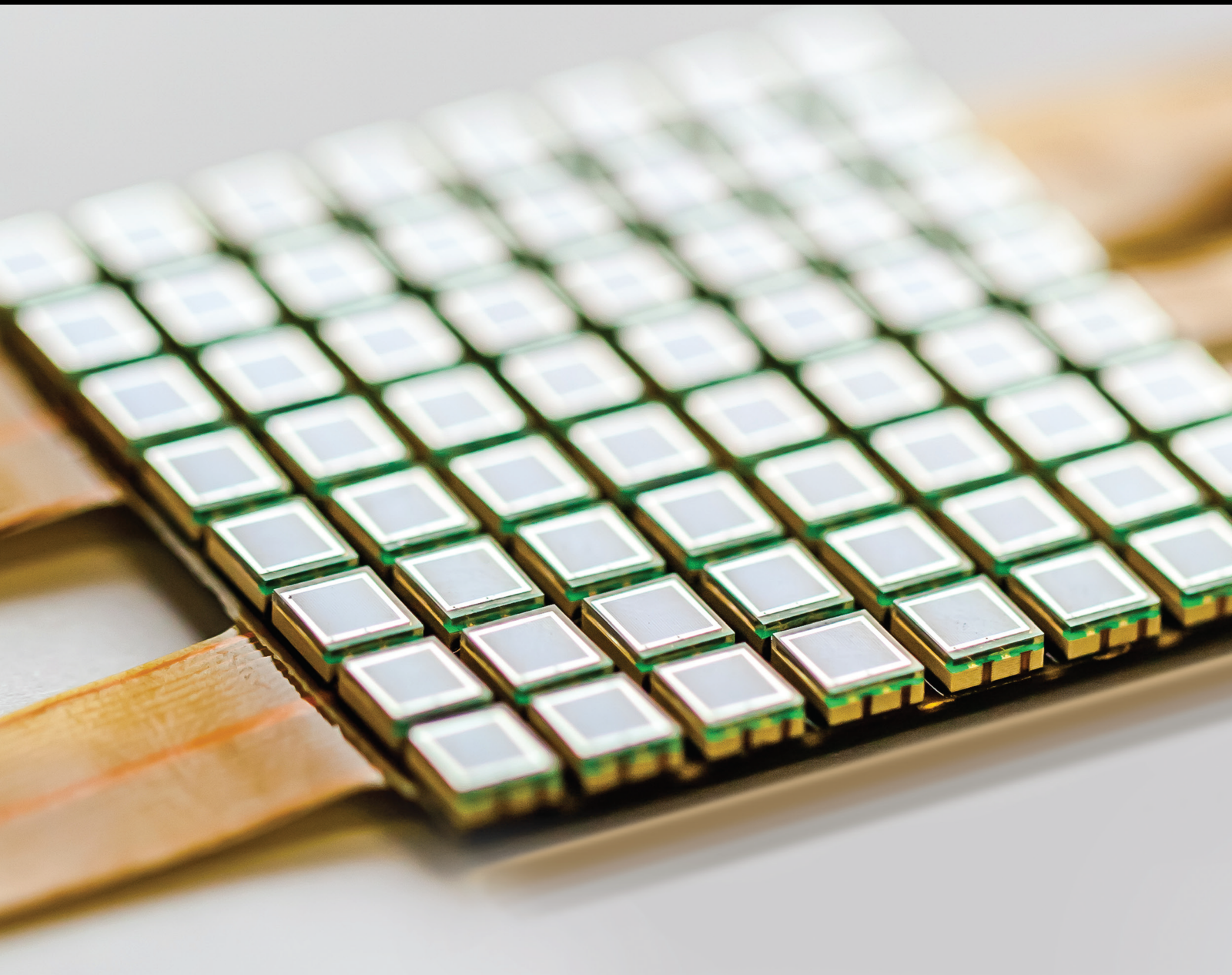


# New Developments in Ultrasonic Transducer Design and Sensing Technology

Lead Guest Editor: Nan Li

Guest Editors: Jiabin Jia and YAN LYU





---

# **New Developments in Ultrasonic Transducer Design and Sensing Technology**



Journal of Sensors

---

**New Developments in Ultrasonic  
Transducer Design and Sensing  
Technology**

Lead Guest Editor: Nan Li

Guest Editors: Jiabin Jia and YAN LYU



---




Copyright © 2022 Hindawi Limited. All rights reserved.

This is a special issue published in "Journal of Sensors." All articles are open access articles distributed under the Creative Commons Attribution License, which permits unrestricted use, distribution, and reproduction in any medium, provided the original work is properly cited.

# Chief Editor

Harith Ahmad , Malaysia

## Associate Editors

Duo Lin , China  
Fanli Meng , China  
Pietro Siciliano , Italy  
Guiyun Tian, United Kingdom

## Academic Editors

Ghufran Ahmed , Pakistan  
Constantin Apetrei, Romania  
Shonak Bansal , India  
Fernando Benito-Lopez , Spain  
Romeo Bernini , Italy  
Shekhar Bhansali, USA  
Matthew Brodie, Australia  
Ravikumar CV, India  
Belén Calvo, Spain  
Stefania Campopiano , Italy  
Binghua Cao , China  
Domenico Caputo, Italy  
Sara Casciati, Italy  
Gabriele Cazzulani , Italy  
Chi Chiu Chan, Singapore  
Sushank Chaudhary , Thailand  
Edmon Chehura , United Kingdom  
Marvin H Cheng , USA  
Lei Chu , USA  
Mario Collotta , Italy  
Marco Consales , Italy  
Jesus Corres , Spain  
Andrea Cusano, Italy  
Egidio De Benedetto , Italy  
Luca De Stefano , Italy  
Manel Del Valle , Spain  
Franz L. Dickert, Austria  
Giovanni Diraco, Italy  
Maria de Fátima Domingues , Portugal  
Nicola Donato , Italy  
Sheng Du , China  
Amir Elzwawy, Egypt  
Mauro Epifani , Italy  
Congbin Fan , China  
Lihang Feng, China  
Vittorio Ferrari , Italy  
Luca Francioso, Italy

Libo Gao , China  
Carmine Granata , Italy  
Pramod Kumar Gupta , USA  
Mohammad Haider , USA  
Agustin Herrera-May , Mexico  
María del Carmen Horrillo, Spain  
Evangelos Hristoforou , Greece  
Grazia Iadarola , Italy  
Syed K. Islam , USA  
Stephen James , United Kingdom  
Sana Ullah Jan, United Kingdom  
Bruno C. Janegitz , Brazil  
Hai-Feng Ji , USA  
Shouyong Jiang, United Kingdom  
Roshan Prakash Joseph, USA  
Niravkumar Joshi, USA  
Rajesh Kaluri , India  
Sang Sub Kim , Republic of Korea  
Dr. Rajkishor Kumar, India  
Rahul Kumar , India  
Nageswara Lalam , USA  
Antonio Lazaro , Spain  
Chengkuo Lee , Singapore  
Chenzong Li , USA  
Zhi Lian , Australia  
Rosalba Liguori , Italy  
Sangsoon Lim , Republic of Korea  
Huan Liu , China  
Jin Liu , China  
Eduard Llobet , Spain  
Jaime Lloret , Spain  
Mohamed Louzazni, Morocco  
Jesús Lozano , Spain  
Oleg Lupan , Moldova  
Leandro Maio , Italy  
Pawel Malinowski , Poland  
Carlos Marques , Portugal  
Eugenio Martinelli , Italy  
Antonio Martinez-Olmos , Spain  
Giuseppe Maruccio , Italy  
Yasuko Y. Maruo, Japan  
Zahid Mehmood , Pakistan  
Carlos Michel , Mexico  
Stephen. J. Mihailov , Canada  
Bikash Nakarmi, China



Ehsan Namaziandost , Iran  
Heinz C. Neitzert , Italy  
Sing Kiong Nguang , New Zealand  
Calogero M. Oddo , Italy  
Tinghui Ouyang, Japan  
SANDEEP KUMAR PALANISWAMY ,  
India  
Alberto J. Palma , Spain  
Davide Palumbo , Italy  
Abinash Panda , India  
Roberto Paolesse , Italy  
Akhilesh Pathak , Thailand  
Giovanni Pau , Italy  
Giorgio Pennazza , Italy  
Michele Penza , Italy  
Sivakumar Poruran, India  
Stelios Potirakis , Greece  
Biswajeet Pradhan , Malaysia  
Giuseppe Quero , Italy  
Linesh Raja , India  
Maheswar Rajagopal , India  
Valerie Renaudin , France  
Armando Ricciardi , Italy  
Christos Riziotis , Greece  
Ruthber Rodriguez Serrezuela , Colombia  
Maria Luz Rodriguez-Mendez , Spain  
Jerome Rossignol , France  
Maheswaran S, India  
Ylias Sabri , Australia  
Sourabh Sahu , India  
José P. Santos , Spain  
Sina Sareh, United Kingdom  
Isabel Sayago , Spain  
Andreas Schütze , Germany  
Praveen K. Sekhar , USA  
Sandra Sendra, Spain  
Sandeep Sharma, India  
Sunil Kumar Singh Singh , India  
Yadvendra Singh , USA  
Afaque Manzoor Soomro , Pakistan  
Vincenzo Spagnolo, Italy  
Kathiravan Srinivasan , India  
Sachin K. Srivastava , India  
Stefano Stassi , Italy

Danfeng Sun, China  
Ashok Sundramoorthy, India  
Salvatore Surdo , Italy  
Roshan Thotagamuge , Sri Lanka  
Guiyun Tian , United Kingdom  
Sri Ramulu Torati , USA  
Abdellah Touhafi , Belgium  
Hoang Vinh Tran , Vietnam  
Aitor Urrutia , Spain  
Hana Vaisocherova - Lislalova , Czech  
Republic  
Everardo Vargas-Rodriguez , Mexico  
Xavier Vilanova , Spain  
Stanislav Vitek , Czech Republic  
Luca Vollero , Italy  
Tomasz Wandowski , Poland  
Bohui Wang, China  
Qihao Weng, USA  
Penghai Wu , China  
Qiang Wu, United Kingdom  
Yuedong Xie , China  
Chen Yang , China  
Jiachen Yang , China  
Nitesh Yelve , India  
Aijun Yin, China  
Chouki Zerrouki , France

## Contents







---

### **Guided Wave Focusing Imaging Detection of Pipelines by Piezoelectric Sensor Array**

Song Guorong, Bian Ce, Lyu Yan , Li Yang, Yang Jing, Zheng Lei, and He Cunfu

Research Article (14 pages), Article ID 4731341, Volume 2022 (2022)

### **Ultrasonic Testing of Carbon Fiber-Reinforced Polymer Composites**

Bocheng Wang , Pengju He , Yingnan Kang , Jiabin Jia , Xin Liu , and Nan Li 

Review Article (20 pages), Article ID 5462237, Volume 2022 (2022)

### **A Method Applied in Anomaly Detection of Impurities Adhering to Pipes of Coriolis Mass Flowmeter**

Jianxin Ren , Yixin Qin , Peng Yang , and Peng Zhang


Research Article (11 pages), Article ID 9376885, Volume 2022 (2022)

### **Shape Reconstruction of Eccentric Defect in Cylindrical Component by Modified Born Approximation Method**

Gangfeng Zheng , Ze Li , Songfeng Liu , Hao Dong , Bin Wu , and Cunfu He 

Research Article (6 pages), Article ID 3142637, Volume 2022 (2022)

### **Optimization of Damage Equivalent Accelerated Test Spectrum Derivation Using Multiple Non-Gaussian Vibration Data**

Fei Xu , Kjell Ahlin, and Binyi Wang

Research Article (14 pages), Article ID 3668726, Volume 2021 (2021)

## Research Article

# Guided Wave Focusing Imaging Detection of Pipelines by Piezoelectric Sensor Array

Song Guorong,<sup>1</sup> Bian Ce,<sup>1</sup> Lyu Yan ,<sup>1</sup> Li Yang,<sup>2</sup> Yang Jing,<sup>3</sup> Zheng Lei,<sup>3</sup> and He Cunfu<sup>1</sup>

<sup>1</sup>Faculty of Materials and Manufacturing, Beijing University of Technology, Beijing, China

<sup>2</sup>Guobiao (Beijing) Testing & Certification Co. Ltd., Beijing, China

<sup>3</sup>Beijing Aerospace Measurement & Control Technology Co. Ltd., Beijing, China

Correspondence should be addressed to Lyu Yan; [lyuan@bjut.edu.cn](mailto:lyuan@bjut.edu.cn)

Received 19 March 2022; Revised 13 July 2022; Accepted 25 July 2022; Published 1 September 2022

Academic Editor: Abdellah Touhafi

Copyright © 2022 Song Guorong et al. This is an open access article distributed under the Creative Commons Attribution License, which permits unrestricted use, distribution, and reproduction in any medium, provided the original work is properly cited.

The sensor array-based guided wave focusing detection method can effectively improve the detection sensitivity of defects and realize the visual imaging. In this research, the three-dimensional finite element simulation model of stainless steel pipeline for guided wave focusing detection was established, and the  $L(0, 2)$  mode of guided wave was excited by applying a load on the end surface of the pipeline. And in the experiment, the excitation and reception of  $L(0, 2)$  mode guided waves on the outer surface of the stainless steel pipeline were realized by the piezoelectric transducer array. A 16-channel guided wave focusing experimental system was integrated to conduct the defect detection experiments on a stainless steel pipe with diameter of 140 mm and wall thickness of 5 mm. The total matrix data acquisition was performed, and then the amplitude total focusing (TFM) imaging and sign coherence factor (SCF) imaging of the pipe were realized. In this way, the experimental results showed that the pipeline defect detection method and the system proposed in this research can achieve the longitudinal and circumferential positioning and imaging of defects, like holes and scratches.

## 1. Introduction

Ultrasonic guided waves using sensor arrays can improve the resolution of defect detection. Combining the total focusing method (TFM), the longitudinal and circumferential positioning of defects can be achieved precisely in a large range [1]. Moreover, the sensor array can locate multiple defects at the same time, which can solve the problem of identifying scratch defects smaller than half a wavelength [2]. A phased array system controls every element in the array to excite and receive ultrasonic waves according to a certain time delay. The beam can be focused in any point of a testing structure, which can improve the capability of detecting small defects [3].

The existing ultrasonic guided wave detections usually achieve axial positioning of pipeline defects through the A-sweep signals and cannot determine the circumferential location or the number of defects in the circumferential direction. Detection of pipeline circumferential defects usually requires a sweep of the entire pipeline [4]. Li et al. [5]

achieved the monitoring of bubble flow inside opaque pipes by sensor arrays. In terms of focusing detection of pipelines, Rose and Paul [6] proposed an ultrasonic guided wave focusing principle to detect defects in pipelines. Mu et al. [7] compared theoretical calculations with finite element simulations to validate the idea of guided wave focusing in pipelines and demonstrated that guided wave focusing can improve the circumferential resolution of defects through a commercial phase-controlled system. Wu et al. [8] proposed a virtual phase-controlled focusing method to achieve focusing detection of pipeline defects, which improved the detection capability of ultrasonic guided waves for defects, but their experiments used multiple switching to equate the effect of multichannel devices, which is a tedious process. The conventional ultrasonic detection methods have low sensitivity for scratch defects [9].

In terms of the total focusing method, Holmes et al. [10] first proposed a total focus algorithm that was superior to the sensor array sweep and was able to perform virtual focus detection for each point of the grid, but the experiment



required multiple devices for signal excitation and acquisition, and surely, the operation process was much tedious. Jie et al. [11] quantitatively analyzed the effect of varying array element parameters (amplitude, phase, and time delay) on the quality of TFM imaging. He et al. [12] used a ring-shaped electromagnetic sensor array consisting of eight sensors that were excited to generate a single A0 mode Lamb wave at low frequencies; using the total focusing method, they achieved fast large-area detection of plate-like structures by Lamb waves. Camacho et al. [13] first proposed a phase imaging algorithm by defining a phase coherence factor and a sign coherence factor, respectively, weighted the synthesized output to achieve the suppression of the side and gate flaps, and finally improved the signal-to-noise ratio. Prado et al. [14] used the sign coherence factor (SCF) for the weighted processing of total focusing imaging and proposed a composite imaging method by single mode Lamb wave for plate structures. Liu et al. [15] used the advantage of all-round detection of dense piezoelectric transducer array and combined the composite imaging method of TFM and SCF to achieve the multiple defect images. The experiments used a single channel system for total matrix signal acquisition, which would be not efficient. Lyu et al. [16] designed a high-voltage excitation of multichannel tone-burst signal with synchronous signal acquisition. Experiments are conducted by the developed multichannel system and the piezoelectric linear array. Guided wave phased array and the total focusing imaging algorithm are demonstrated on a 1 mm aluminum plate.

In this research, a 16-channel guided wave focusing detection system was developed to implement the total matrix data acquisition experiment on the pipeline, and then the total focusing imaging algorithm and sign coherence factor imaging algorithm were manipulated to realize the focusing imaging of multiple pipeline defects.

## 2. Mode Selection and Simulation Analysis

**2.1. Mode Selection.** A stainless steel pipe was adopted in the experiment, with a length of 2000 mm, inner diameter of 130 mm, and wall thickness of 5 mm, as shown in Figure 1, in which the density is  $7.932 \text{ g/cm}^3$ , the longitudinal wave speed is 5960 m/s, and the transverse wave speed is 3260 m/s. The axisymmetric longitudinal mode dispersion curves were calculated based on the above fundamental parameters. The group velocity dispersion curves are demonstrated in Figure 2.

The  $L(0, 2)$  or  $L(0, 1)$  mode exhibits almost no dispersion in the lower frequency range, and  $L(0, 2)$  possesses faster propagation speed, which will be distinct in time domain to avoid the complex echoes, and then benefits the following signal analysis. Therefore, both simulation and experiment utilized the  $L(0, 2)$  mode for the detection. The excitation frequency range was between 80 kHz and 200 kHz according to the above dispersion curve.

**2.2. Wave Excitation and Simulation.** A finite element model of the pipeline was established in ABAQUS (Dassault Systemes SIMULIA), according to the actual parameters of the

specimen used in Section 2.1. The material parameters of the stainless steel are shown in Table 1. And the excitation signal was set to a Hanning windowed 5-period sinusoidal signal with a central frequency of 108 kHz to match the piezoelectric transducer.

The simulation model is calculated using dynamic explicit analysis step, the sampling duration is set to  $1000 \mu\text{s}$ , which is sufficient for the  $L(0,2)$  mode guided wave to propagate to the rear half of the pipe, the sampling points are set to 10000 points, the sampling frequency is 10 MHz at this time, the output variable of the output node is set to displacement, and the displacement direction is set to  $y$  direction, which is used to extract the vibration of the mass point in the vertical pipe axial direction, i.e., the  $L(0,2)$  mode vibration direction of the guided wave. A hexahedral structured network is used to mesh the pipe model, and the mesh size is set to 1.5 mm to meet the requirement that the mesh size is less than one-eighth of the wavelength.

To excite the longitudinal mode, the excitation region of displacement load was applied and divided in 16 elements at the end surface of the pipe, and the loading is along the axial direction of the pipe. The obtained diagram of wave propagation in the pipe is shown in Figure 3, and the fastest guided wave velocity obtained after calculation is 5040.9 m/s, which coincides with the corresponding  $L(0, 2)$  mode guided wave velocity of 5113.3 m/s in the dispersion curve. It can be determined that the above excitation method can generate  $L(0, 2)$  mode guided waves propagating axially along the pipe and can be used for pipe defect detection. The wavelength of this mode wave in the pipe is 46.7 mm.

A model of the pipe with two artificial through-holes was established. In the center of the pipe, we set two artificial through-holes with a diameter of 7 mm, 16 piezoelectric sensors along the circumference of the pipe were uniformly distributed on the surface of one end of the pipe, and the interval between each sensor was 27.48 mm. The sensor array distribution and the location of the defects are shown in Figure 4.

The ultrasonic excitation started from CH1 to CH16 one by one counterclockwise, and in every excitation, all the sensors will receive its own echoes.

The simulation was carried out in the way of 1 channel excitation and 16 channel reception. Totally, 16 sets of data were obtained, and finally, a data matrix  $[M]$  of  $16 \times 16 \times n$  ( $n$  is the number of data point in one time history) points data were constructed. Taking the excitation by CH5 for example, the 16 sets of echoes obtained are shown in Figure 5. We can see that the first-channel excitation produced the highest initial wave amplitude when received by itself, and the circumferential wave is included. However, we cannot find any axial echoes with the defect information at all.

Above all, from the simulation results, it can be seen that the excited waves by CH5, which is closest to one of the defect, could not find the defect echoes, even though it has the most significant signal by its channel. Therefore, it was necessary to use the matrix data to improve the resolution of defect echoes. And the total focusing method will be adopted to visualize and locate the defects accordingly.

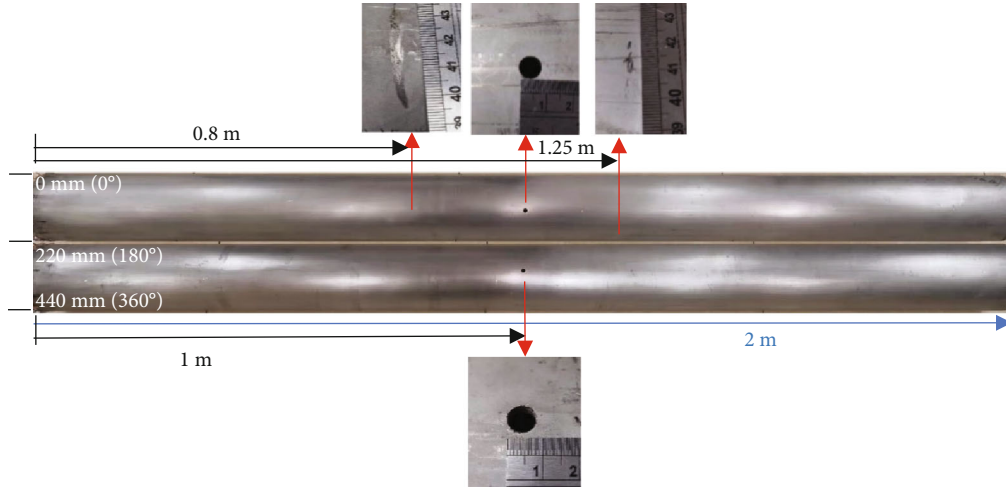


FIGURE 1: Diagram of pipeline under test.

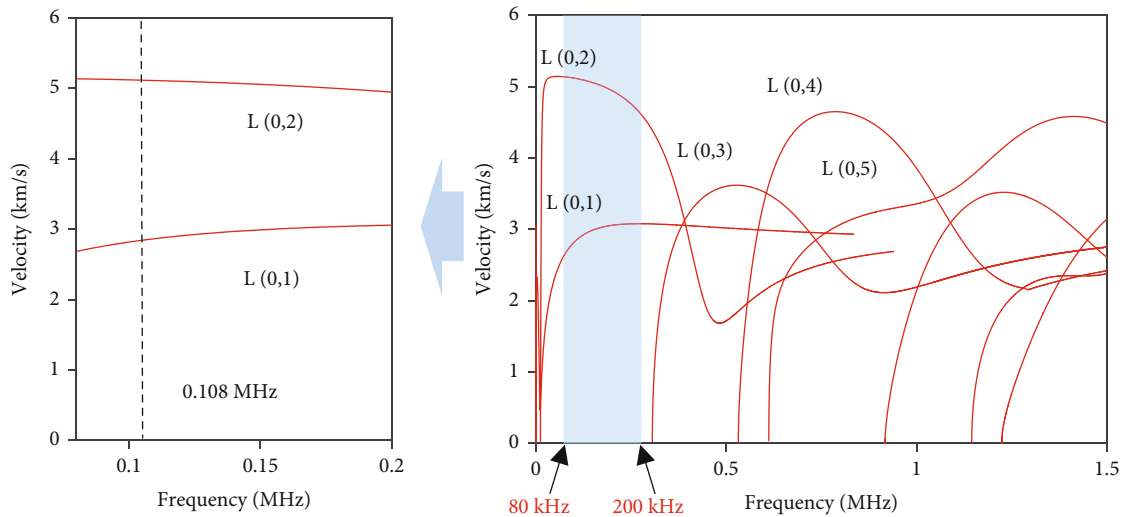


FIGURE 2: Group velocity of longitudinal modes.

TABLE 1: Stainless steel pipe material parameters.

Density	Poisson's ratio	Elastic modulus
7932 kg/m <sup>3</sup>	0.30	193 GPa

### 3. Array Sensor Imaging

The total focusing method is a virtual focus postprocessing imaging technique based on total matrix data, which is divided into two main parts: total matrix data acquisition and total focusing imaging [17, 18].

An array of 16 sensors was mounted on the end surface of the pipe, so we will have 16 echoes for each exciting element. And then, the 16 × 16 echo signals are obtained for total focusing imaging. It should be noted that the image of the pipe will be unrolled to plane view, in which a Cartesian coordinate system is established. The image plane is discretized into a grid, shown in Figure 6. The total focusing

algorithm uses the  $[M]$  matrix data to achieve point focusing imaging of all discrete points in grid. As shown in Figure 6, where  $P$  is the time amplitude information.  $P$  is the  $A$  scan waveform of each channel signal composed of time and amplitude, and the amplitude information of each virtual focus is obtained by wave speed and crossing time according to the coordinates of each virtual focus. The signal amplitude of all ultrasonic echo signals at that point is solved according to the distance of each array element to that point, and the amplitude values are superimposed to obtain the amplitude of that point, and then the above process is repeated to obtain the amplitude information of all focus points [19].

The flow chart of total focus imaging algorithm is shown in Figure 7(a). The parameters are set as follows:  $N = 16$ , pitch = 27.5 mm,  $f = 108000$  Hz,  $F_s = 1/5000000$  s,  $c = 5011$  m/s,  $H = 1500$  mm,  $L = 440$  mm, step $X = 1$  mm, and step $Y = 1$  mm.

The SCF imaging on the basis of total focus imaging, in addition to using the amplitude information in the matrix

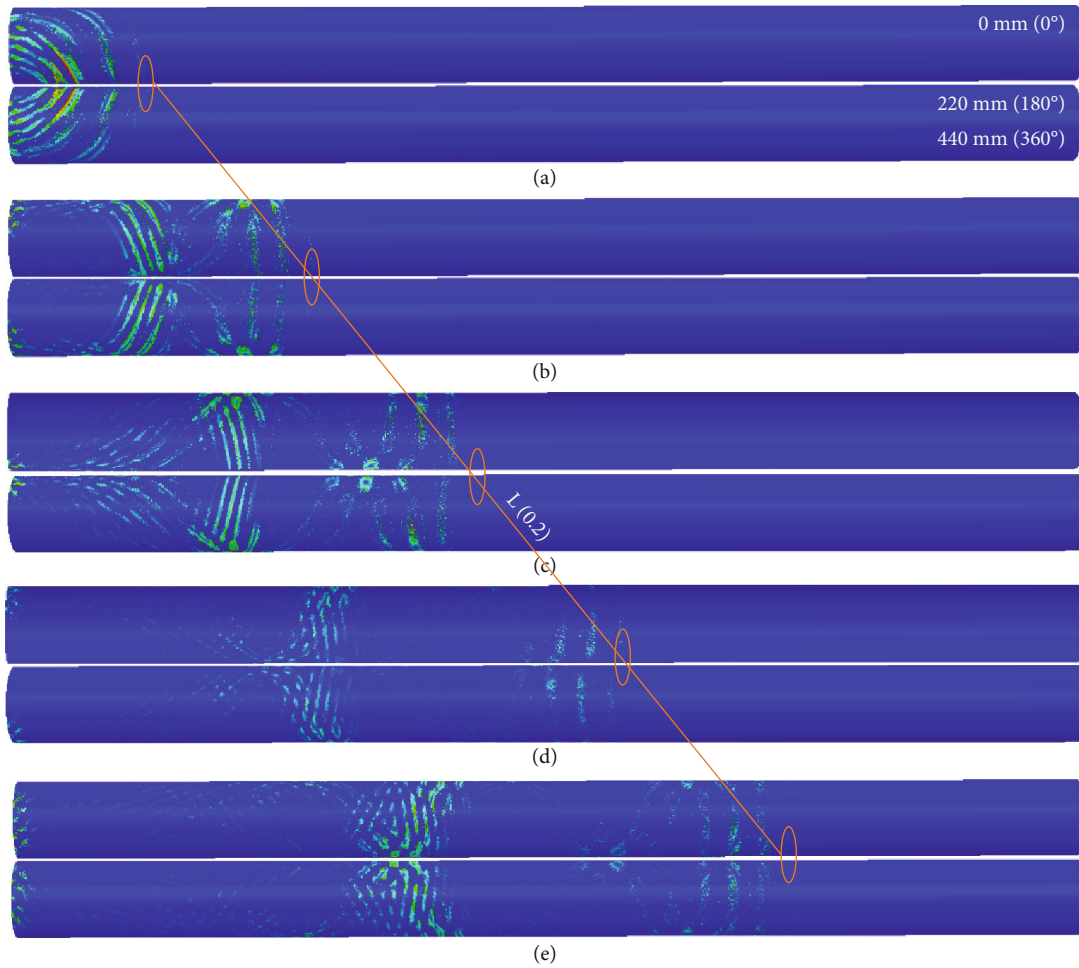


FIGURE 3: Pipeline guided wave propagation at (a)  $t = 60 \mu\text{s}$ , (b)  $t = 120 \mu\text{s}$ , (c)  $t = 180 \mu\text{s}$ , (d)  $t = 240 \mu\text{s}$ , and (e)  $t = 300 \mu\text{s}$ .

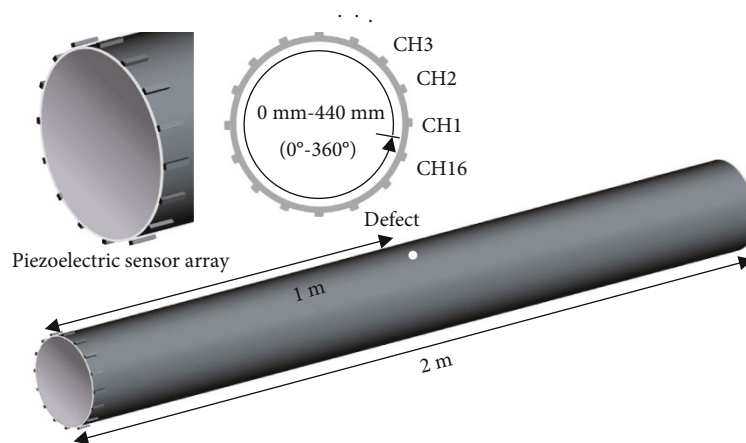


FIGURE 4: Sensor distribution and sensor position diagram.

data, also introduces the phase information of the signal into the algorithm. This method overcomes the susceptibility of the signal amplitude to noise and interference from the side and gate flaps and effectively suppresses the effect of the inconsistent directivity of the acoustic beam on the imaging

quality [13], improving the contrast and signal-to-noise ratio of the imaging.

Among the proposed phase imaging methods, the sign coherence factor imaging algorithm has better detection results in defect localization, and the sign coherence factor



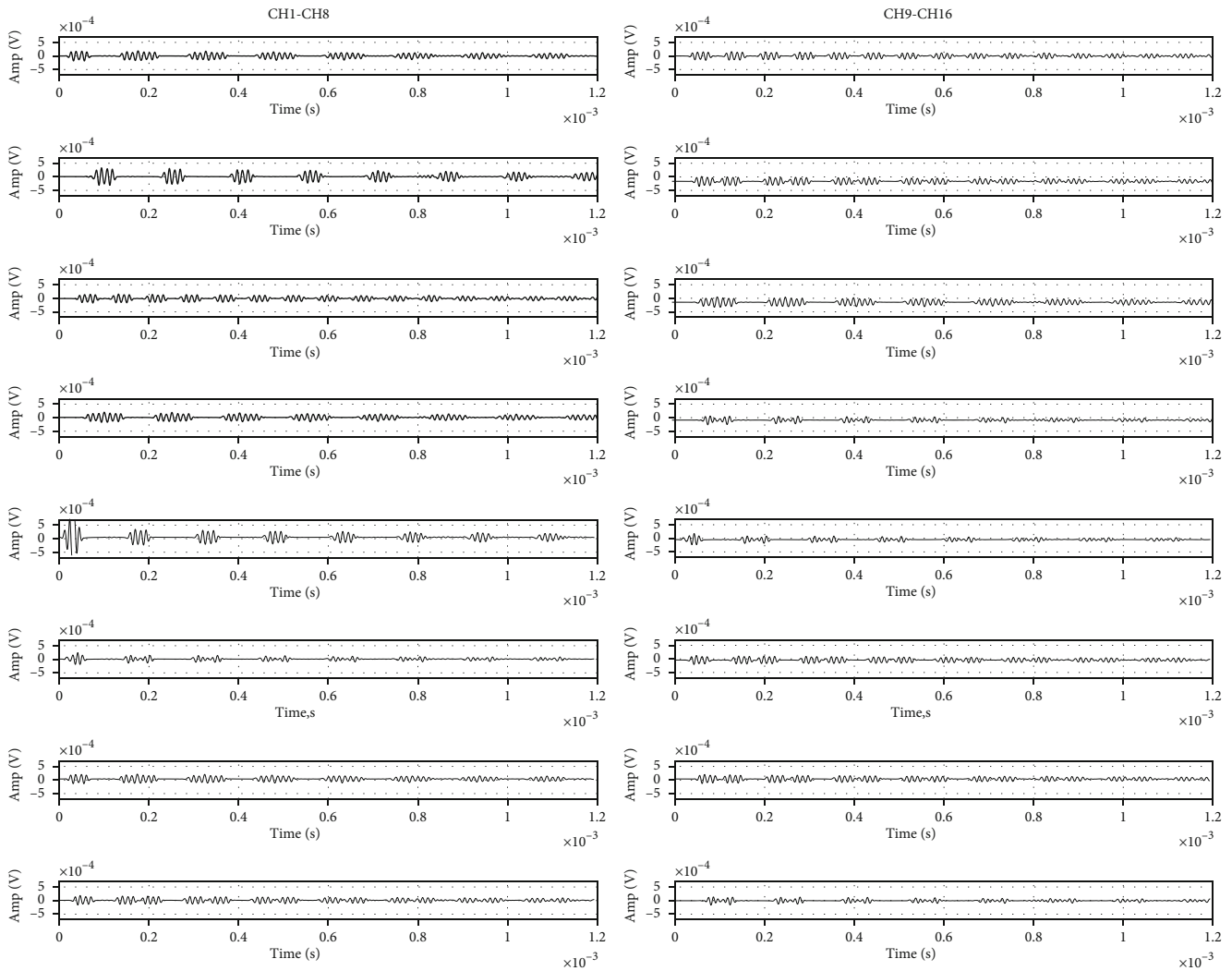


FIGURE 5: Waveforms received by 16 channels after excitation by CH5.

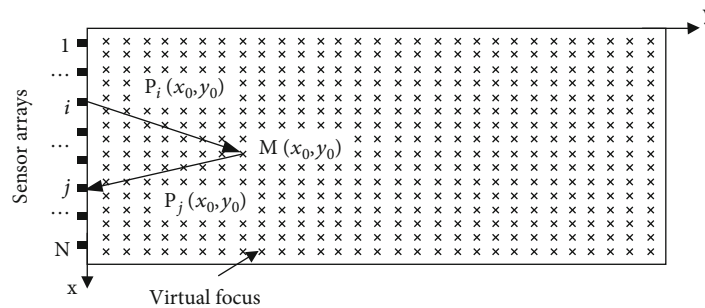


FIGURE 6: Schematic diagram of total focus imaging algorithm.

imaging is a method analyzing the variance of the signal symbol polarity [15]. The flow chart of sign coherence factor imaging is shown in Figure 7(b). The parameters are set as follows:  $N = 16$ ,  $\text{pitch} = 27.5 \text{ mm}$ ,  $f = 108000 \text{ Hz}$ ,  $F_s = 1/5000000 \text{ s}$ ,  $c = 5011 \text{ m/s}$ ,  $H = 1500 \text{ mm}$ ,  $L = 440 \text{ mm}$ ,  $\text{step}X = 1 \text{ mm}$ , and  $\text{step}Y = 1 \text{ mm}$ .

The total focusing method was used to image the total matrix data obtained from the simulation as shown in Figure 8.

Sign coherence factor imaging was performed on the basis of the total focusing method, as shown in Figure 9.

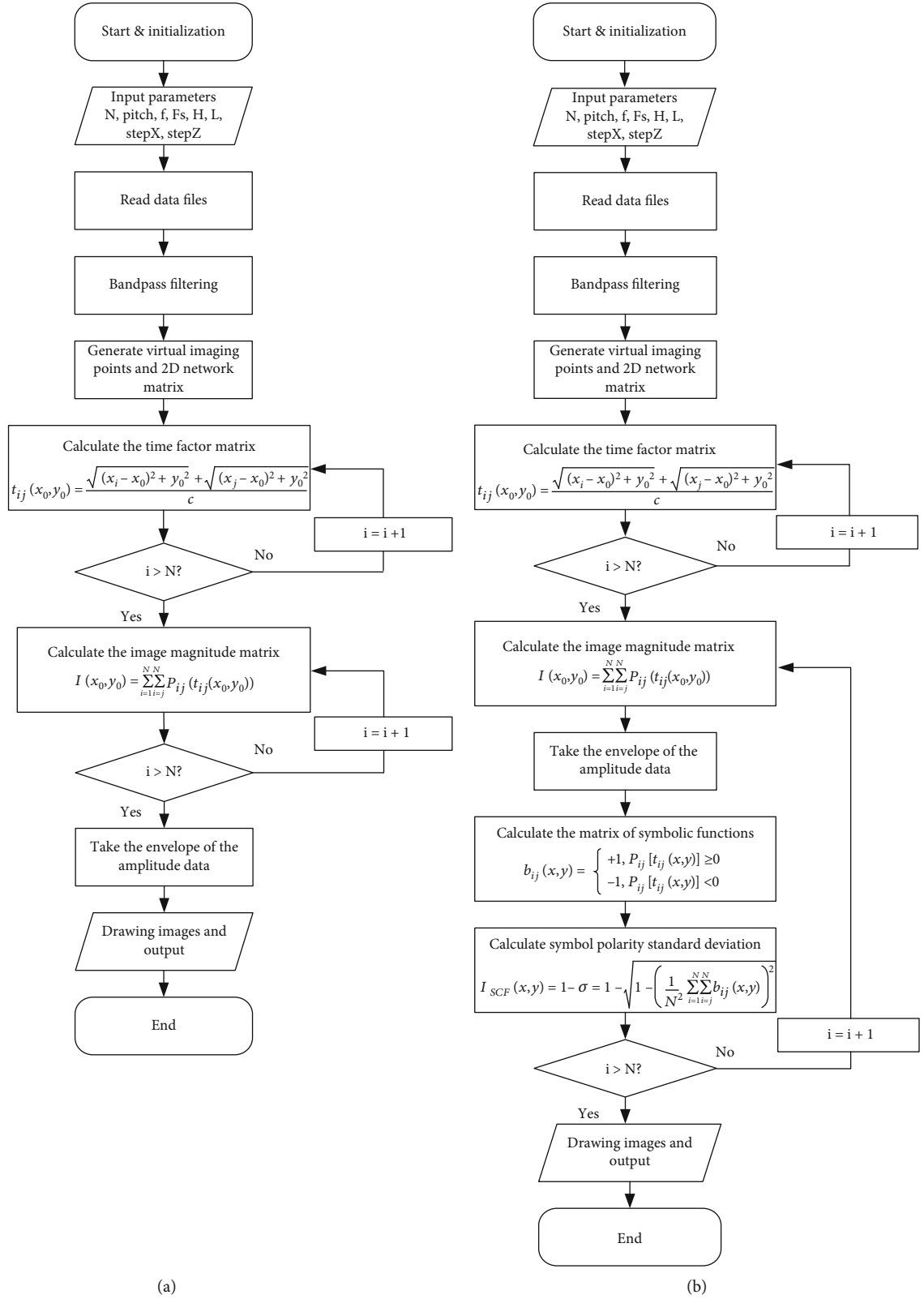


FIGURE 7: Flow chart of total focus and sign coherence factor imaging (a) total focus and (b) sign coherence factor.

The imaging resolution was set to 1 mm, and the imaging results were thresholded at 80% to remove noise artifacts and performed time windowing from  $98 \mu\text{s}$  to  $314 \mu\text{s}$ , corre-

sponding to a region in the image of 250 mm to 800 mm. However, due to the guided wave also propagating along the circumference of the pipe in the simulation, the

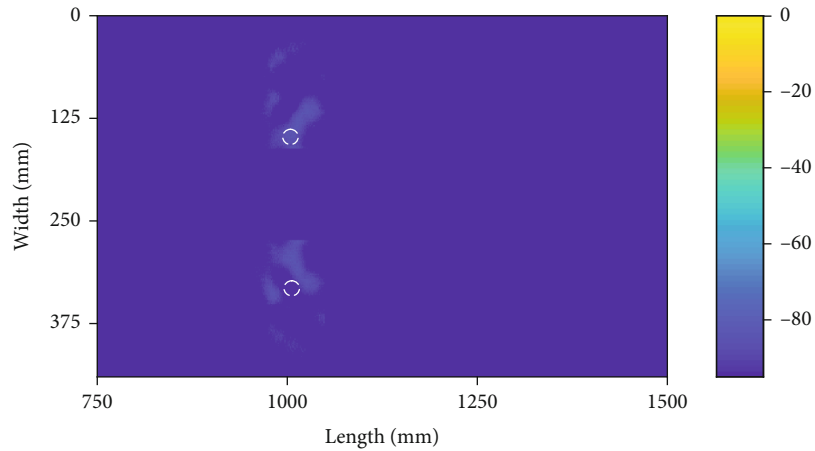


FIGURE 8: Simulation results of pipeline full focus imaging.

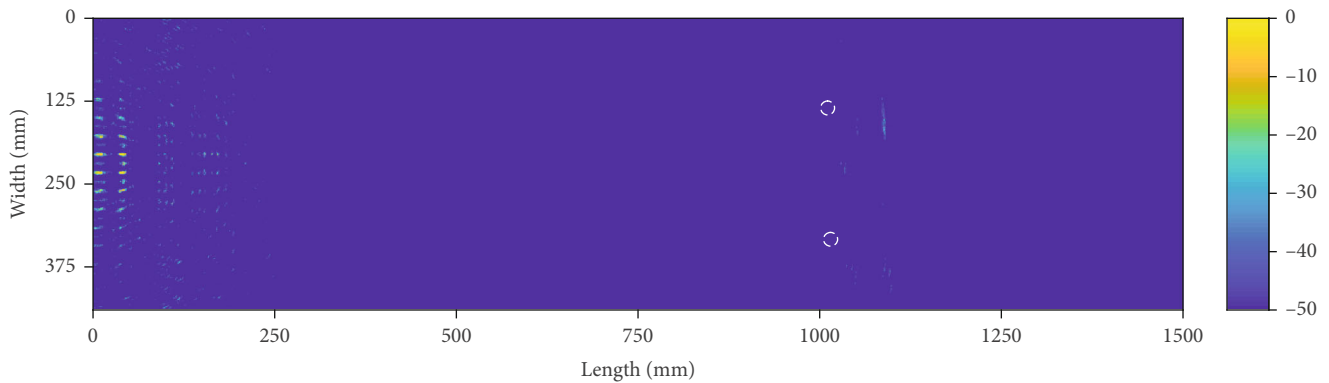


FIGURE 9: Simulation results of pipeline sign coherence factor.

amplitude is large, which has a relatively large impact on the results. From the obtained image (the white circle is the actual location of the defect), it can be seen that the artificial through-hole set in the middle of the pipe was detected, and the location information of the defect was consistent with the set model. The sign coherence factor imaging was better than the total focusing method.

Therefore, through the sensor array-based pipeline guided-wave, the total focus method could obtain more accurate location information of multiple defects in metal pipes, which verified the theory of using the total focus imaging method and sign coherence factor imaging, and then guided for the subsequent experiments.

#### 4. Sensor Array Excitation/Acquisition System

To realize the multichannel total matrix data acquisition function, the multichannel ultrasonic excitation and acquisition system was designed, which can realize 16 channel ultrasonic signal excitation and synchronous signal acquisition and can support up to 16 channel of rotating excitation or phase-controlled excitation. The 16 receiving channels can be used synchronously or independently, which can realize total focusing imaging detection. The system equipment adopts a dual 220 V AC power supply, and the excita-

tion voltage can reach up to  $180 V_{pp}$  peak-to-peak, which can realize the sinusoidal signal excitation with 5-cycle Hanning window modulation. The sampling signal gain is 0-42 dB, which can be adjusted online. Data is transferred via USB2.0 and through the host computer for excitation acquisition, parameter adjustment, and data storage. Figure 10 shows the appearance of the device. The basic parameters of the equipment indicators are shown in Table 2.

The system mainly includes multichannel signal synchronization acquisition module, multichannel guided wave signal excitation module, signal amplification module, power supply and data interface module, high-voltage linear power supply, and detection system host computer. Figure 11 shows the structure of the system.

The multichannel signal excitation module consists of 16 independent excitation channel and 16 independent signal amplification links. The excitation signal is realized by direct digital synthesis (DDS) technology for arbitrary waveform signal excitation, and this experiment needs to reduce the guided waveform dispersion phenomenon, so a 5-cycle Hanning window-modulated sinusoidal signal is used as the excitation signal, and the frequency can be adjusted online by the host computer. With signal amplification linked by the PA85 amplifier chip as the core device to



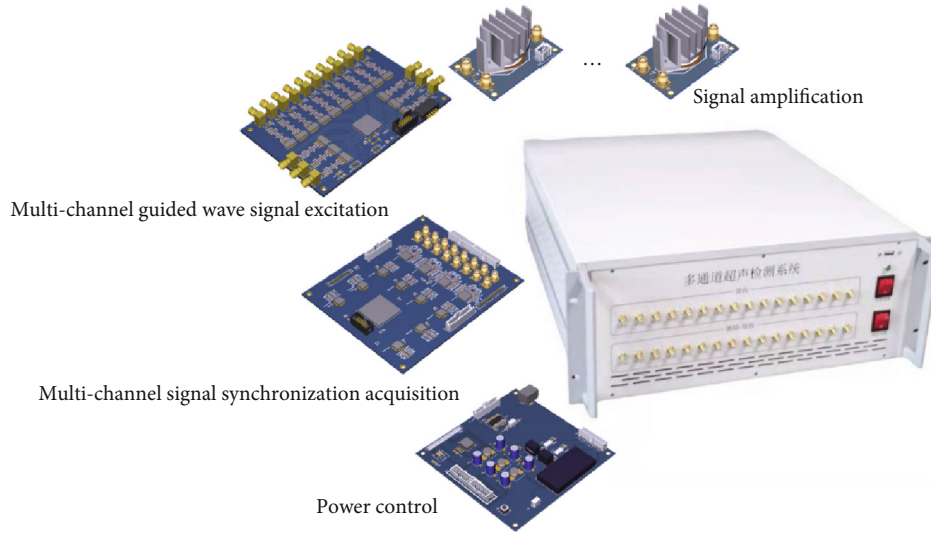


FIGURE 10: Basic structure of multichannel ultrasonic excitation acquisition system.

TABLE 2: Parameters of the equipment indicators.

Parameter name	Value
Data transfer	USB2.0
Excitation frequency	10 kHz~500 kHz
Excitation amplitude	180 V <sub>pp</sub>
Programmable gain amplifier	0~42 dB
Maximum sampling rate	100 MHz
Sampling length	655 us@50 MHz
Power supply	220 V AC

achieve 100 times the voltage amplification of the input signal, the excitation waveform can be amplified with the peak-to-peak value of 180 V<sub>pp</sub> excitation signal.

The multichannel signal acquisition module needs to realize the synchronous signal acquisition of 16 channels. After the signal acquired by each channel enters the acquisition module, it is processed by program-controlled gain amplification, filtering, etc. and then acquired by the high-speed ADC, converted into 8-bit binary code values, read and cached by the FPGA, and transferred to the host computer after the acquisition is completed. To realize the data transmission between the acquisition system and the host computer, the USB2.0 communication interface based on the interface chip CH376 is used, which can realize the bidirectional transmission of data and control instructions. The dynamic link library based on CH376 is used to design the multichannel signal acquisition host computer program, which can automatically realize the total matrix data acquisition process of one excitation and multiple acquisitions.

Figure 12 showed the time-frequency diagram of the Hanning window-modulated 5-period 300 kHz sinusoidal signal output from the system, from the time domain diagram, it could be seen that the peak-to-peak value of the excitation signal can reach 180 V<sub>pp</sub>, the signal had no obvi-

ous distortion, and the signal-to-noise ratio was as high as 40 dB.

## 5. Experimental Study of Pipeline Detection

*5.1. Total Matrix Data Acquisition.* The total matrix data acquisition experiment was conducted on stainless steel pipes using the developed multichannel ultrasonic detection system, and the total matrix data acquired were processed by applying imaging algorithms.

Firstly, total matrix data acquisition experiments were conducted for stainless steel pipes, and the experiments used the same stainless steel pipe parameters as the model established in the simulation experiments. The defects were set as two symmetrical openings with 7 mm diameter artificial through-hole to verify the multidefect detection capability of the method, and to verify the detection capability of the method for scratch defects, two surface scratch damages were randomly set on the pipe surface, which can simulate scratch defects and corrosion damages in the pipe. The selected piezoelectric transducer size was 13.3 mm × 3.5 mm × 1 mm, which was coupled to the surface of the stainless steel pipe by the 502 glue. The piezoelectric transducer array arrangement was also consistent with the setup of the simulation experiment, uniformly arranged on the outer surface of one end of the pipe, and the center distance of each piezoelectric transducer was 27.48 mm. The basic configuration of the detection experiment is shown in Figure 13.

The 16 excitation/reception channels of the instrument were connected to 16 piezoelectric sensors with coaxial shielded wires, which can realize the self-excitation and self-acceptance of each piezoelectric sensor. Since the center frequency of the piezoelectric transducer was 108 kHz, the initial value of the excitation signal was set to 108 kHz in the host computer, the excitation signal was 5-period Hanning window modulating the sinusoidal signal, the excitation channel was set to 16 channel in turn, the sampling

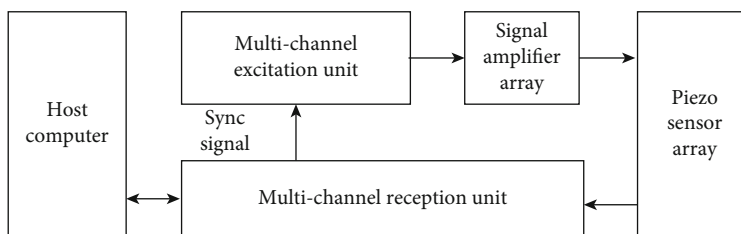


FIGURE 11: Basic structure of multichannel ultrasonic excitation acquisition system.

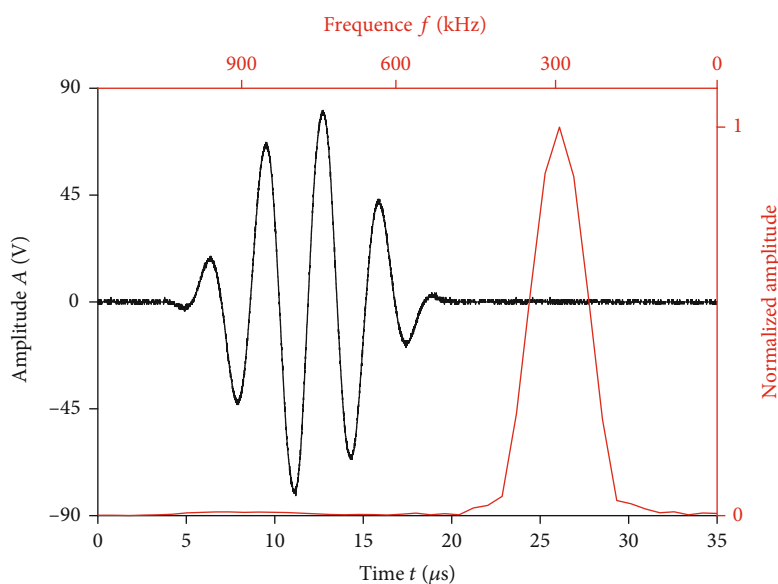


FIGURE 12: Excitation signal test result.

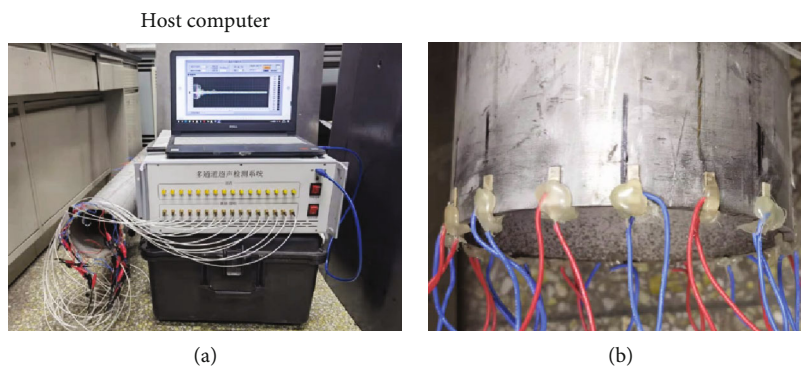


FIGURE 13: Experimental setups and sensor array: (a) experimental setups and (b) sensor array.

length was set to  $655.36 \mu s$ , the gain amplification of the received signal was set to 40 dB, and a total matrix data acquisition was performed after the setup was completed. The signal received from 16 channels after 5 channel excitation is shown in Figure 14, and the comparison with the simulated signal showed that the signal characteristics were the same.

From the acquired signal waveform, it could be seen that the defect signal could not be identified in the self-excited and self-accepted signal of CH5 which is closest to one of

the defect and could not find the defect echoes, even though it has the most significant signal by its channel. Therefore, it is also necessary to apply a focused imaging algorithm to the total matrix signal and remove the influence of other modal guide waves. Firstly, the waveform and spectrum of a single signal were analyzed, as shown in Figures 15 and 16. The frequency band of the echo signal became wider and introduced echo interference from other frequencies, so in addition to applying the focused imaging algorithm, it was also necessary to find a suitable filter band for signal filtering.

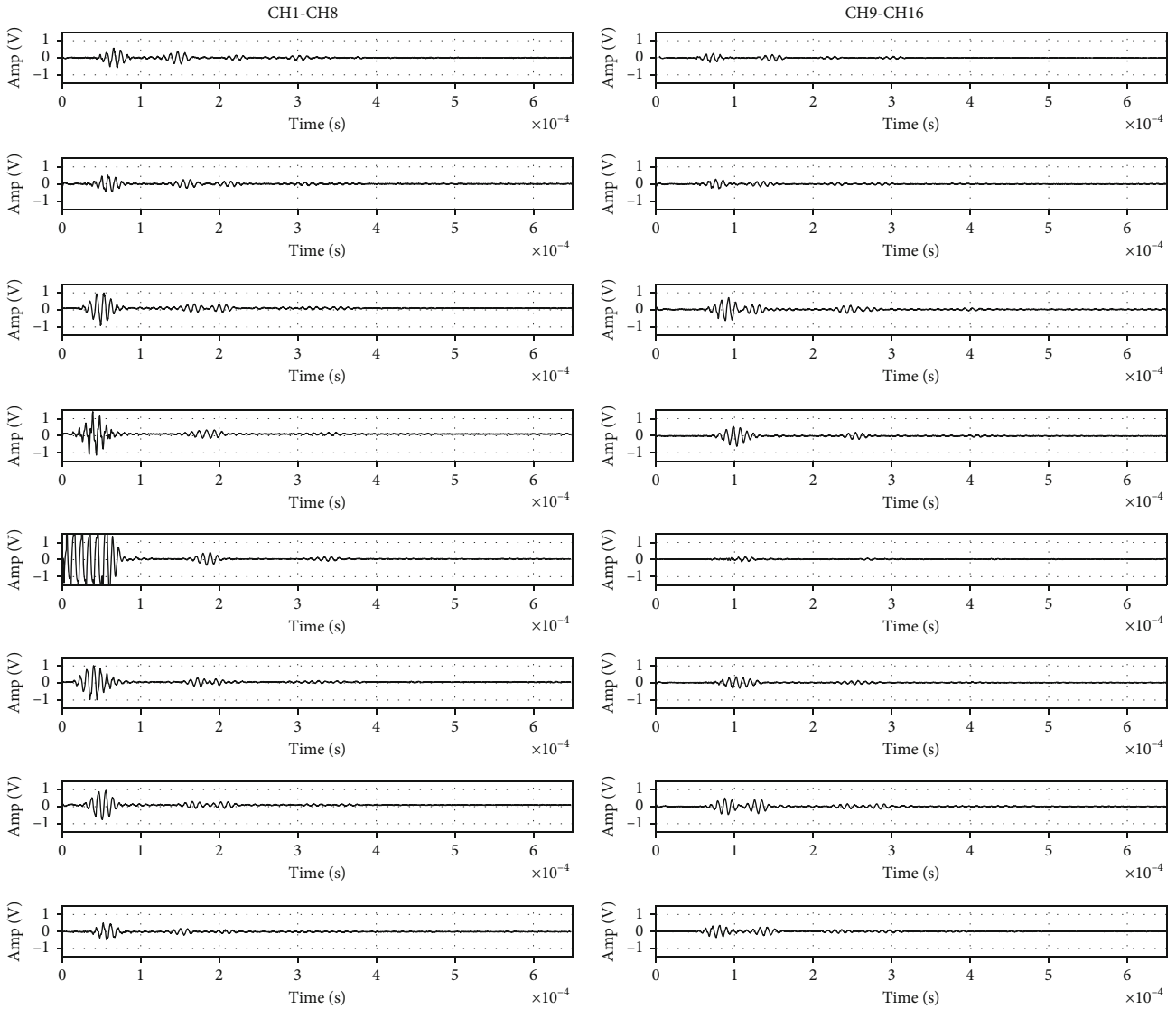


FIGURE 14: Waveform received by 16 channels after excitation of CH5.

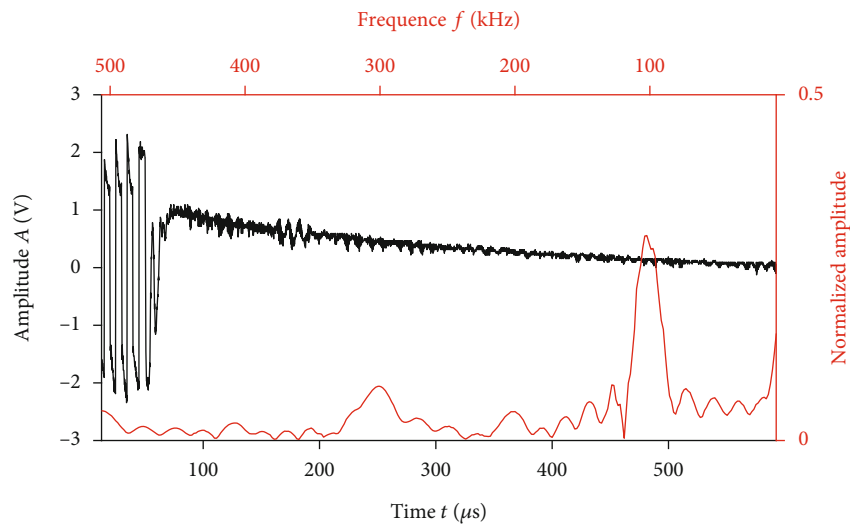


FIGURE 15: Channel 5 self-excitation and self-collection signal.

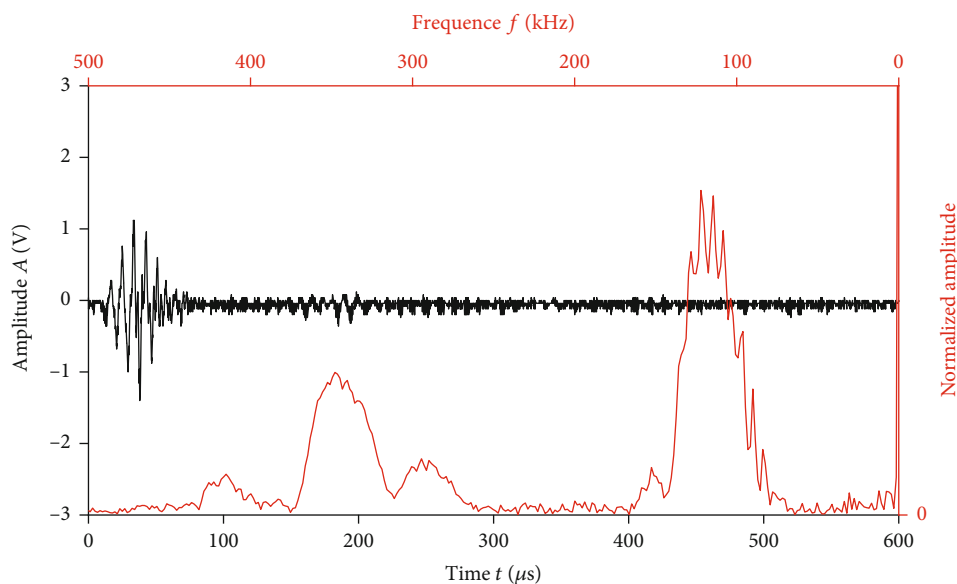


FIGURE 16: Signal received by channel 6.

**5.2. Total Focusing Imaging.** Applying the amplitude total focus method to the collected total matrix data, wave velocity was adopted as the base parameter of 5011 m/s actually measured in the experiment, the basic parameter settings are shown in Table 3, the imaging results were processed for 113 dB dynamic range to remove noise artifacts, from the images obtained (the white circle is the actual location of the defect), it could be seen that the two artificial through-hole set were detected, and the location information of the defect was consistent with the set. The model was the same. Therefore, the basic position information of multiple defects in metal pipes could be obtained by the guided wave total focusing method based on the sensor array, as shown in Figure 17.

From the total focusing imaging results, it showed that the artifacts in the image still could not be completely removed, and the defect echo amplitude was not obvious enough to compare with the artifacts, which was not conducive to the discrimination and localization of pipeline defects, and the setup column pattern and scratch defects could not be distinguished in the figure. However, the imaging results verified the feasibility of total matrix data acquisition imaging for pipeline defect detection.

**5.3. SCF Imaging.** Amplitude total focus imaging uses only the signal amplitude information for imaging, which is susceptible to noise interference and thus leads to imaging distortion; in addition, the influence of signal noise can cause the generation of artifacts and reduce the accuracy of detection results. Phase-based SCF imaging uses the polarity information of the signal for imaging, which is less disturbed by amplitude attenuation and other interference, and can effectively suppress the grating and side flaps of the beam directionality and improve the resolution of imaging. Therefore, the sign coherence factor imaging algorithm was used to process the total matrix data of 16 channels, the narrow-band band pass filtering was performed on the echo signal,

TABLE 3: Stainless steel pipe material parameters.

Parameter name	Set value
Number of elements	16
Distance between the centers of adjacent elements	27.5 mm
Single element width	3.5 mm
Element center frequency	108 kHz
Sampling rate	50 MHz
Imaging length	1500 mm
Imaging width	440 mm

and the imaging resolution was set to 1 mm. 50 dB dynamic range processing was performed on the imaging results to remove noise artifacts, and the imaging results were obtained as shown in Figure 18.

The two installed artificial through-holes and the scratch defects on the pipe surface were clearly distinguishable from the results of the sign coherence factor imaging, which fully illustrated that the equipment and the method introduced in this paper can detect and image multiple small defects in metal pipes and obtain the location of the defects on the pipe surface.

However, from the imaging results, the location of the defect, and the actual location of the defect in the specimen, there was a certain error; for this experiment, the longitudinal positioning error of the round hole was within 2.1%, meeting the detection needs; the reasons for the error were currently considered the following three: the first was the piezoelectric sensor size larger, resulting in inaccurate positioning, and, with half wavelength unequal, will lead to multimode guided wave generation; the second reason was that the wave speed measurement was not accurate enough, resulting in a certain error when imaging; and the third reason was that the piezoelectric sensor was not positioned

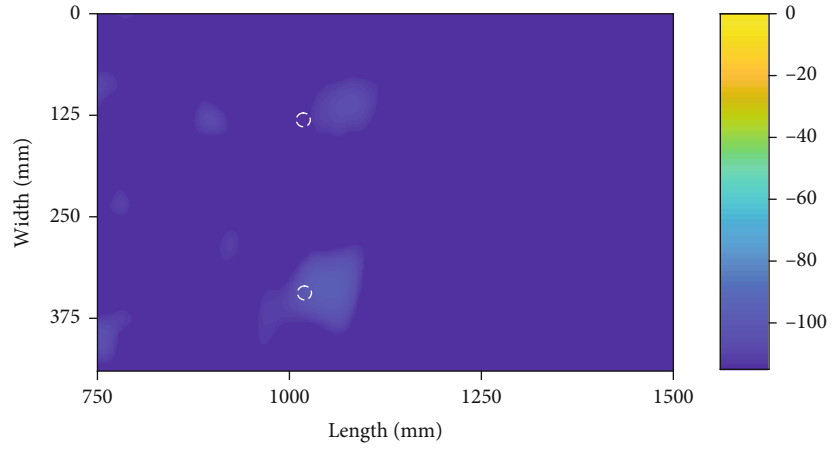


FIGURE 17: Results of pipeline total focus imaging.

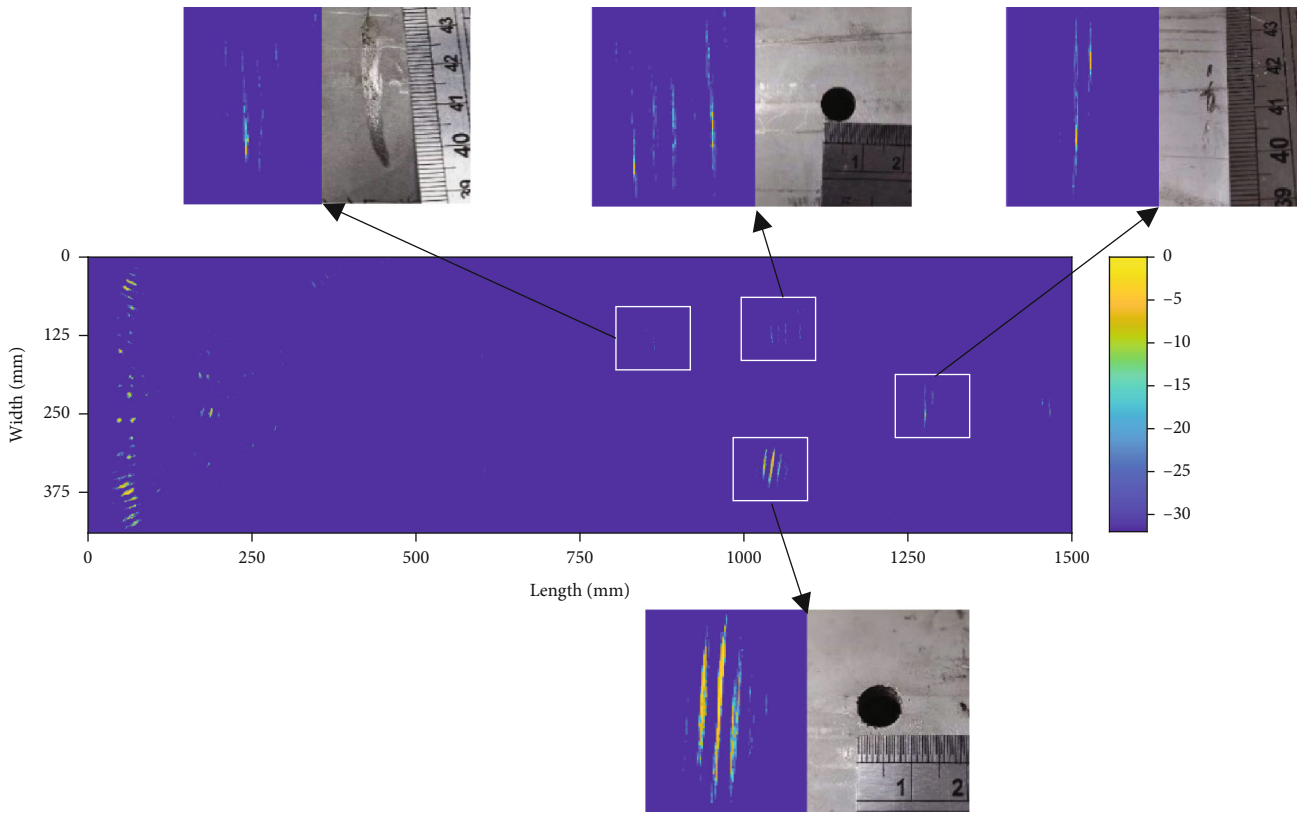


FIGURE 18: 16-channel narrow-band filtered SCF imaging results.

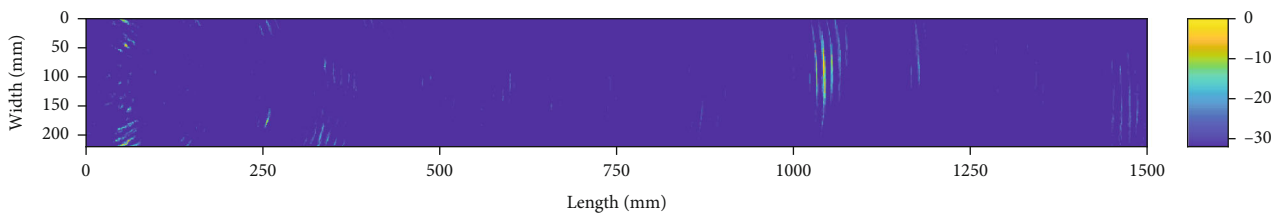


FIGURE 19: Imaging results of CH1 to CH8 channels of pipeline with SCF.

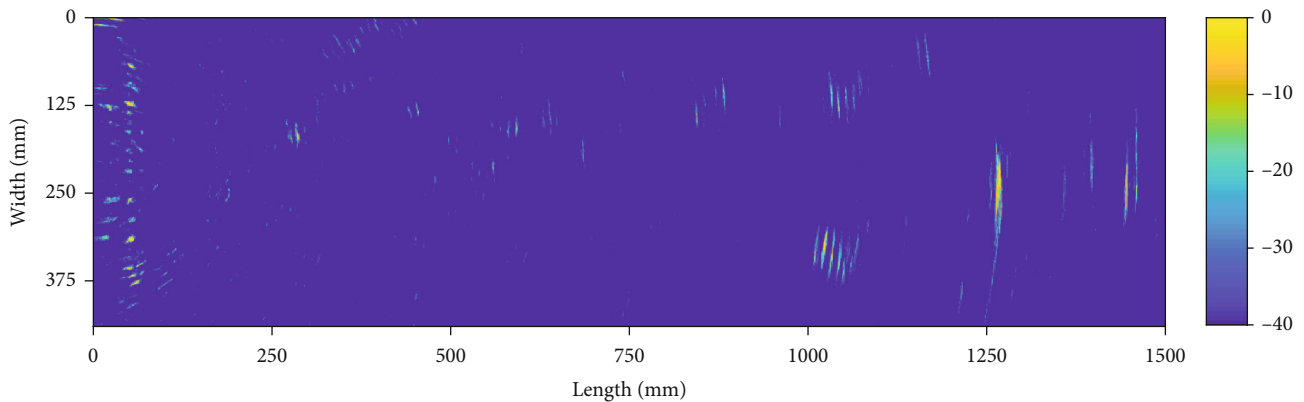


FIGURE 20: Pipeline 16-channel broadband filtered SCF imaging results.

accurately enough around the circumference of the pipe, resulting in deviations in the actual guided wave propagation path.

The results of the sign coherence factor imaging experiment using CH1 to CH8 channels of total matrix data are shown in Figure 19. It can be found that the quality and accuracy of imaging decrease when the number of channel is reduced.

When the filter band of the acquired echo signal was widened, i.e., echoes from other modes might be introduced, the imaging results at this time are shown in Figure 20, and the artifacts produced were significantly increased compared with the results after narrow-band filtering in Figure 18. Therefore, narrow-band filtering of the acquired signal was helpful to remove the interference of guided wave signals from other modes, improve the imaging quality, and reduce artifacts.

## 6. Conclusions

- (1) The total focus method imaging enables defect imaging detection of metal pipes, locating the location of multiple defects
- (2) The 16-channel guided wave focus detection system could realize the total focus method detection, and the signal-to-noise ratio of the collected signal was high. Combining with the host computer program could automatically realize the acquisition process of the total matrix data, which greatly improved the efficiency of the array detection experiment
- (3) Focusing method using sign coherence factor imaging has the advantages of high resolution and high contrast and could eliminate noise artifacts and improve the accuracy of defect localization imaging and detection of scratch defects in the case of imaging results doing lower dynamic range processing. Increased number of sensors could improve the imaging quality, and the filtering of the echo signal could eliminate the interference of the guided wave

signal of other modes and in this way, the detection sensitivity of scratch defects can be effectively improved

## Data Availability

The data used to support the findings of this study are included within the article.

## Conflicts of Interest

The authors declare that there is no conflict of interest regarding the publication of this paper.

## Acknowledgments

This work is supported by the National Natural Science Foundation of China (Nos. 12072004 and 51875010), Beijing Natural Science Foundation (No. 3192006), and General Project of Scientific Plan of Beijing Municipal Education Commission (KM201710005012).

## References

- [1] F. Ciampa, S. G. Pickering, G. Scarselli, and M. Meo, "Nonlinear imaging of damage in composite structures using sparse ultrasonic sensor arrays," *Structural Control and Health Monitoring*, vol. 24, no. 5, pp. 1–13, 2017.
- [2] J. Zhang, B. W. Drinkwater, and P. D. Wilcox, "The use of ultrasonic arrays to characterize crack-like defects," *Journal of Nondestructive Evaluation*, vol. 29, no. 4, pp. 222–232, 2010.
- [3] M. A. Caminero, I. Garcia-Moreno, G. P. Rodriguez, and J. M. Chacon, "Internal damage evaluation of composite structures using phased array ultrasonic technique: impact damage assessment in cfrp and 3d printed reinforced composites," *Composites*, vol. 165, no. MAY15, pp. 131–142, 2019.
- [4] S. J. Jin, B. Zhang, X. Sun, Z. C. Wang, and L. Lin, "Ultrasonic testing of defects in pipeline based on image characteristics of TOFD circumferential scan," *Journal of Mechanical Engineering*, vol. 40, pp. 1–7, 2022.
- [5] N. Li, L. Wang, J. Jia, and Y. Yang, "A novel method for the image quality improvement of ultrasonic tomography," *IEEE*



- Transactions on Instrumentation and Measurement*, vol. 70, pp. 1–10, 2021.
- [6] J. L. Rose and M. Paul, “Ultrasonic guided wave phased array focusing in pipelines,” in *23rd Conference and Exposition on Structural Dynamics 2005, IMAC-XXIII*, Orlando, FL, US, 2005.
- [7] J. Mu, J. Hua, and J. L. Rose, “Ultrasonic guided wave focus inspection potential of bare and coated pipes,” *Insight-Non-Destructive Testing and Condition Monitoring*, vol. 52, no. 4, pp. 195–200, 2010.
- [8] B. Wu, H. Fu, and C. F. He, “Ultrasonic guided wave inspection based on synthetic phase control method,” *Chinese Journal of Scientific Instrument*, vol. 34, no. 3, pp. 31–38, 2013.
- [9] L. Nan, J. Sun, J. Jiao, B. Wu, and C. He, “Quantitative evaluation of micro-cracks using nonlinear ultrasonic modulation method,” *Ndt & E International*, vol. 79, pp. 63–72, 2016.
- [10] C. Holmes, B. W. Drinkwater, and P. D. Wilcox, “Post-processing of the full matrix of ultrasonic transmit-receive array data for non-destructive evaluation,” *NDT&E International*, vol. 38, no. 8, pp. 701–711, 2005.
- [11] J. Zhang, B. W. Drinkwater, and P. D. Wilcox, “Effects of array transducer inconsistencies on total focusing method imaging performance,” *NDT & E international*, vol. 44, no. 4, pp. 361–368, 2011.
- [12] Y. Zheng, C. F. He, B. Wu, and J. Zhou, “Guided wave arrays for large plate structures inspection,” *Acta Acustica*, vol. 38, no. 1, pp. 71–79, 2013.
- [13] J. Camacho, M. Parrilla, and C. Fritsch, “Phase coherence imaging,” *IEEE Transactions on Ultrasonics, Ferroelectrics, and Frequency Control*, vol. 56, no. 5, pp. 958–974, 2009.
- [14] V. T. Prado, R. T. Higuti, C. Kitano, Ó. Martínez-Graullera, and J. C. Adamowski, “Lamb mode diversity imaging for non-destructive testing of plate-like structures,” *Ndt & E International*, vol. 59, pp. 86–95, 2013.
- [15] Z. Liu, K. Sun, G. Song, C. He, and B. Wu, “Damage localization in aluminum plate with compact rectangular phased piezoelectric transducer array,” *Mechanical Systems and Signal Processing*, vol. 70, pp. 625–636, 2016.
- [16] Y. Lyu, H. Hong, G. Song, and C. He, “A simplified integration of multi-channel ultrasonic guided wave system for phased array detection and total focusing imaging,” *International Journal of Acoustics and Vibration*, vol. 26, no. 2, pp. 104–109, 2021.
- [17] A. J. Hunter, B. W. Drinkwater, and P. D. Wilcox, “Autofocusing ultrasonic imagery for non-destructive testing and evaluation of specimens with complicated geometries,” *Ndt & E International*, vol. 43, no. 2, pp. 78–85, 2010.
- [18] J. J. Zhou, Y. Zheng, Z. J. Zhang, and J. D. Tan, “Research on the effect of defect scattering on phased array ultrasonic TFM imaging,” *Chinese Journal of Scientific Instrument*, vol. 2, 2017.
- [19] A. J. Hunter, B. W. Drinkwater, and P. D. Wilcox, “The wave-number algorithm for full-matrix imaging using an ultrasonic array,” *IEEE Transactions on Ultrasonics Ferroelectrics & Frequency Control*, vol. 55, no. 11, pp. 2450–2462, 2008.

## Review Article

# Ultrasonic Testing of Carbon Fiber-Reinforced Polymer Composites

Bocheng Wang <sup>1</sup>, Pengju He <sup>1,2</sup>, Yingnan Kang <sup>1</sup>, Jiabin Jia <sup>3</sup>, Xin Liu <sup>2</sup>,  
and Nan Li <sup>1</sup>

<sup>1</sup>AIMCNT Research Center, School of Automation, Northwestern Polytechnical University, Xi'an 710129, China

<sup>2</sup>School of Information Engineering, Xi'an Eurasia University, Xi'an 710065, China

<sup>3</sup>School of Engineering, The University of Edinburgh, Edinburgh, UK

Correspondence should be addressed to Nan Li; [nan.li@nwpu.edu.cn](mailto:nan.li@nwpu.edu.cn)

Received 18 March 2022; Revised 23 May 2022; Accepted 25 May 2022; Published 27 June 2022

Academic Editor: Carlos Marques

Copyright © 2022 Bocheng Wang et al. This is an open access article distributed under the Creative Commons Attribution License, which permits unrestricted use, distribution, and reproduction in any medium, provided the original work is properly cited.

Composite materials have been extensively used in different fields due to their excellent properties, among which carbon fiber-reinforced polymer (CFRP) is the representative. Especially in high-precision fields, such as aerospace, CFRP has become the main structural material for some core components instead of metal. The particularity of such materials and their components in terms of structure, material properties, and required detection conditions puts forward more stringent and targeted detection requirements for detection technology. Ultrasonic testing technology as one of the important means of composite defect detection, which is derived from advanced nondestructive testing (NDT), has also been a rapid development. The propagation behavior and variation of ultrasonic waves in CFRP composites can reveal defects and damages in CFRP composites. Moreover, by constructing reasonable defect identification technology and detection technology, not only the qualitative and quantitative positioning analysis of defects and damages in CFRP composites can be realized but also the automatic, visual and intelligent NDT, and evaluation of CFRP composites can be realized. This paper mainly reviews the innovative nondestructive ultrasonic testing technology for CFRP composites and briefly introduces the research progress and application of this technology in CFRP defect detection. Finally, advanced nondestructive ultrasonic testing technology is summarized, and the problems and development direction of this kind of testing technology are put forward.

## 1. Introduction

With the increasing development of science and technology, more and more composite materials have been widely used due to their excellent performance [1–3]. Among them, CFRP made of carbon fiber as reinforcement and resin as matrix are shown. As high-performance structural materials, CFRP not only has the characteristics of typical carbon materials, such as high-temperature resistance, friction resistance, and corrosion resistance, but also has the characteristics of high specific strength, high specific modulus, and high fatigue resistance. Therefore, it has been well applied in different fields such as aerospace [4–6], military industry [7], automobile and sports [8, 9], and medical treatment [10].

Due to the influence of the manufacturing process, environmental factors, and some random conditions (such as impact, fatigue, and other human factors), defects and damages are inevitable in the production that is made of CFRP materials. In many cases, these defects and damages are difficult to be detected by human eyes, causing great hidden danger for subsequent use. Therefore, with the extensive application of carbon fiber composite materials in various fields, the requirements for its reliability and safety are becoming higher and higher [11]. Defects and damage have a serious impact on the quality and performance of materials and components and also greatly reduce the service life [12]. To ensure the high quality and reliability of CFRP components, defect detection and quality monitoring is necessary

and important in the process of manufacturing and service via NDT technology, to find out the hidden trouble in time.

The complexity of the internal structure is therefore difficult to detect CFRP and its components. Defect signals of CFRP components with different production and processing techniques and structures have different forms of expression, and it is difficult to distinguish the coupling between characteristic signals generated by different types of defects [13]. To avoid the hidden danger caused by the defects of carbon fiber composite materials, researchers present a lot of detection technologies to detect these defects and damage. Common detection methods include X-ray detection, eddy current detection, penetration detection, ultrasonic detection, and infrared thermal wave detection. Sensors based on optical technology have also become the direction of continuous development in the detection field [14–16], such as polymer optical fiber as a sensor is used for detection [17, 18].

Currently, the commonly used detection methods of CFRP sheet defects mainly include X-ray detection method, eddy current detection method, ultrasonic detection method, and infrared thermal wave detection method, among which ultrasonic detection method is the most commonly used in the world. Ultrasonic detection technology plays an indispensable role in CFRP defect detection and has become the hot spot and focus direction of composite material detection. The detection method based on ultrasonic technology has also become one of the important research directions in NDT field.

This paper presents the research progress of ultrasonic testing technology in the field of defect detection of composite materials (especially CFRP) and summarizes the existing advanced ultrasonic NDT technology, especially in the field of defect detection of CFRP materials. It is desirable for this review can make more relevant researchers understand and invest in the research field of ultrasonic-based technologies. So that the technology can better serve the engineering application and promote the rapid development of the whole industry.

## 2. Basic Concepts of CFRP and Ultrasonic Technology

*2.1. The Structure of the CFRP.* CFRP is composed of carbon fiber and polymer resin, in which carbon fiber acts as reinforcement material to provide strength and polymer resin acts as a matrix to fix the fiber [19, 20]. The structure and performance of CFRP depend on different orientations of carbon fiber (see Figure 1(a)) [21]. The most typical CFRP structure is unidirectional laying (see Figure 1(b)), that is, all carbon fibers are laid in parallel along the same direction in the matrix. There is also the preparation of CFRP, carbon fiber mutual preparation, such a structure will increase the damage tolerance of CFRP (see Figure 1(c)).

The combination of carbon fiber and polymer resin provides the structure with many excellent properties such as lightweight, high strength, and corrosion resistance, which makes the components suitable for a variety of applications (see Figure 2).

In addition to conventional engineering fields, CFRP is also widely used in transportation, military industry, energy, and other industries. However, in the process of production, processing, and application of CFRP, it is inevitable to encounter defects and damage problems, resulting in huge hidden danger. Therefore, defect detection of CFRP is an important part that cannot be ignored.

*2.2. Typical Defects of CFRP.* Defect damage is the main reason why the failure of CFRP. Under the influence of the manufacturing process, environmental factors, and some random conditions, defects and damage of CFRP are inevitable, and their manifestations are the same as those of other fiber composites, mainly including matrix cracking [29], fiber-matrix interface debonding [30, 31], fiber fracture [32, 33], delamination [34, 35], and pore [36, 37].

Matrix cracking is the most serious damage type in composites. Composite materials begin to fail at the onset of static live fatigue loading due to the formation of micro-cracks, which then rapidly spread to cause collective cracking [29] (see Figure 3(a)). Since the initial crack growth parallel to fiber direction is controlled by the toughness of the matrix, the use of tougher resins would be expected to lead improvements in the matrix-dominated properties controlled by the failure mode [38].

Fiber debonding is mainly due to friction for sliding between fiber and matrix interface. Friction between the fiber and the matrix and fiber deformation will affect the strength of the composite [39], resulting in fiber debonding. Fard et al. [31] studied the correlation between nanoscale interfacial debonding and multimode fracture in carbon fiber composites (see Figure 3(b)).

Delamination defects are very common in composite materials [40] (see Figure 3(c)). Composite laminates are degummed between layers, causing cracks and forming thin large gaps. The main reason for delamination is the mismatch of thermal expansion coefficient between the matrix and fiber or too long storage time, reinforced materials without surface treatment, external shock, etc. [41]. In addition, delamination may occur when drilling composites [42]. The delamination between carbon fiber layers is the most serious defect type in carbon fiber resin matrix composite products, which reduces the compressive strength and stiffness of the material and affects the structural integrity. Under the condition of mechanical or thermal load, the delamination in the structure will continue to increase, which may lead to material fracture when the situation is serious.

Pore refers to the formation of voids in carbon fiber products during the molding process, which is one of the principal defects of CFRP [43, 44] (see Figure 3(d)). It should be divided into fibrous pores (including pores in fiber bundles) and lamellar pores. When the porosity is less than 1.5%, the pores are spherical. When the porosity is greater than 1.5%, the pores are cylindrical parallel to the fiber axis. Pores in carbon fiber composites mainly affect the interlaminar shear strength, longitudinal and transverse bending strength and modulus, longitudinal and transverse tensile strength and modulus, and compressive strength and modulus.

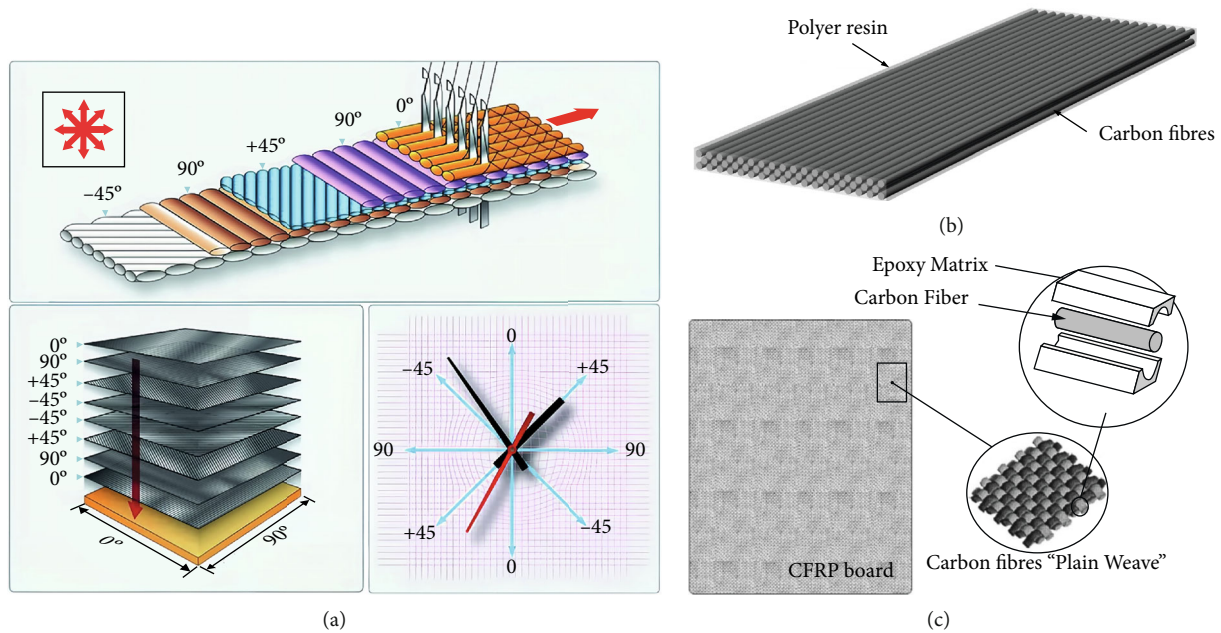


FIGURE 1: Typical CFRP structure. (a) Format description of carbon fiber orientation angle in CFRP material [21]. (b) Typical structure of CFRP [22]. (c) A CFRP board with “plain weave” structure [23].

In order to avoid the defects of CFRP, on the one hand, it is necessary to strictly control every process from material selection to production and then to final production. From the selection of high quality raw materials for manufacturing CFRP, the supervision in the production process and the improvement of the standardization and efficiency of the whole production process, and then to the final transportation process to strictly control, all kinds of defects in CFRP can be reduced. On the other hand, the damage detection and real-time monitoring of CFRP are particularly important. In order to ensure the safe application of composite materials, detection and research of composite materials have attracted extensive attention.

### 3. Advanced Ultrasonic Testing Technology

Defect damage of carbon fiber composites can be identified by destructive methods and NDT methods. The destructive method mainly refers to the traditional metallographic method, which is to observe a certain section of the material through a metallographic microscope, and can intuitively find the internal structural characteristics of the material. Defects inside CFRP can not only be determined by metallographic methods but also can realize the understanding of the shape, size, and location distribution of defects. However, the metallographic method requires grinding and polishing of carbon fiber composite materials before metallographic observation, which is inefficient and leads to unexpected damages to the materials. In practical engineering applications, especially for the inspection of large quantity of workpieces, a metallographic method is unrealistic.

As an emerging detection method, NDT can complete the detection without destroying the performance and internal structure of the detected object. In NDT, ultrasonic test-

ing technology has been one of the most widely used testing technologies due to its characteristics of harmlessness, high sensitivity and accuracy, easy implementation, and wide application.

The basic principle of ultrasonic defect detection is that the directionally emitted ultrasonic beam encounters a defect when it propagates in the workpiece to be tested, that is, the reflection and attenuation of the wave are generated, and the defect signal is obtained after signal processing. There are three basic defect display methods: A-scan showing defect depth and defect reflected signal amplitude, B-scan showing defect depth and its distribution in longitudinal section, and C-scan showing distribution in plane view.

Using the propagation behavior of the ultrasonic longitudinal wave in the composite, the time-domain characteristics of the acoustic wave echo signal are recorded, including the propagation time, signal amplitude, and phase information in the detected composite material, and are displayed by ultrasound A-scan. Based on the A-scan detection technique of ultrasonic echo signal technology, the accurate quantitative assessment of the thickness and defect depth of the composite parts is detected, and the qualitative-evaluation of defects can be obtained.

#### 3.1. Ultrasonic-Based Detection Methods

**3.1.1. Ultrasonic C-Scan Testing Technology.** As one of the earliest methods for NDT of composite materials, ultrasonic testing technology can not only realize the qualitative and quantitative characterization and evaluation of composite material defects and damage and is easy to implement engineering testing applications; it can also be used for the internal microstructure and composition of composite materials,



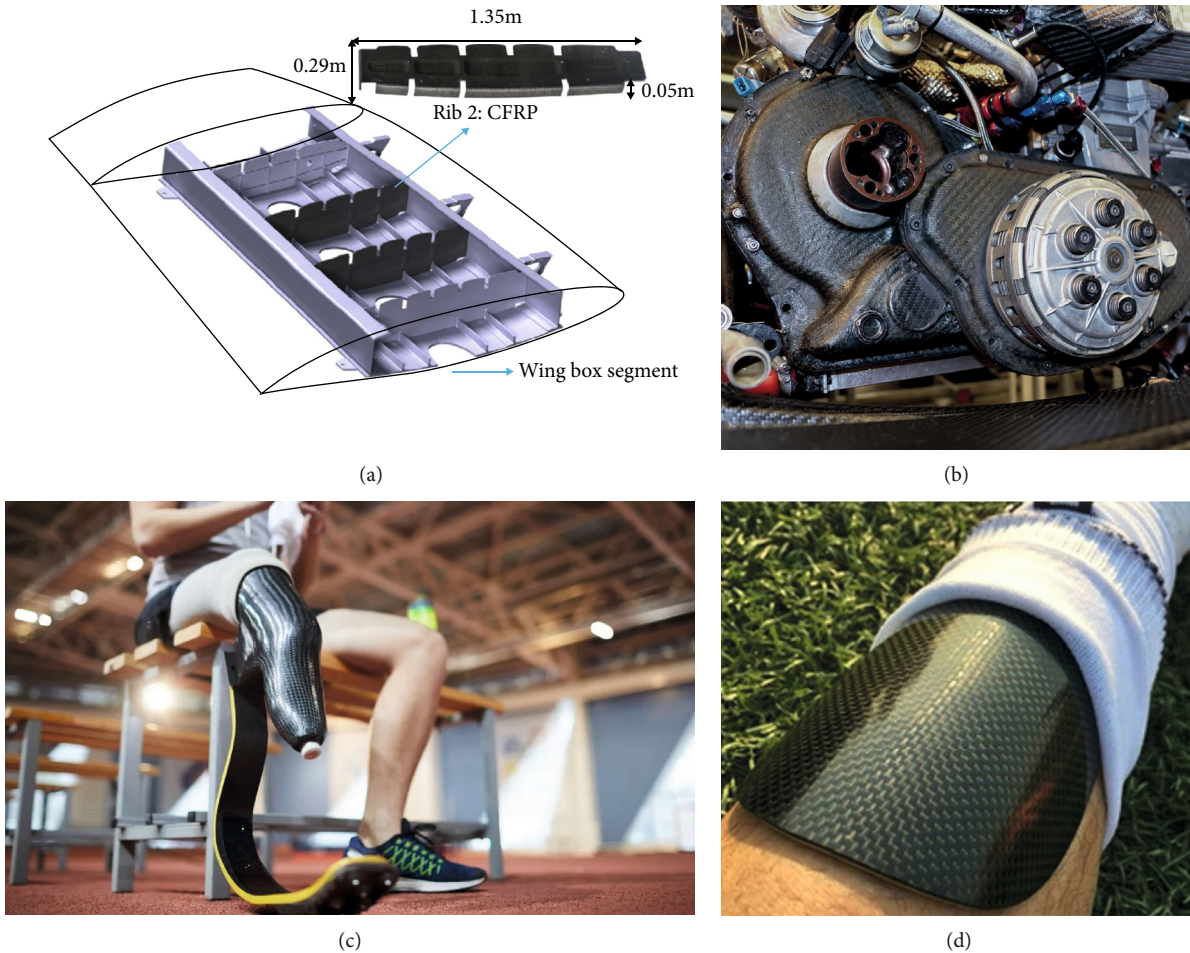


FIGURE 2: Application of CFRP in various fields. (a) The Airbus A350 XWB is made of 52% CFRP, including the wing SPAR and fuselage parts [24]. The rear wing SPAR of the Airbus A350 XWB demonstrator wing is covered by CFRP [25]. (b) CFRP is also widely used in high-end racing cars. It is now can be used in the engine part [26]. (c) CFRP is used in the medical field (a prosthesis made of CFRP with better strength performance [27]). (d) CFRP is used in the sports field (carbon plate running shoes and sports protectors [28]).

such as fiber content distribution, elastic properties, and other characterization.

Ultrasonic C-scan detection technology is a very extensive and important method for NDT and evaluation of composite materials. Founded on the principles of ultrasonic C-scan and B-scan imaging, it can realize ultrasonic visual NDT of composite structures. In general, the ultrasonic C-scan imaging inspection technology based on a single sound source is the most commonly used composite material inspection technology so far. Compared with the destructive method, it will not damage the measured object and achieve better detection results. Water immersion ultrasonic C-scan detection is commonly used. Water is used as the coupling agent, and ultrasonic waves enter the specimen through water for detection. However, this method may affect the specimen with the water coupling agent.

Songping et al. [45] introduced a depth-direction ultrasonic C-scan detection technology. Based on the characteristics of ultrasonic propagation in the time domain, several scanned images of the interior of carbon fiber composites can be realized, which can be used only for defect detection. Wu et al. [46] proposed a multisensor information fusion

technology for defect detection of composite ultrasonic C-scan. Hasiotis et al. [47] used ultrasonic C-scanning technology to detect artificial defects added to CFRP composites, realized the determination and characterization of defects, and accurately measured the thickness of the specimen. Shiino et al. [48] used ultrasonic C-scanning to detect the damage to carbon fiber laminates caused by thermal stress caused by temperature changes. It is verified that temperature changes can cause cracks in the low porosity of the composites. Gao [49] discussed the influence of different placement methods of carbon fiber laminates on the results of water jet ultrasonic C-scan defect detection and obtained that the upper part of the part occlusion has the greatest influence on the water jet, the lower part occlusion is the second, and the left and right effects are the least. Ultrasonic C-scan has a high frequency and good penetrability. Therefore, rapid and accurate detection of delamination and debonding defects has become the primary choice for the detection of large composite components such as aircraft parts [50]. Patronen et al. [51] detected the possible debonding defects of the multilayer stepped lap structure between the carbon fiber composite wing plate and the titanium attachment in the fighter and analyzed

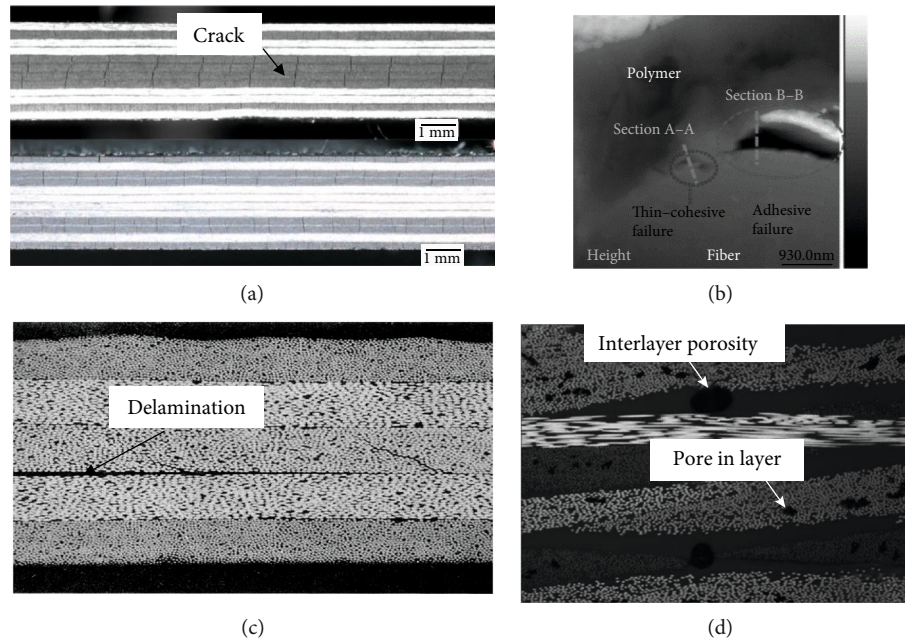


FIGURE 3: Common defects of CFRP. (a) Matrix cracks of carbon fiber composite materials [29]. (b) The interface part of the sample is debonding [31]. (c) Section of delamination defect [40]. (d) Pore defects of fabric CFRP [43].

TABLE 1: Ultrasonic phased array detection of different defects.

Defect type	Applications
Delamination defect	Nageswaran et al. [58] accurately identified defect shape for CFRP artificial delamination defects (2006)
	Xu et al. [59] used linear phased array transducers to accurately detect the layer defects and depth of the R zone of L-shaped components (2013)
	Guang and Na [60] quantitatively measured the sample thickness and defect depth through experiments on linear array and arc array phased array probes (2013)
	Meola et al. [61] used ultrasonic phased array technology to measure the shape, size, and depth of a 20 mm diameter circular delamination defect embedded in CFRP (2015)
	Kappatos et al. [62] used modeling laminated CFRP composites with various artificial delamination defect modes and simulated detection with phased array delay timing and sampling array techniques (2017)
	Zhang et al. [63] focused on the feature extraction and imaging methods to characterize the size and position information of delamination defects through the ultrasonic phased array detection method (2018)
Debonding defect	Caminero et al. [64] prepared samples with preembedded layered defects of different materials, shapes, sizes, and buried depths and studied the influence of the layering method and thickness on the test results (2019)
	Zhang and Du [65] adopted PAU testing technology and obtained the ideal detection parameters for delamination defects of carbon fiber laminate structures through modeling of sound field and delamination defects, CIVA simulation, and detection tests (2020)
	Cao et al. [66] used ultrasonic phased array technology to conduct NDT and quantitative evaluation of embedded delamination defects in carbon fiber composites and analyzed the measurement error (2021)
	Li et al. [67] used the ultrasonic phased array system to detect three common defects in CFRP delamination, inclusion, and debonding established and trained a BP neural network to identify the three defects, and the recognition rate reached 95.7% (2015)
Pore defect	Lamarre [68] realized the detection of small defects of 1.5 mm in carbon fiber composite materials for wind turbine blades, which can detect defects such as debonding, delamination, and wrinkles (2017)
	Grondin [69] proposed an array of ultrasonic inspection technology based on adaptive focusing and applied it to the accurate detection of defects in complex composite materials in aviation (2018)
	Grondin and Li et al. [69, 70] used all-focus 3D PAU testing to detect debonding defects of carbon fiber composite materials used in bogies (2021)
Pore defect	Zhang et al. [71] used a line array transducer to configure an angled delay block for sector scanning to detect defects such as pores and delaminations in the R zone (2013)
	Li et al. [72] established a CFRP microcutting simulation model with pore defects and studied the microcutting behavior of CFRP with different fiber arrangement directions under different porosity conditions (2022)

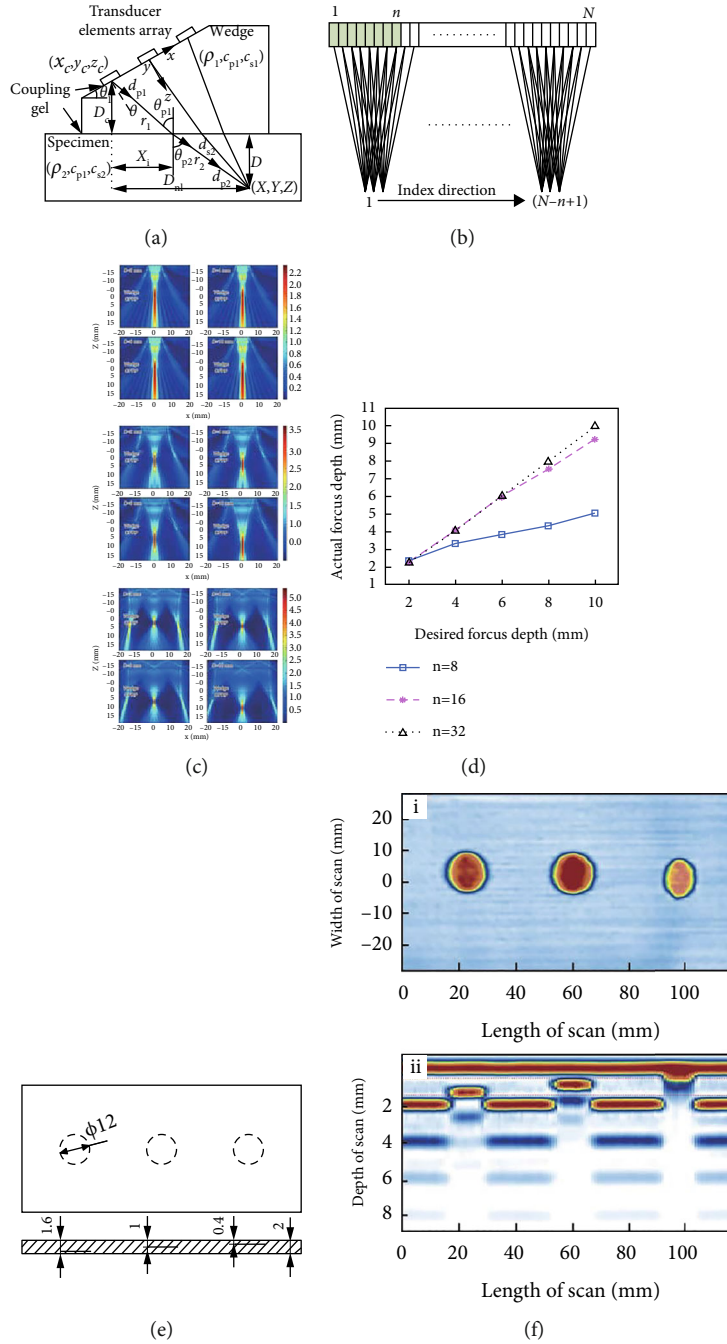


FIGURE 4: Phased array inspection of CFRP laminates [74]. (a) Phased array ultrasound detects the acoustic radiation schematic diagram. Phased array ultrasound realizes the deflection and focus of the acoustic beam by controlling the delay time of the excitation and receiving acoustic waves of each element in an electronic way. (b) A schematic diagram of zero-focus scanning method for testing CFRP laminates using phased array ultrasound; the focusing effect is the best when the beam is vertically incident inside the plate. (c) Simulation results of the sound field under different combinations of activation aperture and focus depth. (d) The comparison between the setting value and the simulation value of focusing depth under different activation apertures shows that the larger the activation aperture is, the smaller the error between the simulation value and the setting value of focusing depth is, and the more accurate the focusing is. (e) Schematic diagram of defect size and distribution. (f) phased array detection image of CFRP laminate (i) C-scan and (ii) B-scan.

the phase and amplitude changes of the ultrasonic waves at the interface. Defects larger than 4 mm can be detected by using the phase change, and scanning detection of the outer and inner debonding defects is realized by using different echo amplitude changes and gain adjustment.

3.1.2. *Array Ultrasonic Testing Technology.* Array ultrasonic testing technology has become one of the main developed detection technologies in the aerospace field in recent years due to its high detection accuracy and good flexibility. At present, different array ultrasonic testing technologies have



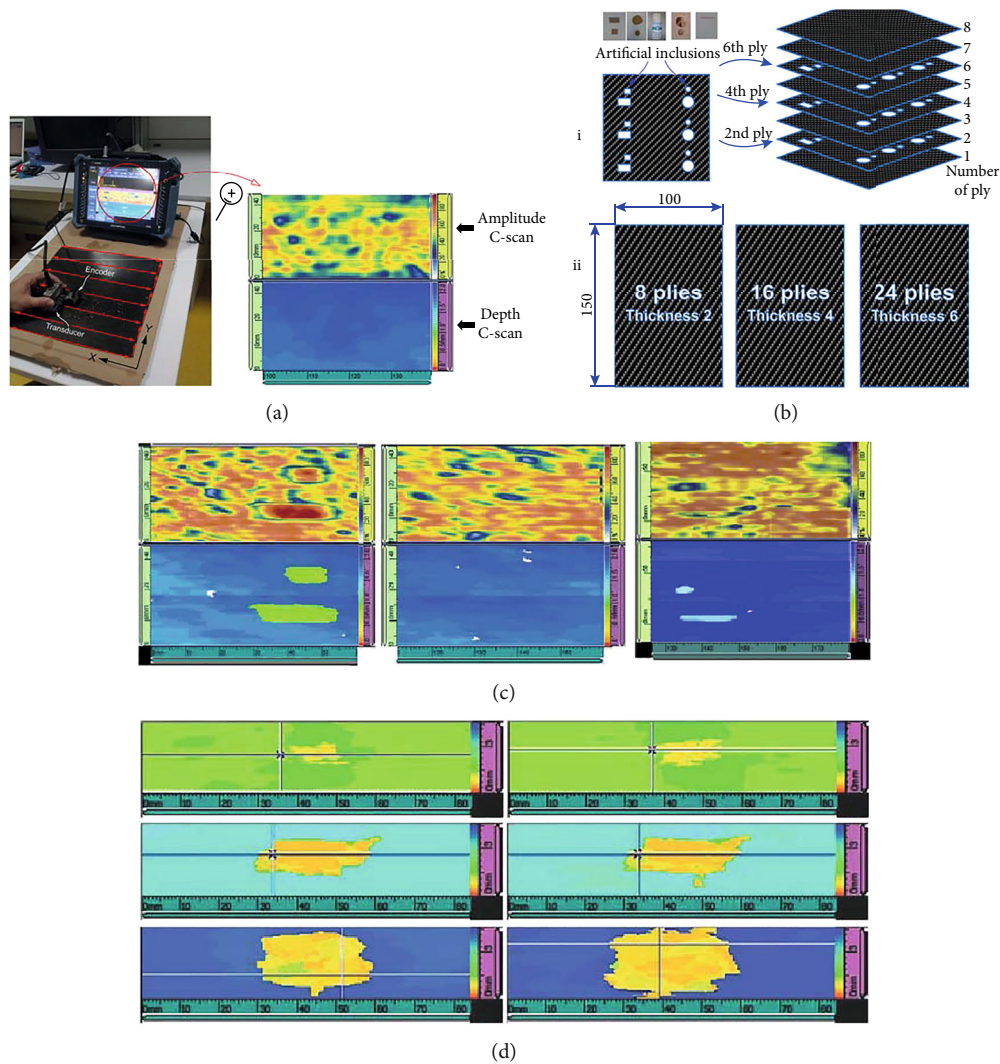


FIGURE 5: Ultrasonic phased array defect detection experiment [64]. (a) Experimental equipment of PAU testing and its ultrasonic C-scan image. (b) Experimental CFRP samples for inclusion defects (i) and impact defects (ii). (c) Different inclusion defect detection results. (d) Different impact energy test results.

gradually replaced conventional ultrasonic testing methods and are widely used in the NDT and evaluation of complex structures and special materials in the aerospace field, but it is difficult to identify defects and has higher requirements for the skills of operators.

(1) *Array Ultrasonic Testing*. Zhou et al. [52] combined piezoelectric sensing array and ultrasonic Lamb wave detection technology to detect the debonding damage of carbon fiber composite T-joint and used the improved BP neural network system to analyze the damage state identify. The Structural Health Monitoring and Prediction Research Center of Nanjing University of Aeronautics and Astronautics [53] proposed a spatial filter damage imaging localization method independent of the signal propagation speed. Based on multidimensional piezoelectric sensor arrays and ultrasonic Lamb waves, the damage to carbon fiber laminates was realized. The positioning error is about 1 cm; the online monitoring of the damage of the composite T-joint has been

realized, and it has been verified by the ultrasonic C-scan method [54]; the team also proposed a multisignal classification damage imaging method of the sensor line array. Experiments were carried out on aviation carbon fiber composite panels to achieve damage imaging and localization [55].

Wong et al. [56] used a two-dimensional ultrasonic array transducer composed of 64 piezoelectric elements to measure the full elastic constant matrix of anisotropic carbon fiber sheets, which are different from the traditional failure to determine the elastic properties of CFRP materials, a method for testing the elastic properties of composite materials in situ nondestructively. Liu et al. [57] carried out research on the detection method based on ultrasonic complex analytical signals. Using array ultrasonic detection experiments, the geometry of the fiber layup inside the microstructure of carbon fiber laminate composites can be clearly observed by the detection and imaging method of ultrasonic complex analytical signals.

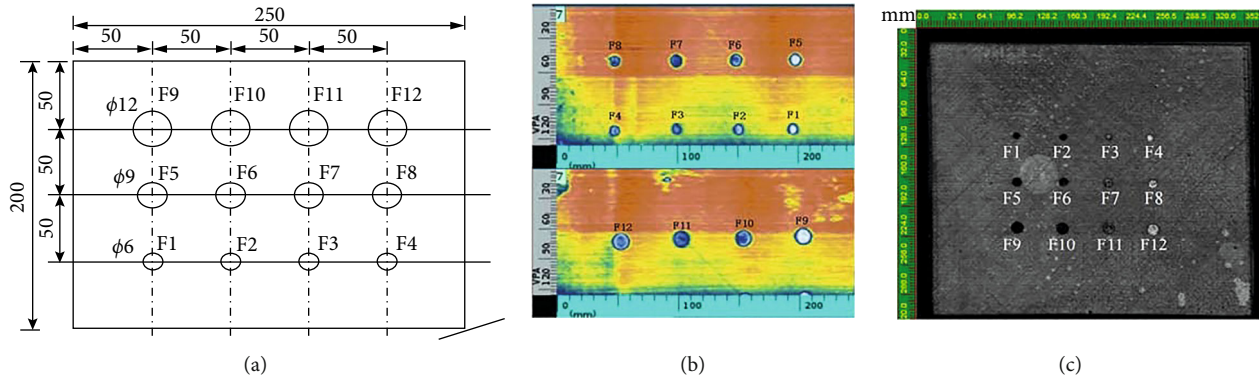


FIGURE 6: Ultrasonic phased array inspection of fuselage panels [75]. (a) Defect distribution map. (b) Ultrasonic phased array inspection results. (c) High-resolution ultrasonic C-scan results.

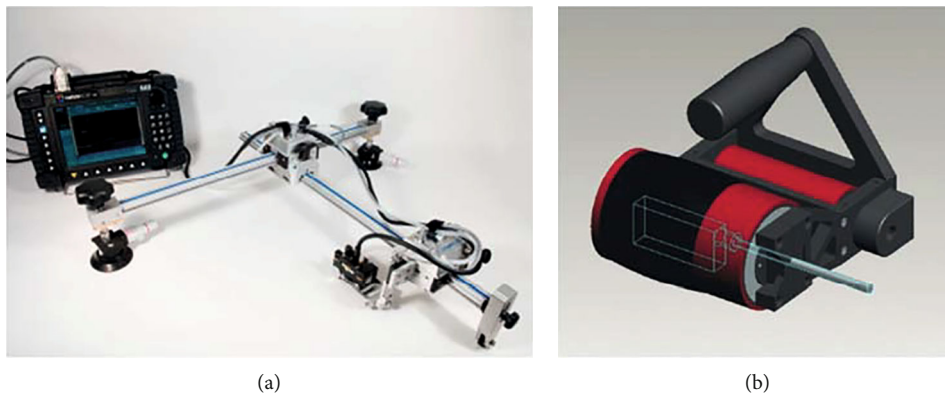


FIGURE 7: Improvement system of ultrasonic phased array. (a) Glide scanner combined with phased array device. The combination of glide scanner and phased array provides a completely portable inspection solution for large-area plane inspection of CFRP components [76]. (b) The ultrasonic array is placed on a rubber-coupled wheel, and the wheel can be manually applied or scanned by the structure and automatic scanning system, which can realize the inspection of a large composite structure. The glide scanner and phased array are combined [77].

(2) *Phased Array Ultrasonic (PAU) Testing*. PAU testing technology is a multichannel testing method based on array transducers, which can deflect and focus sound waves in a designated area inside the test piece using phase control. Compared with the conventional single-channel ultrasonic testing technology, PAU testing technology has more flexible beam control capability, higher detection sensitivity, resolution, and measurement coverage (range). A list of PAU testing for different defect types is shown in Table 1.

Kappatos et al. [62] carried out simulation detection by modeling various artificial delamination defect modes (different sizes and depths) of laminated CFRP composites, phased array delay timing, and sampling array technology, followed by Next, other types of defects will be simulated. Aschy et al. [73] compared the same ultrasonic phased array imaging methods, such as focused line scan, single plane-wave imaging, and dynamic depth focusing, and applied them to the defect detection of carbon fiber materials, identifying the performance and limitations of each method, and improved total focusing method and plane-wave imaging algorithm. Cao et al. [74] simulated the PAU sound field and studied the sound field characteristics under different activation apertures. Prepared CFRP were tested by the

PAU detection system (see Figure 4), realizing the accurate identification of delamination defects of CFRP laminates and effectively improving the accuracy of defect detection.

Caminero et al. [64] conducted experiments on inclusion defects and impact damage of CFRP and 3D printing reinforced composites using ultrasonic phased array technology (see Figure 5), successfully identified artificial inclusions, and estimated their location, size, and morphology. It was also obtained that the impact damage caused more extensive delamination with increasing impact energy and composite thickness.

Li et al. [75] carried out defect detection and quantitative analysis on the carbon fiber composite fuselage panels of large aircraft using ultrasonic phased array detection (see Figure 6), providing technical support and test-ability verification for practical applications.

In addition to the continuous development of PAU testing technology, relevant testing systems have also been improved. Phased array and some special equipment are combined to achieve better testing effect or larger testing range. Habermehl et al. [76] and Freemantle et al. [77] have combined the ultrasonic phased array system to provide a new solution for defect detection of large CFRP components (see Figure 7).

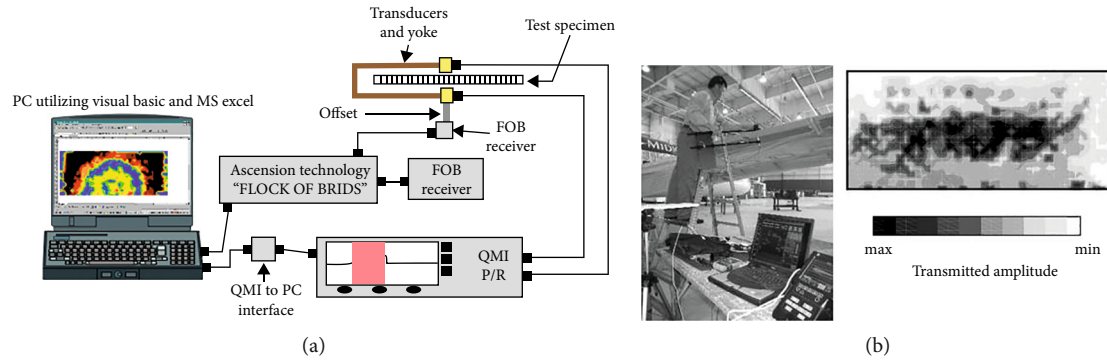


FIGURE 8: An on-site ACU testing system [84]. (a) ACU testing system. (b) ACU C-scan images of an airline that is manually scanned. On the left, is a photo of a scan on the right-wing of the aircraft, and on the right, is the result of the scanned image.

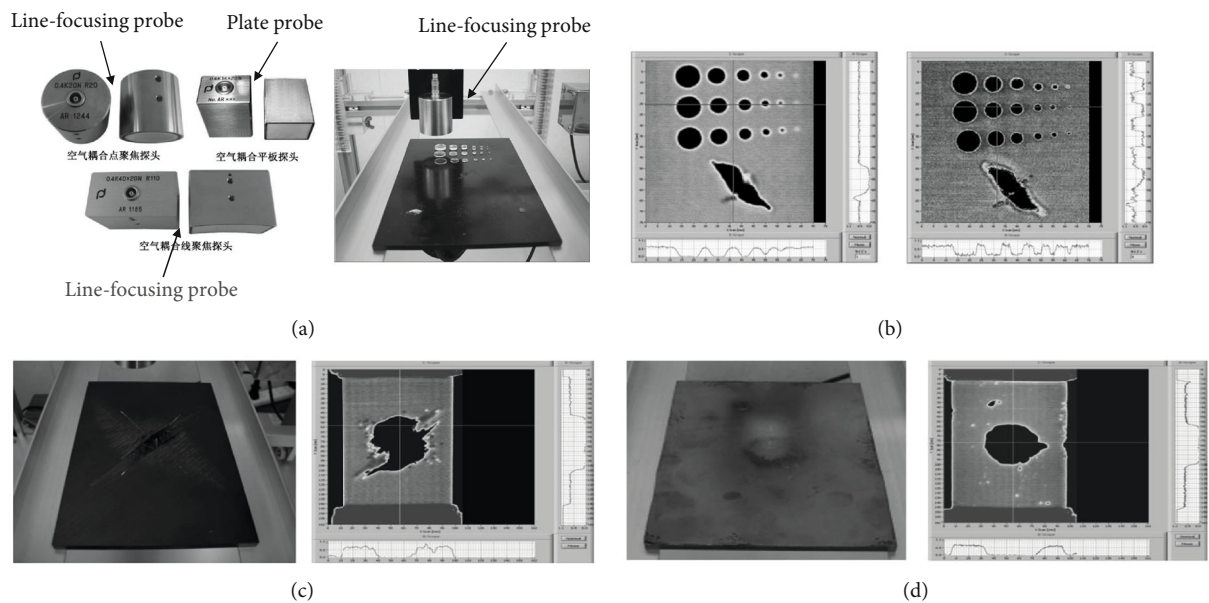


FIGURE 9: Noncontact ACU testing [85]. (a) Different shapes of air-coupled probes (left figure), with different frequencies of point-focused air-coupled transducers on CFRP test samples with scratches detection experiment (right figure). (b) 400 kHz point focusing probe detects that the minimum defect diameter is 2 mm, and the imaging of the simulated defect with a diameter of 1 mm is not clear (left figure); 800 kHz point focusing probe is very clear about the imaging of 1 mm simulated defects (right figure). (c) Defect detection results of aviation CFRP plate specimens. (d) Defect detection results of CFRP plate specimens with a metal coating.

3.1.3. *Air-Coupled Ultrasonic (ACU) Testing.* Typically, the ultrasonic inspection of composite aerospace composite parts employs the ejector technique [78]. However, water coupling brings disadvantages such as pressure changes, air bubbles, limescale, algae, and mechanical corrosion. ACU testing technology uses air as the coupling medium and uses the ACU transducer to excite and receive ultrasonic waves to detect defects in materials and structures.

The difference between ACU testing technology and traditional ultrasonic testing technology is mainly in the presence of a coupling medium, which is intuitive and easy to implement for defect detection of composite materials. With the continuous development of key technologies, such as transducers, signal processing, detection methods, and detection systems, ACU detection technology has been gradually applied in aerospace and other fields to solve structural

parts for which liquid couplants are prohibited (such as honeycomb sandwich materials) and inspection challenges for in-service components such as helicopter tail booms [79]. Due to the large sound attenuation coefficient and the low acoustic impedance of air, the center frequency of the transducer is generally lower than 1 MHz, and a multiperiod modulation pulse train needs to be used as the excitation signal to increase the energy, resulting in a large wavelength and focus of the excitation ultrasonic sound field. Spots have a faint lateral and vertical resolution and mainly use the penetration method to detect thin-walled, low-impedance materials (CUCUEVAS nonmetals such as composite materials).

Salazar et al. [80] designed and developed a high-power and high-resolution pulse generator ACUNDT system, which solved the problems caused by liquid couplants and contact systems in composite material testing. The Kaunas



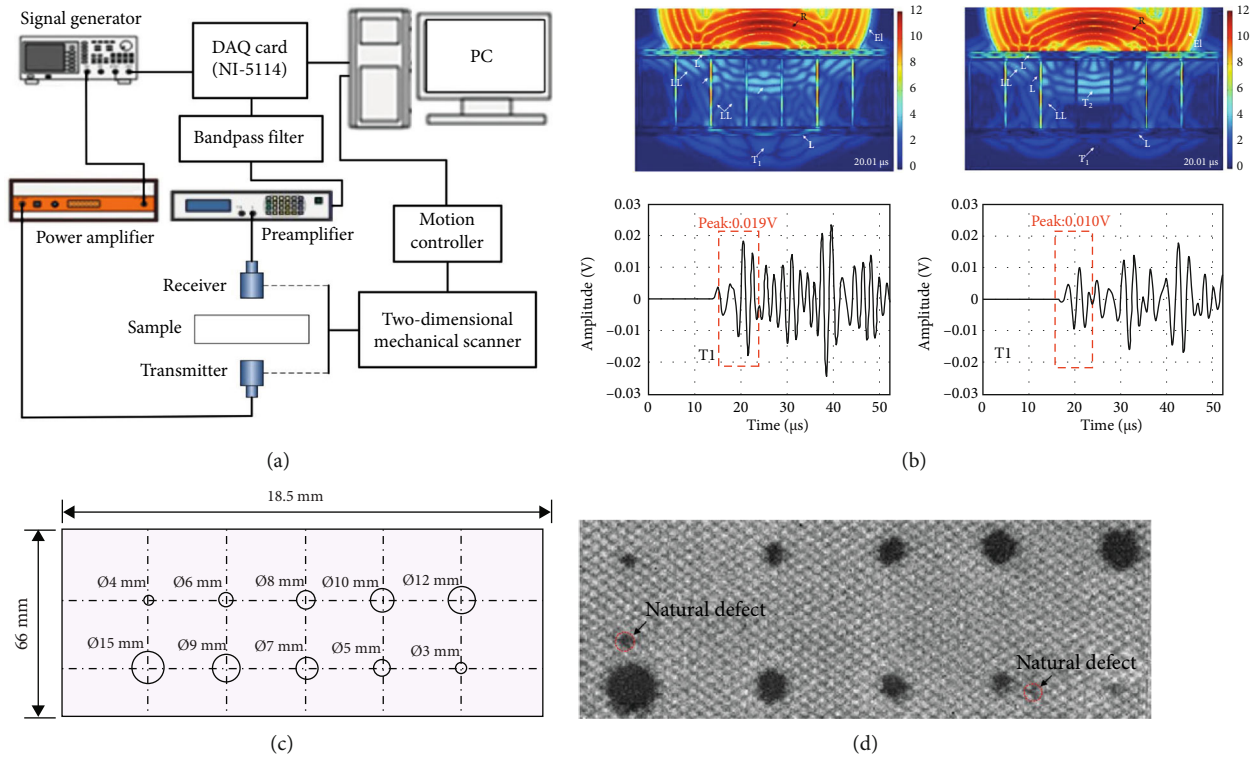


FIGURE 10: Noncontact ACU testing technology [866]. (a) Schematic diagram of the experimental device (DAQ: data acquisition). (b) Composite material samples and defect layout. (c) The top figure is the sound field distribution of the complete honeycomb sandwich composite model at  $20.01 \mu\text{s}$  and the A-wave signal obtained by calculation and simulation, and the bottom figure is the sound field distribution of the honeycomb sandwich composite model with embedded peeling defects and the A-wave signal obtained by calculation and simulation. (d) C-scan result.

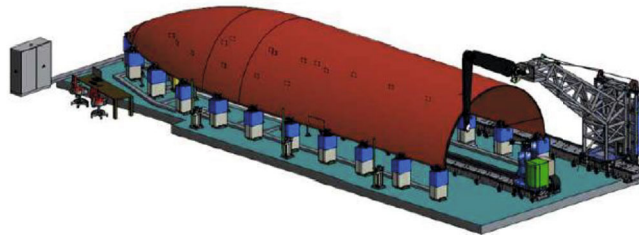


FIGURE 11: One of the largest air-coupled ultrasound C-scan systems in the world [78].

University of Technology Ultrasound Team [81] studied the accuracy of air-coupled ultrasound technology to detect delamination defects in composite materials such as carbon fibers at low frequencies, using a 4700 kHz transducer to measure the 25 mm diameter in GLARE3-3/2 composites. The delamination defect was detected, and the defect diameter was 22 mm obtained by the -6 dB method from the C-scan results. Steinhausen et al. [82] proposed a detection method based on multiarray air-coupled transducers in order to use different frequency transducers to detect various types of defects (inclusion, delamination, debonding, etc.) in the CFRP board, in which each array is excited at different frequencies, and all the arrays are simultaneously excited during detection to increase bandwidth, thereby improving the detection efficiency. Imielińska et al. [83] studied the ACU detection method for impact damage defects of carbon

fiber, glass fiber, and polyamide fiber reinforced resin matrix composites. Peters et al. [84] developed an on-site inspection system applied to aircraft components based on ACU inspection technology (see Figure 8), which can realize image inspection of defects and damages of various aircraft composite materials. Chang and Lu [85] developed a set of the high-sensitivity noncontact ACU detection system to achieve accurate detection and evaluation of carbon fiber composites (see Figure 9). Li and Zhou [86] used noncontact ACU testing technology to detect and characterize debonding defects in aviation carbon fiber honeycomb sandwich composites (see Figure 10).

Hillger et al. [78] in Germany made progress in the detection and imaging difficulties of ACU testing technology in aerospace sandwich components, composite materials, and other components and carried out ultrasonic testing of

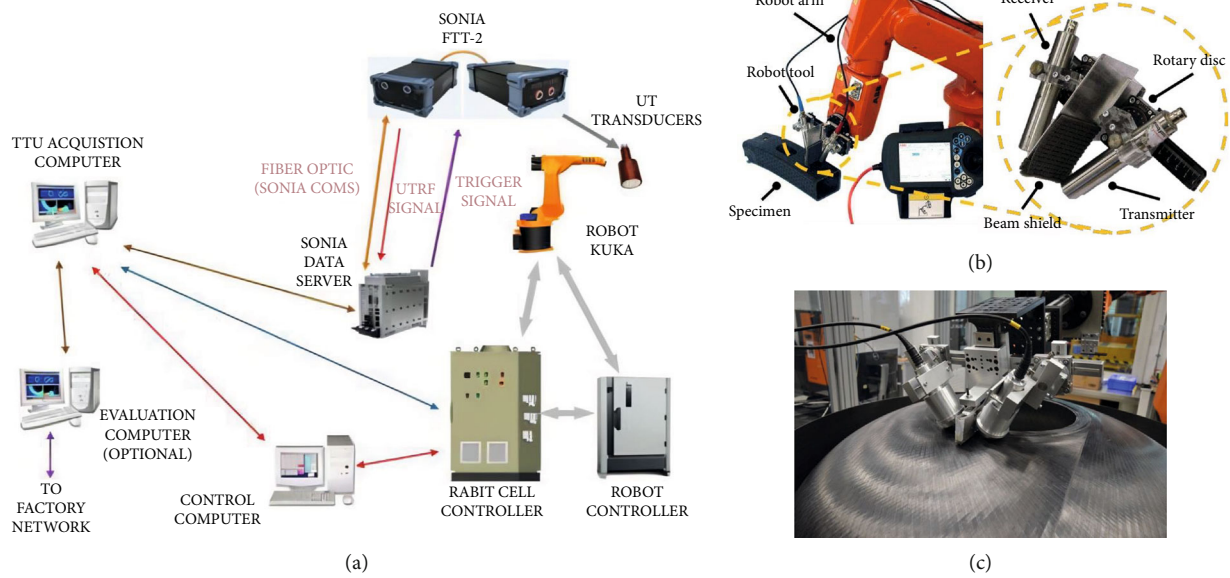


FIGURE 12: Joint robot combined with ACU C-scan. (a) New ACU C-scan system based on a joint robot [87]. (b) Joint robot to adjust the detection angle, the probe is installed on the rotating disc [88]. (c) A joint robot is being tested on a sample [89].

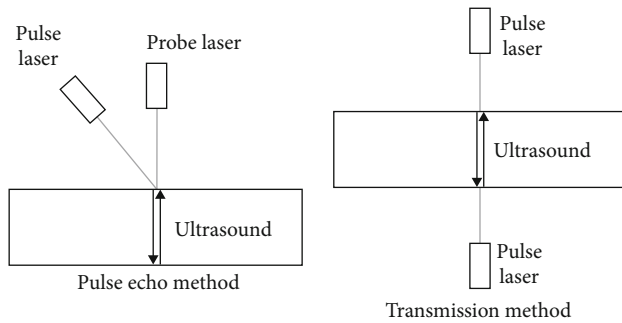


FIGURE 13: Laser is used to exciting and receives ultrasonic waves to detect defects in materials and structures. The commonly used detection methods include penetration method, pulse reflection method, surface wave method, and Lamb wave method. Among them, the pulse reflection method and penetration method are the most widely used [93].

metal sandwiches with CFRP and can automatically calculate the area of the defect; the team also introduced the technical framework and performance parameters of the world’s largest ACU C-scan system (see Figure 11), with an accuracy of less than 2.5 mm.

With the continuous development of modern science and technology, robots are also constantly combined with the ACU testing technology, so that the detection technology has been previously improved (see Figure 12). Cuevas et al. [87] proposed a new ACU C-scan system based on joint robots and applied it to the nondestructive testing of large composite components such as aircraft. Huber [88] combined the ACU Lamb wave detection technology with the joint robot technology to realize the ACU inside profiling scanning imaging detection of the aerospace composite cylindrical structure. Adebahr et al. [89] designed an ACU detection system based on a joint robot. Two ACU transduc-

ers arranged on the same side were used as excitation and receiving ultrasonic Lamb wave detection defects, and a six-axis joint robot was used as a scanning actuator. The system can realize three-dimensional profiling scanning imaging detection of large and complex structures.

**3.1.4. Laser Ultrasonic Testing.** The laser ultrasonic testing technology uses the thermal stress generated by the instantaneous thermal interaction between the laser pulse that can propagate in the air and the composite material to be tested to excite ultrasonic waves inside the material and then uses optical instruments to measure the sound waves noncontact (see Figure 13). Laser ultrasonic testing does not use ultrasonic couplants in the application and also has the characteristics of high resolution. The pulsed laser can also realize long-distance excitation and reception of ultrasonic waves under the condition that it is not perpendicular to the structure. Therefore, laser ultrasonic testing is also used in aviation. The detection of composite materials in high-precision fields such as aerospace has been applied, and this technology is especially suitable for rapid automatic detection of large and complex structures [90–92].

Chia et al. [94] used the Lamb wave excited by the laser to scan the CFRP material of the wing and initially realized the location of the impact damage. Zhou et al. [95] designed a set of laser ultrasonic testing systems based on all-optical excitation and reception, which can clearly distinguish the characteristics of delamination defects above 2 mm in carbon fiber composites, and verified that the application of laser ultrasonic testing technology to the feasibility of delamination detection of carbon fiber composites has realized the detection of impact damage of carbon fiber composites. Sun et al. [93] independently developed a noncontact laser ultrasonic NDT system (see Figure 14), which can effectively detect layered defects with an internal diameter of more than

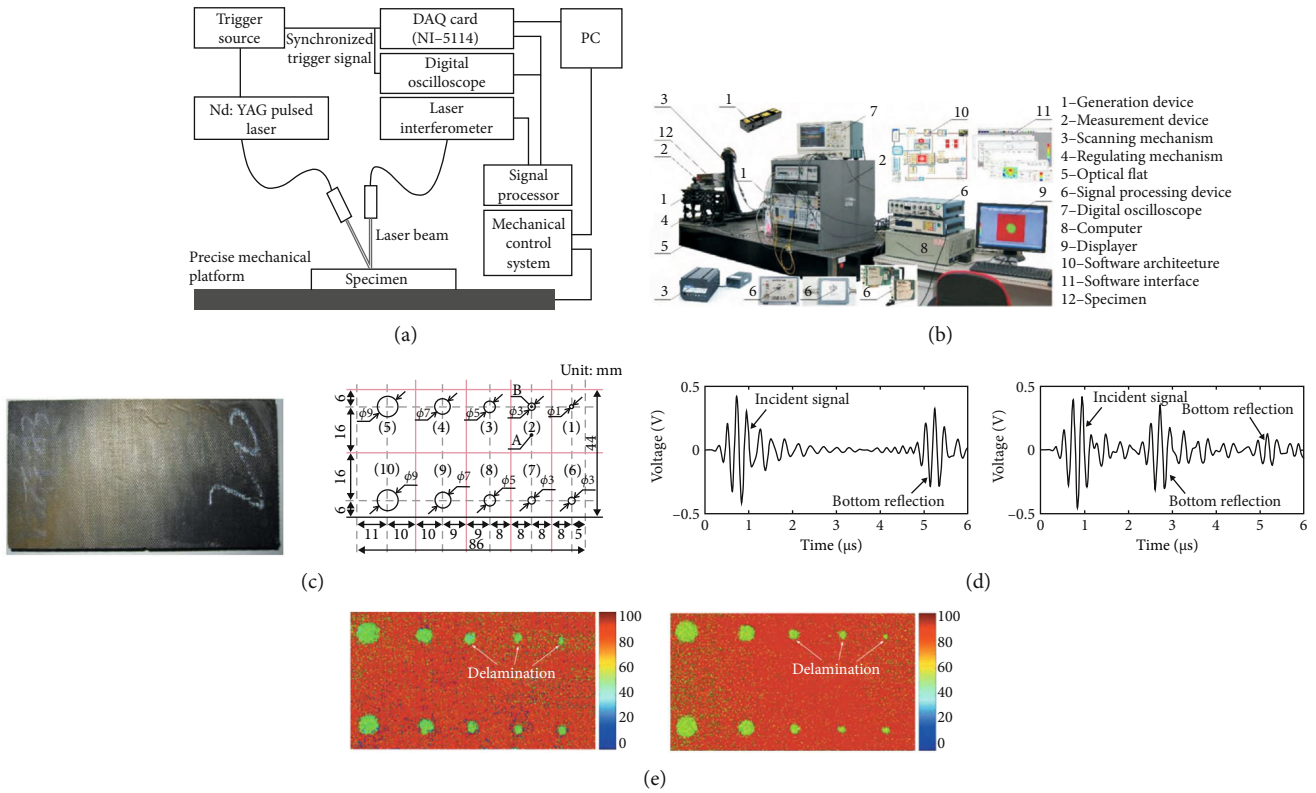


FIGURE 14: Laser ultrasonic testing of advanced composites [84]. (a) Basic theory of laser ultrasonic testing system. (b) Picture of the laser ultrasonic testing system. (c) Photo and layout of the CFRP specimen with internal delamination. (d) Narrow band signals extracted from the broadband laser ultrasonic signals measured at the intact (A) and defect (B) region of the CFRP specimen [96]. (e) Laser ultrasonic C-scan test of CFRP composite with delamination.

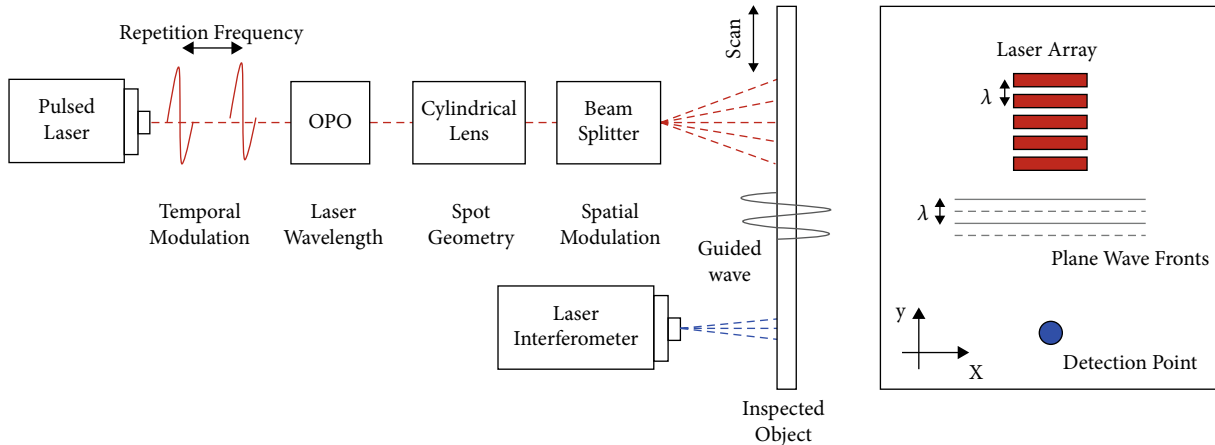


FIGURE 15: Ultrasonic guided wave inspection of composite materials based on laser excitation and detection methods [98].

2 mm in carbon fiber resin matrix composites and can also detect carbon fiber composite materials. Small size is layering at the edge of the fastening hole.

Nakahata et al. [97] used the thermal stress generated by the short-pulse laser and the instantaneous thermal interaction of the material to excite ultrasonic waves inside the material and used a photoacoustic microscope to scan the defects in the CFRP sample at a distance of  $50 \mu\text{m}$  in the X and Y directions. The three-dimensional reconstruction of

the delamination defect is carried out, the position and size of the defect can be accurately analyzed from the results, and the orientation of each fiber layer of the carbon fiber composite material is also reflected. Germany's Kelkel et al. [98] provided great potential for noncontact detection of fiber composites through the combination of laser excitation and detection of ultrasonic guided waves. As showed in Figure 15, the effects of laser wavelength, beam geometry, and spatiotemporal modulation of laser pulses on the

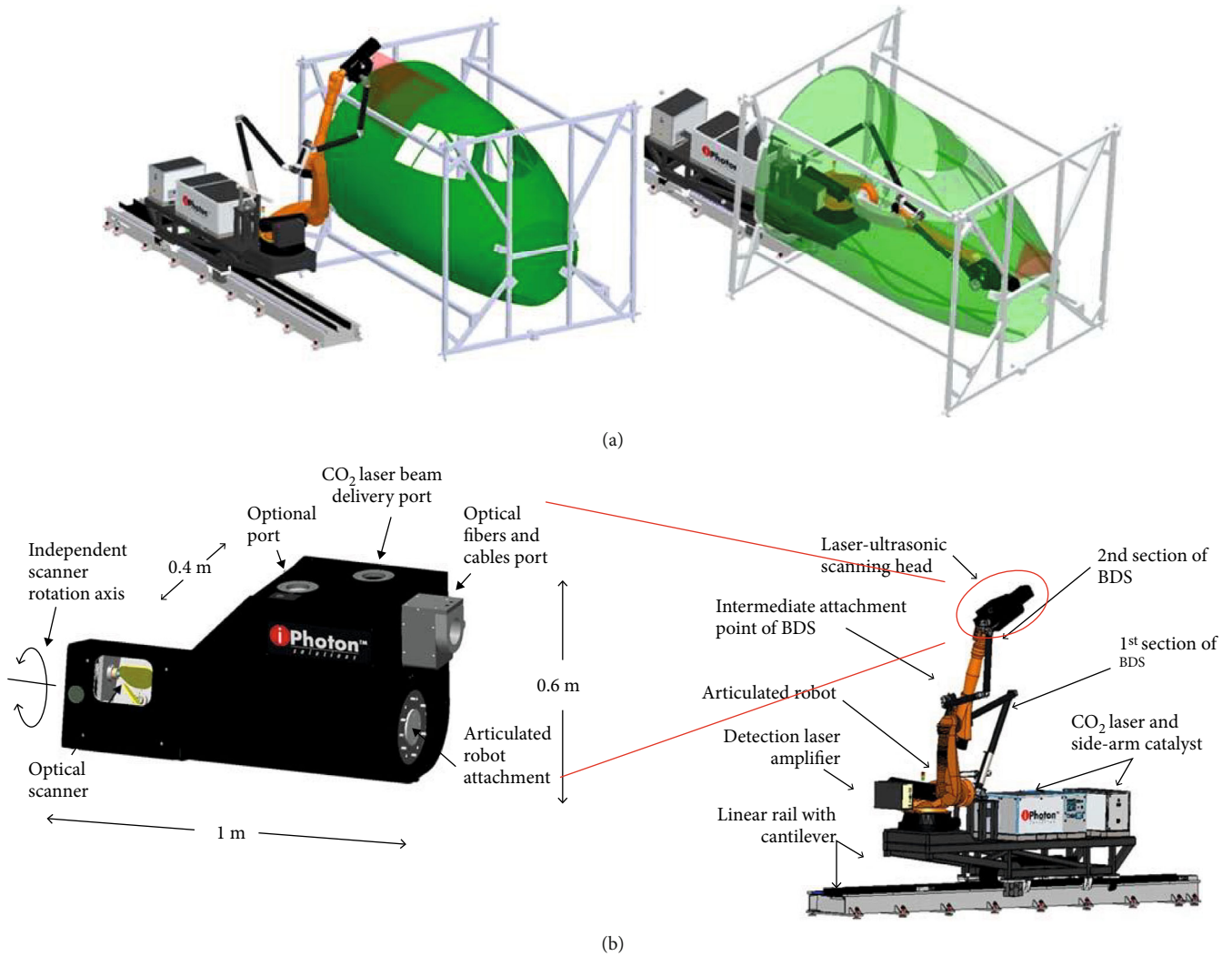


FIGURE 16: Laser ultrasonic detection system based on a joint robot [104]. (a) Illustrations of the inspection of the exterior (left figure) and interior (right figure) of large composite fuselage sections. (b) Schematic diagram of the laser detection system and laser-ultrasonic scanning head.

bandwidth, directivity, and amplitude of the generated acoustic wave are discussed. This method significantly improves the amplitude and signal-to-noise ratio of the ultrasonic guided wave signal.

Wang et al. [99] developed a multiscale ultrahigh-resolution laser ultrasonic inspection system for carbon fiber composites, which can identify microscale damage in CFRP and use a 2D laser with a high spatial resolution of  $60\ \mu\text{m}$  and a 3D image representation. Fischer et al. [100] designed a new noncontact laser ultrasonic inspection system based on optical microphones and used the transmission method to detect the internal defects of composite materials with quasistatic mechanical properties and low-speed shock response characteristics, which proves that the detection system has a high detection resolution. The Spanish Advanced Aviation Technology Center [101] realized the porosity detection of carbon fiber composites by laser longitudinal wave. Li et al. [102] verified the feasibility of laser ultrasonic detection for damage identification of complex-shaped aero-

space composites with curvature. Qiu et al. [103] used non-contact laser ultrasonic technology to detect aviation composite materials and imaged defect damage by extracting the energy and wavenumber information of ultrasonic signals. Dubois and Drake [104] combined laser ultrasonic inspection technology with robotics and developed a laser ultrasonic inspection system based on joint robots (see Figure 16). The system can detect the damage and defects of large-scale CFRP components in real-time. By installing a seven-axis robot with high flexibility on the guide rail for the positioning of the detector, and the system is equipped with a high-performance computer to process the collected data, automatic detection is realized.

**3.1.5. Laser Air-Coupled Ultrasonic Testing.** Bustamante et al. [105] used a hybrid laser air-coupled ultrasonic system CFRP for defect detection (see Figure 17); the system detects defects through the ultrasonic B-scan mode and determines the existence of internal defects in the material by the change



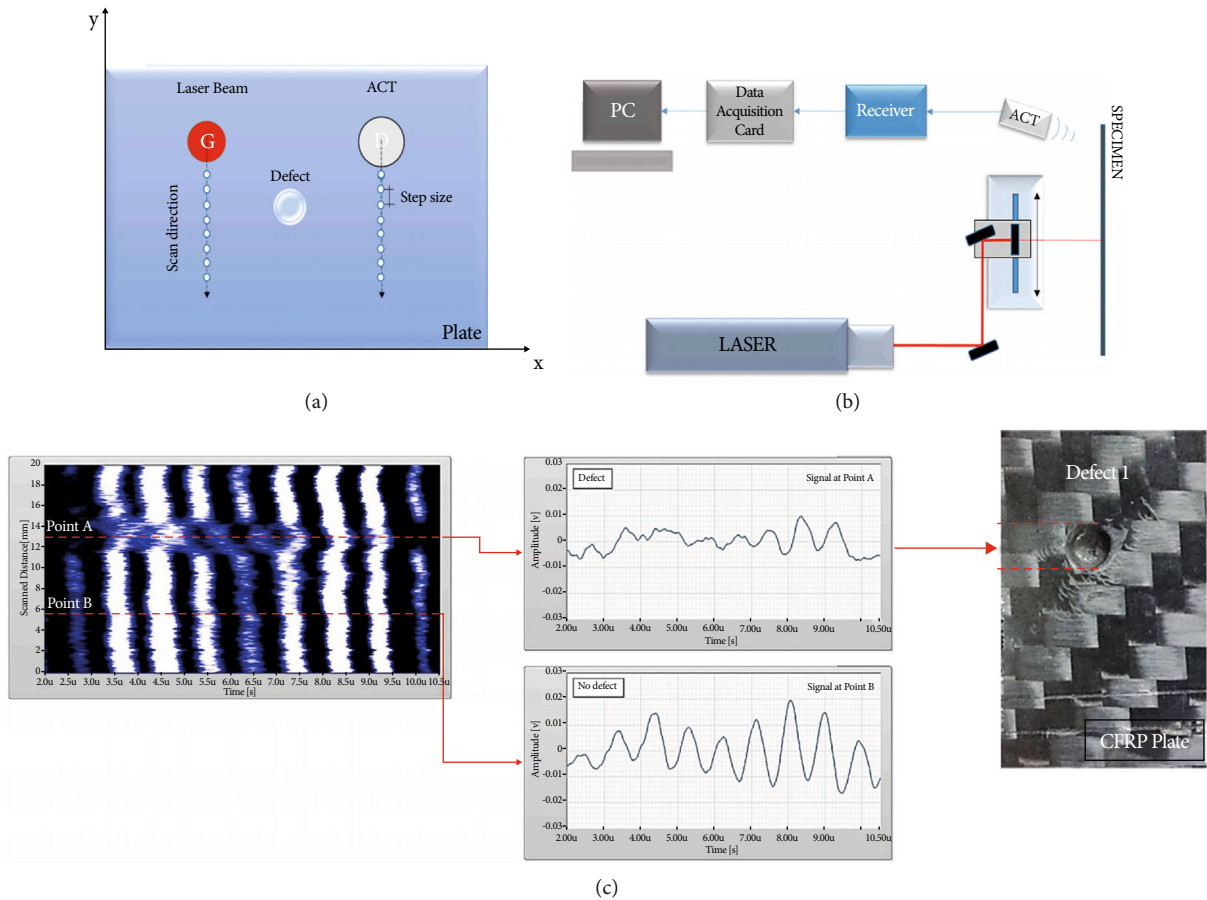


FIGURE 17: Scanning results of laser air-coupled ultrasonic system [105]. (a) Scanning direction and defects. (b) Scanning system. (c) Scanning results of CFRP defects.

of the acoustic wave amplitude. The defect detection of CFRP is shown in Figure 17(c).

Zeng et al. [106] proposed an air-coupled laser-ultrasonic system for detecting the microstructure and defects of woven carbon fiber cloth. Compared with PAU testing, it has higher resolution and defect detection and can detect the microstructure characterization of CFRP, as well as shallow and deep defects (see Figure 18).

### 3.2. Ultrasonic-Assisted Detection Methods

**3.2.1. Ultrasonic Infrared Thermal Imaging Detection.** Ultrasonic infrared thermal imaging detection technology is to apply a short-pulse, low-frequency ultrasonic waves on the surface of the object, and the ultrasonic waves are coupled to the interior of the object through the contact surface for transmission. If there are defects, such as cracks and delaminations in the composite material, under the excitation of ultrasonic waves, the two interfaces of the medium damage will contact and collide, and the mechanical energy of ultrasonic waves will be converted into heat energy under the action of friction, and then, the temperature clothing of the defect and its adjacent areas will increase. The change of the corresponding surface temperature field can be observed and recorded using an infrared thermal imager [107].

Yang et al. [108] carried out ultrasonic infrared thermal imaging NDT on the impact damage of CFRP specimens for UAVs (see Figure 19). The imaging defects are segmented, and the geometric distortion of the defects during the camera imaging process is also compensated (see Figure 19(d)). Umar et al. [109] studied the defect detection of composite materials by ultrasonic infrared imaging technology and successfully detected the damage defects of carbon fiber composite materials. This technology not only improves the efficiency of defect detection but also reduces the detection cost.

Chulkov et al. [110] added two infrared image sequences obtained under optical and ultrasonic excitation (see Figure 20) and then detected the defects of CFRP, realizing the detection of small opening cracks with low thermal resistance.

**3.2.2. Fiber Ultrasonic Testing.** Hudson et al. [111] designed a real-time online monitoring system based on PSFBG, and the results show that the system can detect the ultrasonic signal propagating in CFRP and then can realize the detection of defects. Wang et al. [112] studied a fiber grating ultrasonic testing system to solve the problem of ultrasonic nonlinearity caused by cracks in the composite matrix (see Figure 21), by introducing a phase-shifted fiber Bragg grating (PSFBG)

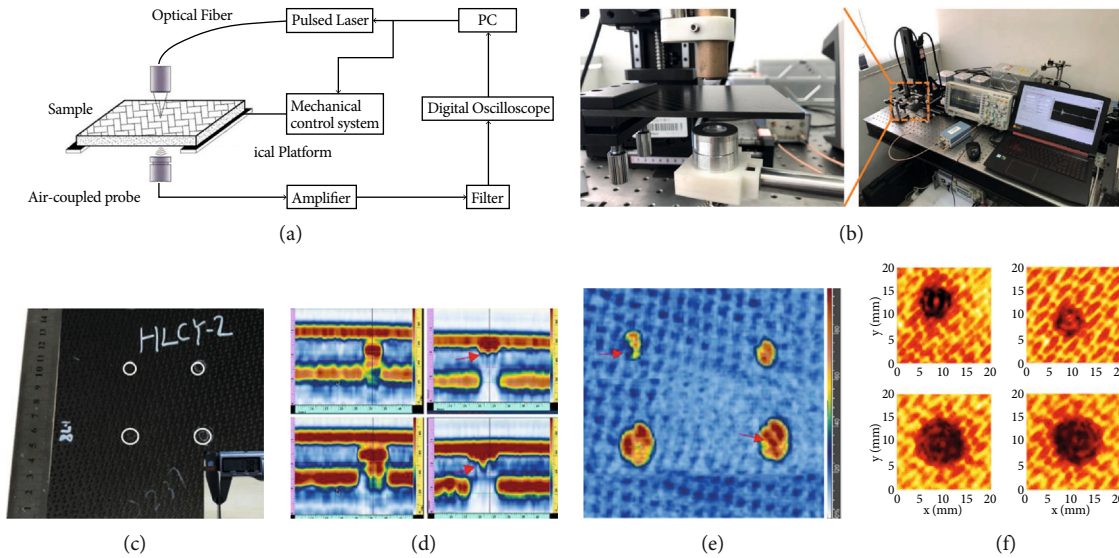


FIGURE 18: Air-coupled laser hybrid system [106]. (a) Schematic diagram of the system. (b) Photo of the experimental setup. (c) Air-coupled laser ultrasound imaging of CFRP samples. (d) 5 MHz phased array B-scan image. (e) 20 MHz phased-array C-scan image. (f) Air-coupled laser scan image.

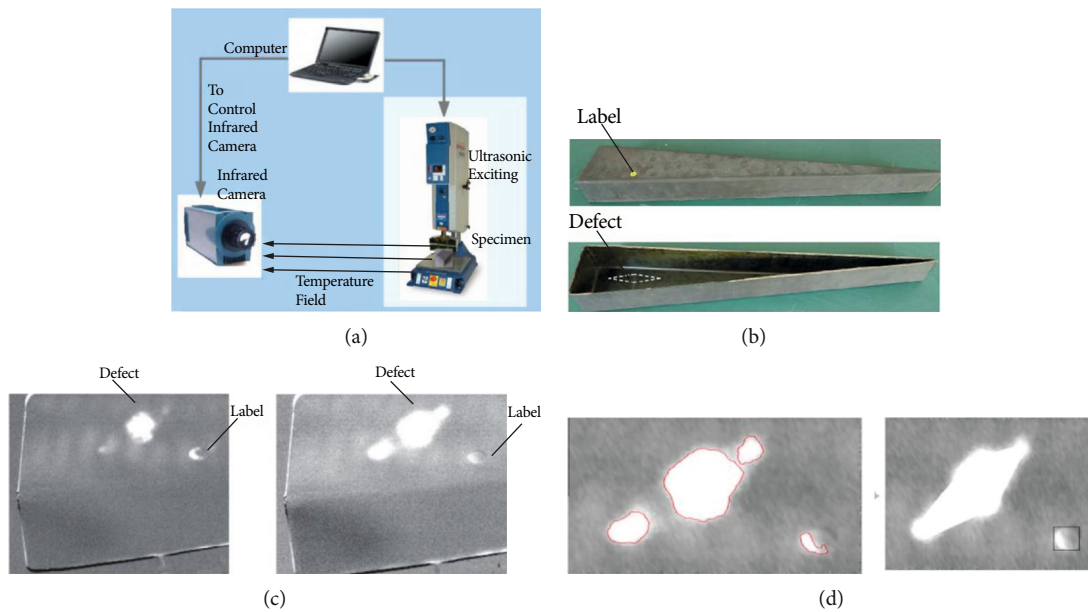


FIGURE 19: Ultrasonic infrared thermal imaging CFRP inspection [108]. (a) Experimental setup. (b) Before and after photos of CFRP specimens. (c) Before and after thermal imaging inspection results. (d) Defect segmentation results (left figure) and defect compensation results (right figure).

to improve the sensitivity and bandwidth of ultrasonic detection and realize the damage assessment of CFRP matrix cracks.

#### 4. Problems and Development Trends

(1) The components of CFRP in different fields often have the characteristics of complex structure, special material, and rapid upgrading, which put forward higher requirements for the corresponding advanced ultrasonic NDT technologies and equipment such as

array ultrasound, air-coupled ultrasound, and laser ultrasound. High precision, automation, intelligence, and engineering have gradually become the development trend of advanced ultrasonic testing technology in the future

(2) The difficulties and key points in the detection of CFRP composites, especially in the field of aerospace. The detection of various defects of CFRP needs to be combined with various advanced ultrasonic testing and imaging technologies to cross and integrate to improve the detection efficiency. At the

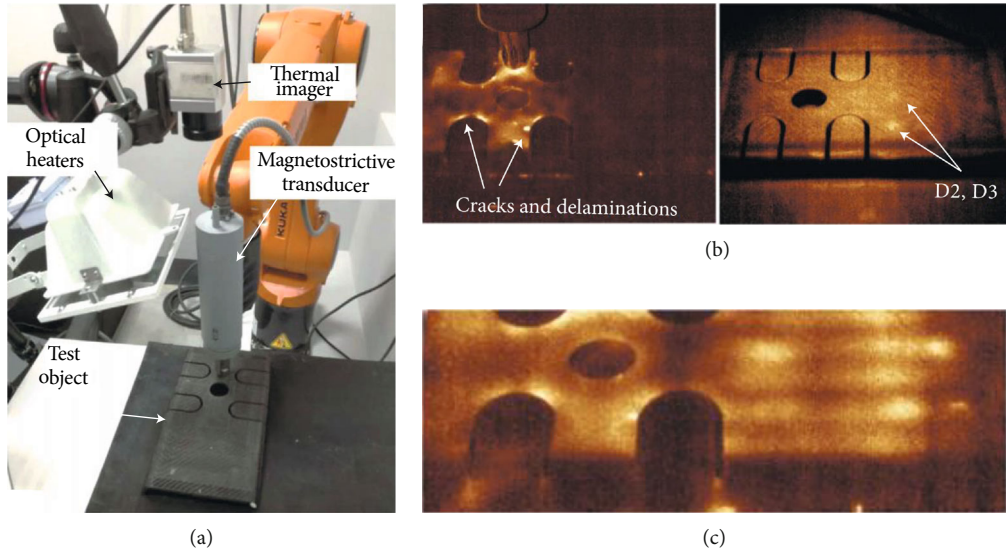


FIGURE 20: Optical and ultrasonic excitation infrared imaging detection [110]. (a) Experimental setup and experimental samples. (b) Ultrasonic excitation (left figure) and optical excitation (right figure) infrared imaging. (c) Infrared synthesis detection diagram.

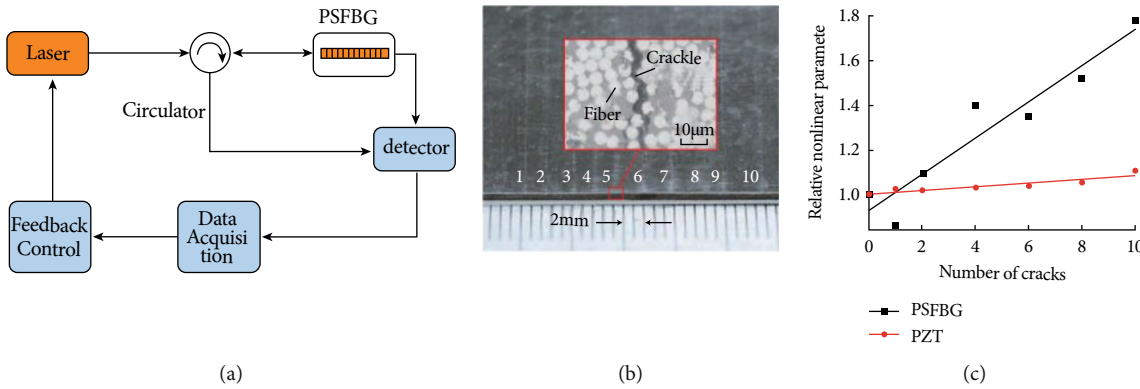


FIGURE 21: Fiber Bragg Grating Ultrasonic Testing System [112]. (a) System schematic diagram. (b) Experimental sample. (c) Relationship between the number of cracks and nonlinear parameters (different sensors).

same time, basic research on the acoustic characteristics and detection model of CFRP composites is carried out to improve the detection accuracy and reliability of CFRP

- (3) In view of the advanced ultrasonic testing technology, such as array ultrasonic, ACU, and laser ultrasonic automatic testing technology, it is necessary to determine the relevant defect detection methods, position calibration, type determination, and parallel control technology according to the research of complex CFRP components tested and further improve the accuracy and efficiency of automatic testing combined with other advanced NDT technologies
- (4) With the rapid development of artificial intelligence, the defects of CFRP can be detected by combining various ultrasonic technologies, and the relevant parameters can be optimized by using deep learning and other methods. The robot technology can help the detection technology to realize real-time detec-

tion, automation, intelligence, and other operations and can be used for NDT of large and complex CFRP components and high precision areas to achieve better detection results

### 5. Conclusion

Recent research shows that ultrasonic is still the most active hot spot in the field of composite materials. Using the appropriate ultrasonic method and ultrasonic technology, not only the defects can be characterized, evaluated, and qualitatively and quantitatively detected but also the automation and visualization of carbon fiber composite structure can be easily realized, and intelligent NDT and evaluation. In the actual test, appropriate test methods should be selected according to the characteristics of various carbon fiber composites, or multiple methods should be used to complement each other to complete different test tasks. The outstanding advantages of ultrasonic NDT are that it is harmless to human body, low cost, and easy to operate. It will certainly



play a greater role in the field of NDT of composite materials. However, in the face of the continuous introduction of new composite materials, new processes, new structures, and new testing requirements, there are still many technical problems and difficulties in ultrasonic NDT and electronic testing.

## Abbreviations

CFRP: Carbon fiber-reinforced polymer

NDT: Nondestructive testing

PAU: Phased array ultrasonic

ACU: Air-coupled ultrasonic.

## Conflicts of Interest

The authors declare that they have no conflicts of interest.

## Acknowledgments

This work was supported in part by the National Natural Science Foundation of China under Grant 51875477 and Grant 51475013 and in part by the Fundamental Research Funds for the Central Universities under Grant 3102020ZDHKY01.

## References

- [1] W. J. Cantwell and J. Morton, "The impact resistance of composite materials—a review," *Composites*, vol. 22, no. 5, pp. 347–362, 1991.
- [2] D. Shanyi, "Advanced composite materials and aerospace engineering," *Acta Materiae Compositae Sinica*, vol. 24, no. 1, pp. 1–12, 2007.
- [3] D. Shanyi, "Composite material innovation drives industrial development," *Science & Technology Review*, vol. 34, no. 8, 2016.
- [4] B. P. Sharma, G. S. Rao, S. Gupta, P. Gupta, and A. Prasad, *Advances in engineering materials*, Springer, Singapore, 2021.
- [5] M. R. Mitchell, R. E. Link, C. K. Liew et al., "Inspections of helicopter composite airframe structures using conventional and emerging nondestructive testing methods," *Journal of Testing and Evaluation*, vol. 39, no. 6, pp. 1011–1022, 2011.
- [6] K. Diamanti and C. Soutis, "Structural health monitoring techniques for aircraft composite structures," *Progress in Aerospace Sciences*, vol. 46, no. 8, pp. 342–352, 2010.
- [7] L. G. I. Bennett, W. J. Lewis, and P. C. Hungler, "The development of neutron radiography and tomography on a SLOWPOKE-2 reactor," *Physics Procedia*, vol. 43, pp. 21–33, 2013.
- [8] L. Zhang, "The application of composite fiber materials in sports equipment," in *2015 international conference on education, management, information and medicine*, pp. 450–453, Atlantis Press, 2015.
- [9] K. Friedrich and A. A. Almajid, "Manufacturing aspects of advanced polymer composites for automotive applications," *Applied Composite Materials*, vol. 20, no. 2, pp. 107–128, 2013.
- [10] C. Y. Chua, H. C. Liu, N. Di Trani et al., "Carbon fiber reinforced polymers for implantable medical devices," *Biomaterials*, vol. 271, article 120719, 2021.
- [11] F. He, Z. Wang, and L. Shi, "Ultrasonic testing technique for the inspection of defects in the corner of composites," *Journal of Materials Engineering*, vol. 1, no. 7, pp. 80–84, 2011.
- [12] X. L. Liang, X. W. Xu, and Z. Y. Lin, "Fatigue performance of composite laminates after low-velocity impact," *Journal of Materials Engineering*, vol. 44, no. 12, pp. 100–106, 2016.
- [13] F. C. He, Z. Wang, L. J. Shi, Y. Liu, D. Yang, and X. Wang, "Application and development of NDT for fiber reinforced polymer matrix composites used in aviation," *Non-destructive Testing*, vol. 40, no. 11, pp. 29–41, 2018.
- [14] Z. J. Quan, J. L. Liu, F. Fang, G. X. Wang, and F. Y. Jiang, "Effect of V-shaped Pit area ratio on quantum efficiency of blue InGaN/GaN multiple-quantum well light-emitting diodes," *Optical and Quantum Electronics*, vol. 48, no. 3, pp. 195.1–195.8, 2016.
- [15] C. A. R. Díaz, C. Marques, M. Domingues et al., "A cost-effective edge-filter based FBG interrogator using catastrophic fuse effect micro-cavity interferometers," *Measurement*, vol. 124, pp. 486–493, 2018.
- [16] Z. Wang, R. Singh, C. Marques, R. Jha, B. Zhang, and S. Kumar, "Taper-in-taper fiber structure-based LSPR sensor for alanine aminotransferase detection," *Optics Express*, vol. 29, no. 26, pp. 43793–43810, 2021.
- [17] A. G. Leal-Junior, A. Frizera, C. Marques et al., "Polymer optical fiber for angle and torque measurements of a series elastic actuator's spring," *Journal of Lightwave Technology*, vol. 36, no. 9, pp. 1698–1705, 2018.
- [18] A. G. Leal-Junior, C. Marques, A. Frizera, and M. J. Pontes, "Dynamic mechanical analysis on a polymethyl methacrylate (PMMA) polymer optical fiber," *IEEE Sensors Journal*, vol. 18, no. 6, pp. 2353–2361, 2018.
- [19] S. Steve, "Manufacturing engineering and technology," *Upper Saddle River*, vol. 30, no. 3, pp. 468–476, 2013.
- [20] Y. Liu, B. Zwingmann, and M. Schlaich, "Carbon fiber reinforced polymer for cable structures—a review," *Polymers*, vol. 7, no. 10, pp. 2078–2099, 2015.
- [21] D. Ozkan, M. S. Gok, and A. C. Karaoglanli, "Carbon fiber reinforced polymer (CFRP) composite materials, their characteristic properties, industrial application areas and their machinability," in *Advanced Structured Materials*, pp. 235–253, Springer, Cham, 2020.
- [22] J. Wen, Z. Xia, and F. Choy, "Damage detection of carbon fiber reinforced polymer composites via electrical resistance measurement," *Composites Part B: Engineering*, vol. 42, no. 1, pp. 77–86, 2011.
- [23] S. R. Karnik, V. N. Gaitonde, J. C. Rubio, A. E. Correia, A. M. Abrão, and J. P. Davim, "Delamination analysis in high speed drilling of carbon fiber reinforced plastics (CFRP) using artificial neural network model," *Materials & Design*, vol. 29, no. 9, pp. 1768–1776, 2008.
- [24] G. Marsh, "Airbus A350 XWB update," *Reinforced Plastics*, vol. 54, no. 6, pp. 20–24, 2010.
- [25] A. Al-Lami, P. Hilmer, and M. Sinapius, "Eco-efficiency assessment of manufacturing carbon fiber reinforced polymers (CFRP) in aerospace industry," *Aerospace Science and Technology*, vol. 79, pp. 669–678, 2018.
- [26] H. Emathing, "Development of a CFRP transmission housing for a formula student racing car," *ATZextra worldwide*, vol. 22, no. S2, pp. 36–39, 2017.

- [27] *Carbon fiber innovations in the medical industry*, 2020, <https://www.pcmi-mfg.com/blog/carbon-fiber-innovations-in-the-medical-industry>.
- [28] F. E. Sino, *Why use carbon fiber sports knee pads?*, 2019, <https://www.carbonfibercustom.com/why-use-carbon-fiber-sports-knee-pads>.
- [29] J. Llobet, P. Maimí, Y. Essa, and F. Martin de la Escalera, "Progressive matrix cracking in carbon/epoxy cross-ply laminates under static and fatigue loading," *International Journal of Fatigue*, vol. 119, pp. 330–337, 2019.
- [30] J. J. Zeng, W. Y. Gao, and F. Liu, "Interfacial behavior and debonding failures of full-scale CFRP-strengthened H-section steel beams," *Composite Structures*, vol. 201, pp. 540–552, 2018.
- [31] M. Y. Fard, B. Raji, and H. Pankretz, "Correlation of nano-scale interface debonding and multimode fracture in polymer carbon composites with long-term hygrothermal effects," *Mechanics of Materials*, vol. 150, article 103601, 2020.
- [32] L. Lassila, F. Keulemans, E. Säilynoja, P. K. Vallittu, and S. Garoushi, "Mechanical properties and fracture behavior of flowable fiber reinforced composite restorations," *Dental Materials*, vol. 34, no. 4, pp. 598–606, 2018.
- [33] L. Longbiao, "Modeling first matrix cracking stress of fiber-reinforced ceramic-matrix composites considering fiber fracture," *Theoretical and Applied Fracture Mechanics*, vol. 92, pp. 24–32, 2017.
- [34] L. Yao, H. Cui, R. C. Alderliesten, Y. Sun, and L. Guo, "Thickness effects on fibre-bridged fatigue delamination growth in composites," *Composites Part A: Applied Science and Manufacturing*, vol. 110, pp. 21–28, 2018.
- [35] R. B. Ladani, K. Pingkarawat, A. T. T. Nguyen, C. H. Wang, and A. P. Mouritz, "Delamination toughening and healing performance of woven composites with hybrid z-fibre reinforcement," *Composites Part A: Applied Science and Manufacturing*, vol. 110, pp. 258–267, 2018.
- [36] A. R. Chambers, J. S. Earl, C. A. Squires, and M. A. Suhot, "The effect of voids on the flexural fatigue performance of unidirectional carbon fibre composites developed for wind turbine applications," *International journal of fatigue*, vol. 28, no. 10, pp. 1389–1398, 2006.
- [37] S. Y. Park, W. J. Choi, and H. S. Choi, "The effects of void contents on the long-term hygrothermal behaviors of glass/epoxy and GLARE laminates," *Composite Structures*, vol. 92, no. 1, pp. 18–84, 2010.
- [38] V. K. Srivastava, T. Gries, D. Veit, T. Quadflieg, B. Mohr, and M. Kolloch, "Effect of nanomaterial on mode I and mode II interlaminar fracture toughness of woven carbon fabric reinforced polymer composites," *Engineering Fracture Mechanics*, vol. 180, pp. 73–86, 2017.
- [39] N. C. Huang and X. Y. Liu, "Debonding and fiber pull-out in reinforced composites," *Theoretical and Applied Fracture Mechanics*, vol. 21, no. 3, pp. 157–176, 1994.
- [40] D. Kreculj and B. Rašuo, "Review of impact damages modeling in laminated composite aircraft structures," *Tehnicki vjesnik/Technical Gazette*, vol. 20, no. 3, 2013.
- [41] M. R. Wisnom, "The role of delamination in failure of fibre-reinforced composites," *Philosophical Transactions of the Royal Society A: Mathematical, Physical and Engineering Sciences*, vol. 370, no. 1965, pp. 1850–1870, 2012.
- [42] A. Krishnamoorthy, S. R. Boopathy, and K. Palanikumar, "Delamination analysis in drilling of CFRP composites using response surface methodology," *Journal of Composite Materials*, vol. 43, no. 24, pp. 2885–2902, 2009.
- [43] J. W. Shi, G. L. Xun, and J. Liu, "Mesoscopic characteristics of voids in CFRP composites fabricated with unidirectional and woven prepreg," *Journal of Central South University: Natural Science Edition*, vol. 51, no. 3, pp. 628–640, 2020.
- [44] S. Hernández, F. Sket, C. González, and J. Llorca, "Optimization of curing cycle in carbon fiber-reinforced laminates: void distribution and mechanical properties," *Composites Science & Technology*, vol. 85, pp. 73–82, 2013.
- [45] L. I. Songping, G. U. Enming, and Z. H. Qianlin, "Evaluation of composite materials by ultrasonic C-scan in depths," *Non-destructive Testing*, vol. 23, no. 1, pp. 13–15, 2001.
- [46] R. M. Wu, X. J. Zhou, and K. B. Wang, "Study on multisensor information fusion in ultrasonic C-scan system of composite material," *Journal of Sensing Technology*, vol. 3, pp. 561–564, 2005.
- [47] T. Hasiotis, E. Badogiannis, and N. G. Tsouvalis, "Application of ultrasonic C-scan techniques for tracing defects in laminated composite materials," *Strojnikski Vestnik-Journal of Mechanical Engineering*, vol. 2011, no. 3, pp. 192–203, 2011.
- [48] M. Y. Shiino, M. C. Faria, E. C. Botelho, and P. C. Oliveira, "Assessment of cumulative damage by using ultrasonic C-scan on carbon fiber/epoxy composites under thermal cycling," *Materials Research*, vol. 15, no. 4, pp. 495–499, 2012.
- [49] W. Gao, "A discussion on the influence of the scanning directions on the scanning results of the ultrasonic water spraying C-scan," *Non-destructive Testing*, vol. 44, no. 2, pp. 13–16, 2020.
- [50] D. K. Hsu, F. E. I. Dong, and L. I. U. Zhanjie, "Ultrasonically mapping the ply layout of composite laminates," *Materials Evaluation*, vol. 60, no. 9, pp. 1099–1106, 2002.
- [51] J. Patronen, C. Stenroos, M. Virkkunen, S. Papula, and T. Sarikka, "Inspection of carbonFiber-Titanium-carbonFiberstepped-Lap Joint," in *European Conference on NDT*, NDT.net, 2018.
- [52] C. Y. Zhu, K. Xiong, and K. Bian, "Experiment on disbond detection on CFRP T-joint," *Journal of Composite Materials*, vol. 29, no. 6, pp. 237–242, 2012.
- [53] B. Liu, L. Qiu, S. Yuan, and C. Wang, "Damage imaging and localization method based on multi-dimension arrays and spatial filter without wave velocity," *Journal of Composite Materials*, vol. 31, no. 3, pp. 835–844, 2014.
- [54] B. Liu, L. Qiu, S. Yuan, H. Shao, and H. Zhang, "The probability imaging algorithm of composite T-joint damage monitoring," *Journal of Vibration Measurement & Diagnosis*, vol. 35, no. 3, pp. 519–524, 2015.
- [55] Q. Bao, S. F. Yuan, L. Qiu, and W. Tongguang, "A damage imaging method based on MUSIC algorithm of linear sensor array for composite structure," *Journal of Composite Materials*, vol. 34, no. 2, pp. 456–462, 2017.
- [56] V. K. Wong, Y. Hu, Z. W. Tham et al., "Measurement of elastic constant matrix of carbon fiber composites with an ultrasonic 2D-Array transducer," *IEEE Sensors Journal*, vol. 22, no. 6, pp. 5562–5570, 2022.
- [57] Y. S. Liu, Y. Li, L. C. Teng, and Z. Zhengqian, "Research on ultrasonic testing method for carbon fiber laminated composite using ultrasonic analytical signal," *Journal of Mechanical Engineering*, vol. 56, no. 24, pp. 31–39, 2020.
- [58] C. Nageswaran, C. R. Bird, and R. Takahashi, "Phased array scanning of artificial and impact damage in carbon fibre

- reinforced plastic (CFRP),” *Insight-NDT and Condition Monitoring*, vol. 48, no. 3, pp. 155–159, 2006.
- [59] N. Xu, Z. Zhou, W. Liu, H. Zhou, and G. Yu, “Ultrasonic phased array inspection method for the corner of L-shaped components,” *Acta Aeronautica et Astronautica Sinica*, vol. 34, no. 2, pp. 419–425, 2013.
- [60] Z. D. Y. Guang and Z. Z. X. Na, *Ultrasonic phased array inspection for the corner of composite components*, Journal of Beijing University of Aeronautics and Astronautics, 2013.
- [61] C. Meola, S. Boccardi, G. M. Carlomagno, N. D. Boffa, E. Monaco, and F. Ricci, “Nondestructive evaluation of carbon fibre reinforced composites with infrared thermography and ultrasonics,” *Composite Structures*, vol. 134, pp. 845–853, 2015.
- [62] V. Kappatos, G. Asfis, K. Salonitis et al., “Theoretical assessment of different ultrasonic configurations for delamination defects detection in composite components,” *Procedia CIRP*, vol. 59, pp. 29–34, 2017.
- [63] Z. L. Zhang, M. B. Fan, B. H. Cao, and Z. D. Fang, “Characterization of delamination defects in carbon fiberreinforced plastics using ultrasonic phased array testing,” *Science Technology and Engineering*, vol. 18, no. 18, pp. 43–47, 2018.
- [64] M. A. Caminero, I. García-Moreno, G. P. Rodríguez, and J. M. Chacón, “Internal damage evaluation of composite structures using phased array ultrasonic technique: impact damage assessment in CFRP and 3D printed reinforced composites,” *Composites Part B: Engineering*, vol. 165, pp. 131–142, 2019.
- [65] H. B. Zhang and B. Q. Du, “Experiment on phased ultrasonic inspection technology of delamination damage of carbon fiber structure,” *Non-destructive Testing*, vol. 42, no. 4, pp. 46–49, 2020.
- [66] H. Y. Cao, M. Y. Ma, G. Q. Ding et al., “Delamination defects testing and evaluation of composite laminates using phased array ultrasonic technique,” *Materials Engineering*, vol. 49, no. 2, pp. 149–157, 2021.
- [67] J. Li, W. Guo, X. X. Yang, Y. Q. Huang, X. L. Zhan, and S. J. Jin, “A flaw classification method for ultrasonic phased array inspection of CFRP,” *Journal of Tianjin University*, vol. 48, no. 8, pp. 750–756, 2015.
- [68] A. Lamarre, “Improved inspection of composite wind turbine blades with accessible advanced ultrasonic phased array technology,” in *15th Asia Pacific conference for NDT (APCNDT2017)*, pp. 1–8, Singapore, 2017.
- [69] E. Grondin, “Adaptive Focusing Technology for the Inspection of Variable Geometry Composite Material,” in *12th European Conference on NDT*, Gothenburg, Sweden, 2018.
- [70] X. F. Li, R. L. Fu, and B. L. Yang, “Full focus 3D phased array ultrasonic testing of carbon fiber composites,” *Non-destructive Testing*, vol. 45, no. 4, pp. 31–34, 2021.
- [71] D. M. Zhang, G. Yu, and Z. G. Zhou, “Ultrasonic phased array inspection for the corner of composite components,” *Journal of Beijing University of Aeronautics and Astronautics*, vol. 39, no. 5, pp. 688–692, 2013.
- [72] S. J. Li, Y. C. Zhou, R. Chen, C. P. Li, X. Y. Qiu, and P. N. Li, “Simulation and experimental study of CFRP micro cutting considering voids defects,” *Journal of Composite Materials*, vol. 39, pp. 1–12, 2022.
- [73] A. Aschy, N. Terrien, S. Robert, and M. Bentahar, “Ultrasonic Phased Array Imaging of Heterogeneous Composite Structures,” in *12th European conference on Non-Destructive Testing*, Gothenburg, Sweden, 2018.
- [74] H. Y. Cao, M. S. Jiang, M. Y. Ma et al., “Parameter optimization method for delamination defects detection of composite laminate using phased array ultrasonic,” *Materials Engineering*, vol. 48, no. 9, pp. 158–165, 2020.
- [75] Z. Y. Li, F. F. Liu, Y. S. Yang, and S. P. Liu, “Ultrasonic phased array inspection of composite fuselage panel,” *Aeronautical Manufacturing Technology*, vol. 64, no. 19, pp. 82–89, 2021.
- [76] J. Habermehl, A. Lamarre, and O. Ndt, “Ultrasonic Phased Array Tools for Composite Inspection during Maintenance and Manufacturing,” in *17th World Conference on Nondestructive Testing*, pp. 25–28, Shanghai, China, 2008.
- [77] R. J. Freemantle, N. Hankinson, and C. J. Brotherhood, “Rapid phased array ultrasonic imaging of large area composite aerospace structures,” *Insight-NDT and Condition Monitoring*, vol. 47, no. 3, pp. 129–132, 2005.
- [78] W. Hillger, A. Szewieczek, D. Ilse, and L. Bühling, “Challenges and new developments for air coupled ultrasonic imaging,” in *the 12th European Conference of Non-Destructive Testing in Gothenburg*, Sweden, 2018.
- [79] B. Q. Ma and Z. G. Zhou, “Progress and development trends of composite structure evaluation using noncontact nondestructive testing techniques in aviation and aerospace industries,” *Acta Aeronautica et Astronautica Sinica*, vol. 35, no. 7, pp. 1787–1803, 2014.
- [80] J. Salazar, A. Turó, J. A. Chávez, J. A. Ortega, and M. J. Garcia, “High-power high-resolution pulser for air-coupled ultrasonic NDE applications,” *IEEE Transactions on Instrumentation and Measurement*, vol. 52, no. 6, pp. 1792–1798, 2003.
- [81] R. Kažys, L. Mažeika, and E. Žukauskas, “Investigation of accurate imaging of the defects in composite materials using ultrasonic air-coupled technique,” *International Journal of Materials and Product Technology*, vol. 41, no. 1-4, pp. 105–116, 2011.
- [82] R. Steinhausen, M. Kiel, C. Pientschke, H. J. Münch, A. Mück, and K. Hahn, “New approaches to air-coupled ultrasound testing of composite lightweight materials,” in *19th World Conference on NDT (WCNDT)*, Munich/Germany, 2016.
- [83] K. Imielińska, M. Castaings, R. Wojtyra, J. Haras, E. L. Clezio, and B. Hosten, “Air-coupled ultrasonic C-scan technique in impact response testing of carbon fibre and hybrid: glass, carbon and Kevlar/epoxy composites,” *Journal of Materials Processing Technology*, vol. 157-158, pp. 513–522, 2004.
- [84] J. J. Peters, D. J. Barnard, and D. K. Hsu, “Development of a fieldable air-coupled ultrasonic inspection system,” *AIP Conference Proceedings*, vol. 700, no. 1, pp. 1368–1375, 2004.
- [85] J. J. Chang and C. Lu, “Research on principle and application of non-contact air-coupled ultrasonic testing,” *Non-destructive Testing*, vol. 37, no. 4, pp. 6–11, 2013.
- [86] H. Li and Z. Zhou, “Detection and characterization of debonding defects in aeronautical honeycomb sandwich composites using noncontact air-coupled ultrasonic testing technique,” *Applied Sciences*, vol. 9, no. 2, p. 283, 2019.
- [87] E. Cuevas, S. Hernandez, and E. Cabellos, “Robot-based solutions for NDT inspections: Integration of laser ultrasonics and air coupled ultrasounds for aeronautical components,” in *25th ASNT Research Symposium*, pp. 39–46, Astor Crowne Plaza New Orleans, New Orleans LA, United States, 2016.



- [88] A. Huber, "NDT of future rocket boosters using air-coupled ultrasound," in *19th World Conference on NDT*, pp. 1–9, Internationales Congress Center, 2016.
- [89] W. Adebahr, Y. Bernhardt, and M. Kreutzbruck, "3D-robotized air-coupled ultrasound measurements of large components," in *Proceeding of the 19th World Conference on NDT*, Germany, Munich, 2016.
- [90] R. M. White, "Generation of elastic waves by transient surface heating," *Journal of Applied Physics*, vol. 34, no. 12, pp. 3559–3567, 1963.
- [91] S. G. Pierce, B. Culshaw, W. R. Philp, F. Lecuyer, and R. Farlow, "Broadband lamb wave measurements in aluminium and carbon/glass fibre reinforced composite materials using non-contacting laser generation and detection," *Ultrasonics*, vol. 35, no. 2, pp. 105–114, 1997.
- [92] S. Yashiro, J. Takatsubo, and N. Toyama, "An NDT technique for composite structures using visualized lamb-wave propagation," *Composites Science and Technology*, vol. 67, no. 15–16, pp. 3202–3208, 2007.
- [93] G. K. Sun, Z. G. Zhou, and X. Chen, "Application of laser ultrasonic technology for nondestructive testing of aerospace composites," *Failure Analysis and Prevention*, vol. 11, no. 5, pp. 276–282, 2016.
- [94] C. C. Chia, J. R. Lee, C. Y. Park, and H. M. Jeong, "Laser ultrasonic anomalous wave propagation imaging method with adjacent wave subtraction: application to actual damages in composite wing," *Optics & Laser Technology*, vol. 44, no. 2, pp. 428–440, 2012.
- [95] A. G. Zhou, G. K. Sun, and Y. Li, "Application of advanced nondestructive testing technologies for the detection of defects in composites," *Aerospace Manufacturing Technology*, vol. 4, pp. 30–35, 2016.
- [96] G. Sun, Z. Zhou, G. Li, and W. Zhou, "Development of an optical fiber-guided robotic laser ultrasonic system for aeronautical composite structure testing," *Optik*, vol. 127, no. 12, pp. 5135–5140, 2016.
- [97] K. Nakahata, K. Ogi, K. Mizukami et al., "Three-dimensional imaging of subsurface delamination in carbon fiber reinforced plastic using photoacoustic wave method," *Electronics and Communications in Japan*, vol. 102, no. 5, pp. 35–42, 2019.
- [98] B. Kelkel, R. Sebastian, M. Gurka et al., "A new concept for the NDT of fiber-reinforced plastics via laser generated ultrasonic guided waves, 19th World Conference on NDT. Venue: Internationales Congress Center".
- [99] S. Wang, J. Echeverry, L. Trevisi, K. Prather, L. Xiang, and Y. Liu, "Ultrahigh resolution pulsed laser-induced photoacoustic detection of multi-scale damage in CFRP composites," *Applied Sciences*, vol. 10, no. 6, p. 2106, 2020.
- [100] B. Fischer, F. Sarasini, J. Tirillò et al., "Impact damage assessment in biocomposites by micro-CT and innovative air-coupled detection of laser-generated ultrasound," *Composite Structures*, vol. 210, pp. 922–931, 2019.
- [101] E. C. Aguado, C. Galleguillos, C. García, and F. L. Ramos, "Laser ultrasonics inspections of aeronautical components validated by computed tomography," in *Proceedings of 7th International Symposium on NDT in Aerospace*, Bremen, Germany, 2015.
- [102] H. Li, C. Zhang, H. L. Ji, and J. H. Qiu, "Damage identification technology of composite plate with curvature based on guided wave detection," *Foreign Electronic Measurement Technology*, vol. 38, no. 5, pp. 75–80, 2019.
- [103] J. H. Qiu, C. Zhang, H. L. Ji, and C. C. Tao, "NDT for aerospace composite structures using laser ultrasonic technique," *Aerospace Manufacturing Technology*, vol. 63, no. 19, pp. 14–23, 2020.
- [104] M. Dubois and T. E. Drake Jr., "Evolution of industrial laser-ultrasonic systems for the inspection of composites," *Nondestructive Testing and Evaluation*, vol. 26, no. 3–4, pp. 213–228, 2011.
- [105] L. Bustamante, N. Jeyaprakash, and C. H. Yang, "Hybrid laser and air-coupled ultrasonic defect detection of aluminium and CFRP plates by means of Lamb mode," *Results in Physics*, vol. 19, p. 103438, 2020.
- [106] L. Zeng, B. Wang, X. Liu et al., "High-resolution air-coupled laser ultrasound imaging of microstructure and defects in braided CFRP," *Composites Communications*, vol. 28, p. 100915, 2021.
- [107] K. Guangjie, Y. Zhengwei, J. Yong, Z. Wei, and D. Ying, "Detection on cracks in blades with complex profile based on ultrasonic infrared thermal imaging," *Infrared and Laser Engineering*, vol. 48, no. 12, article 1204002, 2019.
- [108] B. Yang, Y. Huang, and L. Cheng, "Defect detection and evaluation of ultrasonic infrared thermography for aerospace CFRP composites," *Infrared Physics & Technology*, vol. 60, pp. 166–173, 2013.
- [109] M. Z. Umar, V. P. Vavilov, H. Abdullah, and A. K. Ariffin, "Detecting low-energy impact damages in carbon-carbon composites by ultrasonic infrared thermography," *Russian Journal of Nondestructive Testing*, vol. 53, no. 7, pp. 530–538, 2017.
- [110] A. O. Chulkov, V. P. Vavilov, D. A. Nesteruk, A. M. Bedarev, S. Yarkimbaev, and B. I. Shagdyrov, "Synthesizing data of active infrared thermography under optical and ultrasonic stimulation of products made of complex-shaped CFRP," *Russian Journal of Nondestructive Testing*, vol. 56, no. 7, pp. 595–601, 2020.
- [111] T. B. Hudson, N. Auwajjan, and F. G. Yuan, "Guided wave-based system for real-time cure monitoring of composites using piezoelectric discs and phase-shifted fiber Bragg gratings," *Journal of Composite Materials*, vol. 53, no. 7, pp. 969–979, 2019.
- [112] R. Wang, Q. Wu, K. Xiong, and H. Q. Zhang, "Evaluation of composite matrix crack using nonlinear ultrasonic Lamb wave detected by fiber Bragg grating," *Aeronautical Manufacturing Technology*, vol. 64, no. 21, pp. 51–56, 2021.



## Research Article

# A Method Applied in Anomaly Detection of Impurities Adhering to Pipes of Coriolis Mass Flowmeter

Jianxin Ren <sup>1</sup>, Yixin Qin <sup>1</sup>, Peng Yang <sup>1</sup> and Peng Zhang<sup>2</sup>

<sup>1</sup>School of Automation, Northwestern Polytechnical University, Xi'an, China

<sup>2</sup>Xi'an Dongfeng Electrical Co., Ltd., Xi'an, China

Correspondence should be addressed to Jianxin Ren; renjianxin@nwpu.edu.cn

Received 24 September 2021; Revised 26 May 2022; Accepted 27 May 2022; Published 15 June 2022

Academic Editor: Akhilesh Pathak

Copyright © 2022 Jianxin Ren et al. This is an open access article distributed under the Creative Commons Attribution License, which permits unrestricted use, distribution, and reproduction in any medium, provided the original work is properly cited.

The Coriolis mass flowmeter (CMF) is widely used to measure mass flow, mainly in petrochemical, medical, pharmaceutical, food manufacturing, and other industries. The measuring tube is the crucial component of CMF, which affects the measurement accuracy and causes losses to the production of enterprises. Wall-mounted failure of the measuring tube affects measurement accuracy. A real-time detection method based on acceleration sensor array signal processing and pattern recognition are proposed to detect such failure. Two acceleration sensors are arranged outside the CMF to compose a five-channel sensor array. The signals of the multichannel array are decomposed through a blind source separation algorithm, and array signal features are extracted by a wavelet scattering network. Support vector data description (SVDD) is used to detect the hanging state of CMF at last. The experimental results show that the proposed method can be used to detect the CMF wall-mounted failure in real-time with an accuracy of 89.59%, and the method can reduce production losses.

## 1. Introduction

Coriolis mass flowmeter (CMF) is an instrument that can directly measure the mass flow of fluid without intermediate parameter conversion [1]. Compared with other traditional instruments for measuring mass flow, CMF has significant advantages such as high measurement accuracy, no moving parts, long service life, and slight wear. CMF has been widely used in fluid detection in petrochemical, food, medical, pharmaceutical, and other fields [2]. A typical CMF consists of measuring tubes, drive units, and sensors [3]. The quality of the impurities attached to the measuring tube greatly influences the measurement accuracy of the CMF. The higher the vibration frequency of the CMF, the greater the impact of the attached impurities on the measurement accuracy [4]. Due to long-term operation, the impurities in the fluid are deposited in the measuring tube leading to unbalance in the measuring tube. It affects the calibration factor of the flowmeter and the flow phase calculation of the CMF [5]. Vibration signal detection and analysis is a common method to detect the impurities in the CMF measuring

tube. X-ray and ultrasonic imaging technology are often used to inspect the interior of the CMF measuring tube. However, these methods are either expensive or need additional equipment on the measuring tube, making it difficult to meet the requirements of real-time detection of impurity adhesion of CMF measuring tube [6, 7]. Since the acceleration sensor can accurately detect the acceleration changes and convert them into usable output signals, it can be mounted on the CMF baffle to evaluate the quality of impurities attached to the CMF measuring tube without installing any equipment.

The signal collected from the CMF measuring tube by the acceleration sensor array is a large amount of data. The machine learning algorithm is a good data analysis and quality evaluation solution for such mass data problems. There are many methods for fault detection of CMF. Stark et al. proposed a multimode method to detect the fault state of CMF and completed the design of corresponding diagnostic equipment [8]. Yang et al. proposed an algorithm for CMF fault detection and correction based on threshold comparison [9]. This method improved the measurement accuracy

without increasing the system cost by adding corresponding algorithms to the existing software. Gao et al. realized feature recognition and correction of results by the neural networks [10]. Sun and Wang discussed and compared two verification methods of CMF: online verification and offline verification [11]. Wheeler et al. proposed a method to detect the faults of CMF through the change of its stiffness. However, this method can only be carried out when CMF is not working [12]. Array signal processing consists of array signal decomposition, signal feature extraction, and abnormal signal detection. Wang et al. proposed a bearing fault diagnosis method based on the combination of the fast independent component analysis (FastICA) in blind source separation and envelope spectrum analysis to identify the bearing fault signal characteristics under complex paths [13]. Multichannel data acquisition signals are mixed signals of the original signal. The FastICA preprocess them to obtain the source signal, which is a fast optimization iterative algorithm applicable to any type of data [14]. The effect of the machine learning detection algorithm depends on the extraction of signal features. There are many methods to extract signal features, such as empirical mode decomposition (EMD), Fourier transform, and wavelet transform [15]. EMD has problems with mode aliasing and endpoint effect, Fourier transform cannot be used for nonstationary signals, and wavelet transform has a wider range of applications to signals and retains time information [16–18]. An invariant scattering convolution network is a good feature extraction method based on wavelet transform. The one-class classification algorithm based on support vector data description (SVDD) is adopted in abnormal signal detection. The basic idea of the algorithm is to establish an optimal hypersphere for the data and then determine whether the sample is in the hypersphere for classification [19]. The array signal is decomposed by FastICA, and the original signal is obtained in this paper. The original signal's characteristics are extracted using the wavelet scattering network to train the SVDD anomaly detection model and realize outlier detection of the CMF.

This paper aims to present a CMF wall-mounted failure detection system without additional equipment on the measuring tube. The CMF measurement tube wall-mounted failure can be detected by analyzing the array signal. The principles and methodology are introduced in Section 2. Simulations and experiments are analyzed in Section 3. Some reasonable explanations of simulation results and experimental data are given in the last.

## 2. Principles and Methodology

**2.1. Working Principle of CMF.** CMF consists of a primary instrument and a secondary instrument, as shown in Figure 1(a). The primary instrument includes the flange, shunt body, measuring tube (U-shape), drive unit, and detection units, as shown in Figure 1(b). The secondary instrument is a transmitter that processes the output signal of the primary instrument.

The flange is used to connect the measuring tube and the secondary instrument. The shunt body is used to evenly

divide the measured liquid into two U-shape measuring tubes. An excitation signal is emitted by the drive unit as a mechanical force on the U-shape tube, and the measuring tube vibrates continuously in the second-order vibration mode. Sensors A and B are used to detect the phase changes of the tube.

When the fluid flows in the pipe, the measuring tube is twisted due to Coriolis force. This causes the phase of the feedback signals of the detection sensor A and B to be ahead and lag behind the phase of the driving signal, respectively. The phase relationship between sensors A and B is shown in Figure 2.

$A_0$  represents the amplitude of the vibration signal of the drive unit, and  $A_1$  and  $A_2$  represent the amplitude of sensors A and B, respectively. According to the phase difference between sensors A and B, the mass flow rate of the CMF at this moment can be obtained as shown in the following formula:

$$q_m = \frac{K_s}{8r^2} \Delta t. \quad (1)$$

$q_m$  is the mass flow rate,  $K_s$  is the angular elastic modulus of the measuring tube,  $r$  is the radius of the measuring tube, and  $\Delta t$  is the time difference between the two sides of the coil passing through the centerline.

**2.2. CMF Wall-Mounted Failure Detection Method and Design.** The sensors are divided into two groups. Array 1 consists of two external acceleration sensors distributed on the baffle plate in Figure 1(a); array 2 consists of the two sensors and drive unit as shown in Figure 1(a).

The specific anomaly detection progress is shown in Figure 3.

*Step 1.* After the array captures the vibration signal, the FastICA is used to decompose the signals of the two arrays to obtain the original signals.

*Step 2.* The wavelet scattering network is used to extract the features of the original signal, which is used to train the SVDD anomaly detection model.

*Step 3.* Finally, the single-classification algorithm based on SVDD is used to detect the CMF impurity adhesion. If the collected sensor array data is solved outside the hypersphere, it is believed that impurities are adhering to the pipe wall at this time.

*Step 1.* Fast independent component analysis.

The propagation path of waves in stainless steel is complex, and the propagation speed is fast. It is difficult to describe it with an accurate propagation model. In this paper, the simplified model is selected, and the linear hybrid FastICA is used to decompose the array signals. The FastICA aims to estimate the source signal  $S$  and the mixed matrix  $A$  by observing variable  $X$ .

There are three independent sound sources in Figure 4. A single microphone receives the mixed signals of the three

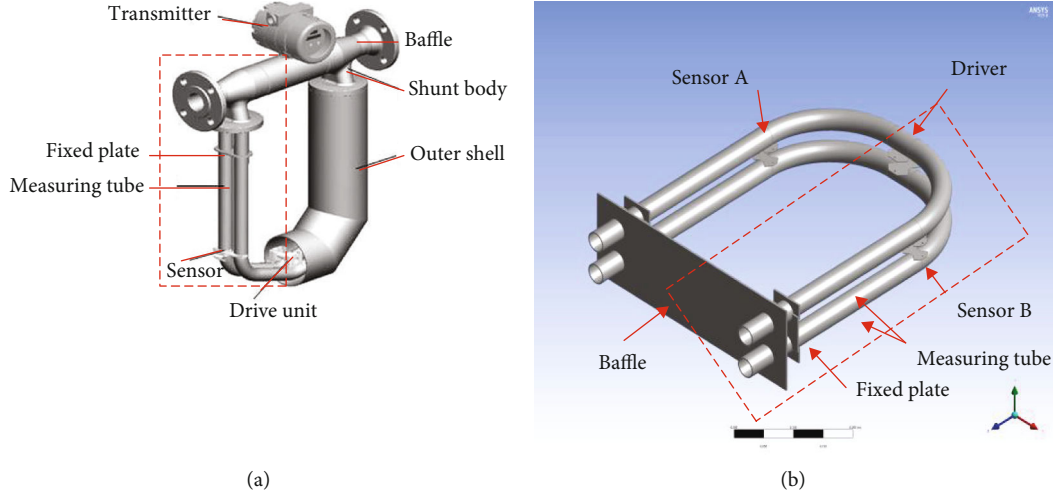


FIGURE 1: (a) The structure of CMF. (b) The primary instrument of CMF.

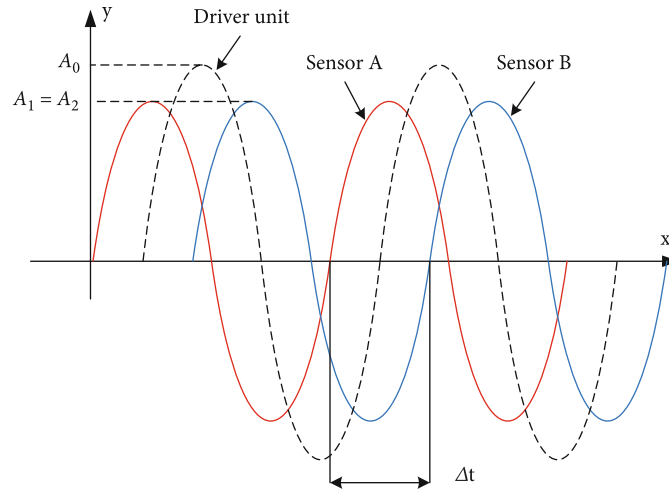


FIGURE 2: Drive unit, sensor A and B output signals.

sound sources. Due to the different distances between the sound source and each microphone, the wave signals received by each microphone are different.

There are  $n$  signal sources  $(s_1, s_2, \dots, s_n)$ ,  $S$  is an independent signal source, and  $A$  is an unknown mixed matrix, which is used to combine and construct observation variable  $X$ , which can be expressed as

$$X = AS. \quad (2)$$

Through the sensor array, the variables  $X$  can be obtained. According to the central limit theorem, the distribution of the combination of multiple random variables tends to Gaussian distribution. Finding an optimal direction  $W$  maximizes the non-Gaussian property of  $S$  in this direction. Thus,  $\hat{S} = W^T X$ , negative entropy is used to measure non-Gaussianness:

$$J(s) = H(s_{\text{gauss}}) - H(s). \quad (3)$$

$H(*)$  is differential entropy, and  $s_{\text{gauss}}$  is a Gaussian random variable with the same covariance matrix as  $s$ . In a sense, negative entropy is the optimal estimation of non-Gaussian. Negative entropy is usually solved by the approximate method of negative entropy. One of the classical methods is the following equation [20]:

$$J(s) = [E\{G(s)\} - E\{G(v)\}]^2. \quad (4)$$

Type of  $G(*)$  is a nonlinear function, and  $v$  is the standard normal distribution of random variables  $E\{G(v)\}$  will be a constant. We only need to care about the value of  $E\{G(W^T X)\}$ . According to the Karush-Kuhn-Tucker condition, the optimal solution of equation (4) under the condition of  $E\{(W^T X)^2\} = \|W\|_2 = 1$  can be expressed as the following equation:

$$\frac{\partial (J(s) - \beta(\|W\|^2 - 1))}{\partial W} = E\{XG'(W^T X)\} - \beta W = 0. \quad (5)$$

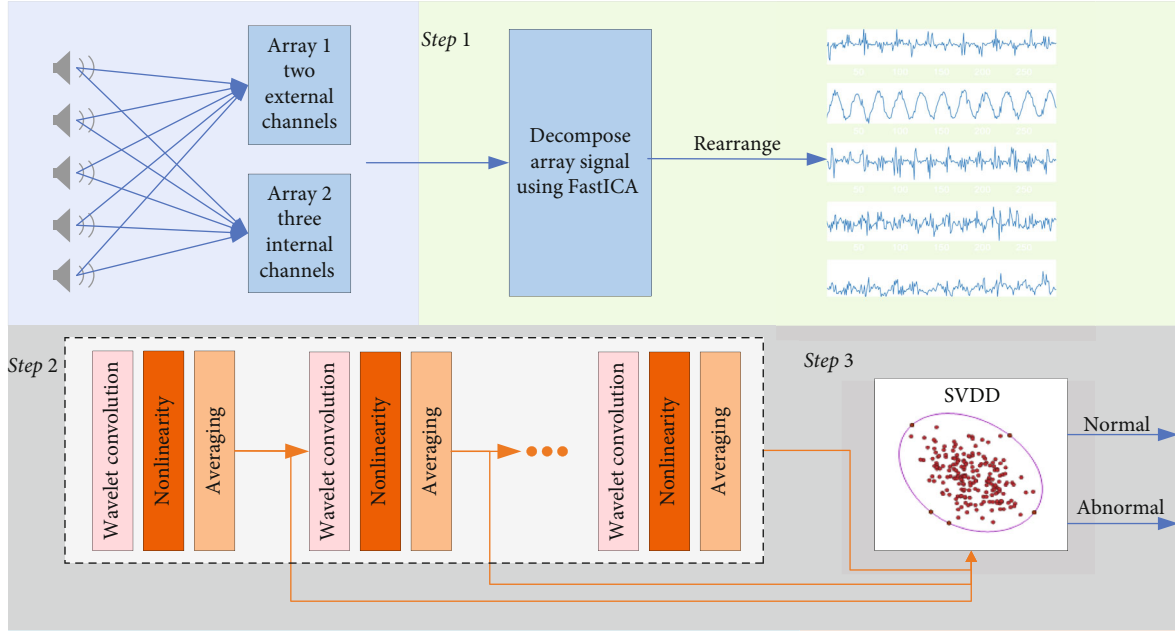


FIGURE 3: Anomaly detection progress.

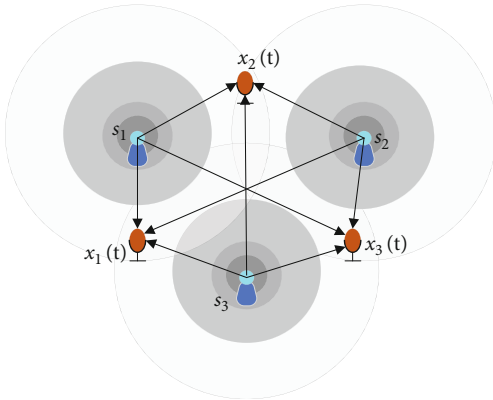


FIGURE 4: Blind source separation model.

The coefficient  $\beta$  is the Lagrange multiplier, and it is used to constrain the expectation of  $E\{XG'(W^T X)\}$ . Equation (5) can be expressed as follows:

$$W_{n+1} = W_n - \frac{E\{XG'(W_n^T X)\} + \beta W_n}{E\{XX^T G''(W_n^T X)\} + \beta}. \quad (6)$$

Under the condition of  $E\{XX^T\} = I$ , simplify equation (6), equation (7) is obtained.

$$W_{n+1} = E\{XG'(W_n^T X)\} - E\{G''(W_n^T X)\} W_n. \quad (7)$$

In this experiment, there is no requirement for amplitude, and the normalized processing of the obtained results

can be obtained as follows:

$$W_{n+1} = \frac{W_{n+1}}{|W_{n+1}|}. \quad (8)$$

$W$  is initialized as the identity matrix. Due to the uncertainty of the order of decomposition results of the FastICA, kurtosis is used as the sorting criterion to reorder the decomposed  $S$  to ensure that the array signal decomposition results are composed in a certain order and avoid the influence of order-disorder on feature extraction [21].

*Step 2. Wavelet transform.*

Various methods are used to generate signal features, such as the calculation of signal statistical characteristics and frequency-domain features [22]. The invariant scattering convolution network is used to automatically extract signal features with excellent performance and high interpretability. It contains wavelet convolution, nonlinear, and averaging operations [23, 24].

The complex wavelet transform for signal  $x$  is expressed as

$$x * \psi_{\lambda_1}(t) = x * \psi_{\lambda_1}^a(t) + jx * \psi_{\lambda_2}^b(t). \quad (9)$$

The extended wavelet  $\psi_{a,b}(t)$  is obtained by the main wavelet  $\psi(t)$  transform. The wavelet modulus coefficient is constructed by a complex wavelet and can be expressed as

$$U[\lambda]x = |x(t) * \psi_{\lambda}| = \sqrt{|x * \psi_{\lambda_1}^a(t)|^2 + |x * \psi_{\lambda_2}^b(t)|^2}. \quad (10)$$

The wavelet scattering coefficients with translation invariance can be obtained by convolving the modulus of

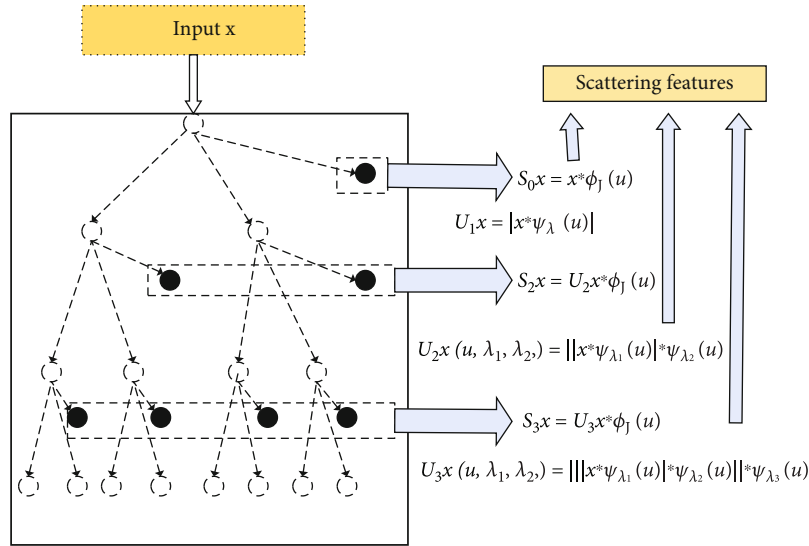


FIGURE 5: Invariant scattering convolution network.

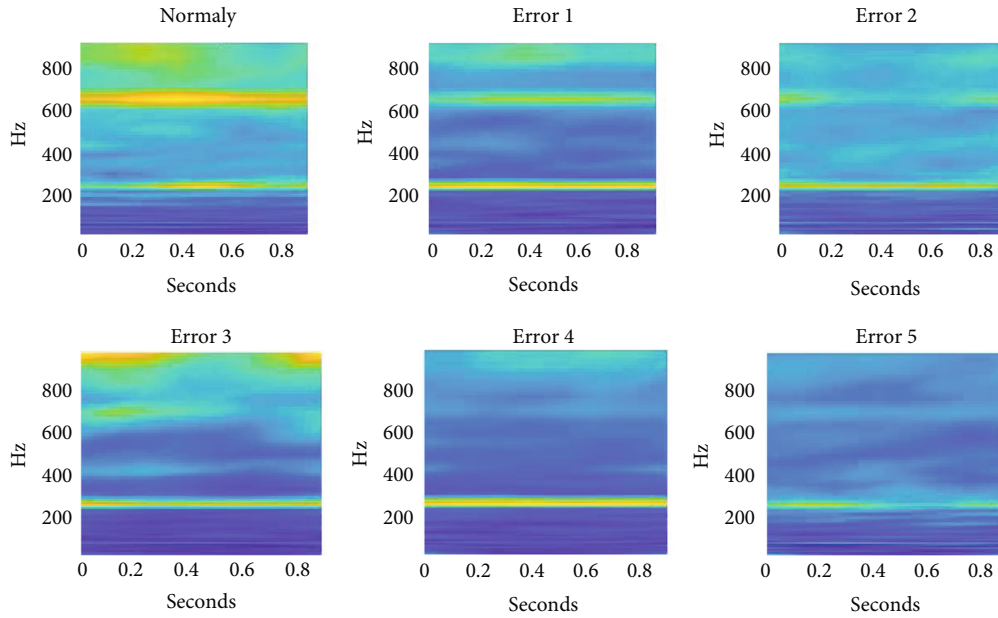


FIGURE 6: Wavelet scattering coefficient.

wavelet coefficients with the scaling coefficient function to obtain the low-frequency information of the signals:

$$[\lambda]x = |x(t) * \psi_\lambda| * \phi(t). \quad (11)$$

$\phi(t)$  is the scaling coefficient function of the low-pass filter.

The invariant scattering convolution network is shown in Figure 5. First, the signal is averaged using a wavelet low-pass filter, which loses the high-frequency details. A continuous wavelet transform is then applied to the signal to generate a set of diagrams of scale coefficients used to capture the details lost in the first step. After taking the modulus of scaling coefficients, the output is filtered using a wavelet low-pass filter to generate the first layer of scattering coeffi-

icients. In the end, repeat the process mentioned above to construct more layers of scattering coefficients.

Figure 6 shows the result of the signal of the two-channel accelerometer sensors after processing by FastICA placed on the fixed plate. For the six cases in the experiment, the scattering coefficients of the first decomposed component are very similar. Figure 6 shows the visualization of set 1 of the scattering coefficient filter for the second decomposed component. It can be seen from Figure 6 that there are significant differences in scattering characteristics between those with and without impurities adhered to the pipe wall.

An invariant scattering convolution network is a special kind of convolutional network. As the preset wavelet basis and nonlinear operators are set in advance, there is no need to adjust filter parameters through training samples, which



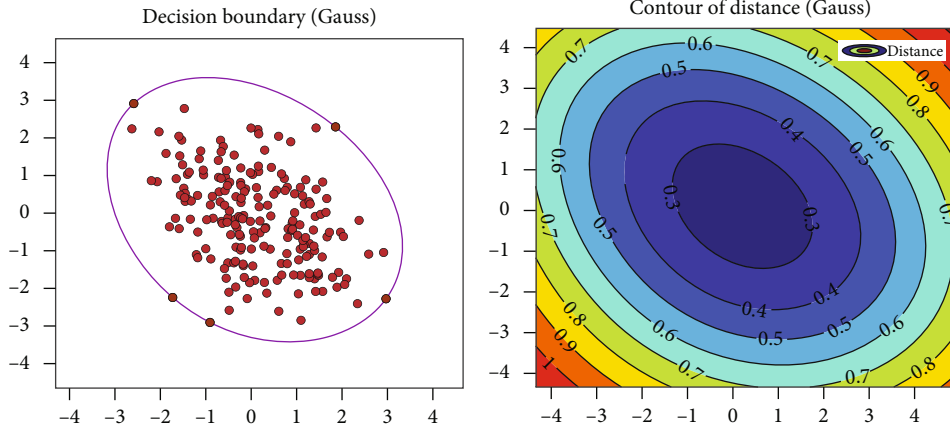


FIGURE 7: SVDD anomaly detection hypersphere.

greatly reduces the number of operations and computational complexity [25].

*Step 3.* Support vector data description.

In this paper, an attempt was made to hang impurities on the fixed points of the pipe wall to simulate the adhesion of impurities in the pipelines of CMF. Usually, the model can only be trained using data from the normal working state of CMF lacking counterexample data [26, 27]. This paper adopts a single classification algorithm based on SVDD to achieve the anomaly detection of impurity adhesion cases to solve this problem of extreme class imbalance [28, 29].

Tax and Tuin first proposed SVDD based on a support vector machine (SVM). This data description can be used for novelty or outlier detection. The primary detection principles are as follows.

Try to find a hypersphere with the smallest volume and wrap all the positive sample data in the hypersphere to complete the description of the target data region. Assuming that there is a class of positive sample data  $x \in R^{n*d}$ , where  $n$  is the number of samples and  $d$  is the feature dimension. The SVDD is used to find a hypersphere with the smallest volume which contains the positive class sample data, the center of the hypersphere is  $a$ , and the radius is  $R$ , which is transformed into the optimization problem:

$$\min R^2 + C \sum_{i=1}^n \xi_i, \quad (12)$$

$$\text{s.t. } \|x_i - a\|^2 \leq R^2 + \xi_i, \xi_i \geq 0. \quad (13)$$

In equations (12) and (13),  $\xi$  is the slack variable, and  $C$  is the penalty coefficient. The introduction of slack variables allows some of the samples not to be in the hypersphere, which reduces the volume of the hypersphere and reduces the risk of overfitting.

As shown in Figure 7, if the image of the new sample point falls into the optimal hypersphere in the feature space, the sample is regarded as a normal point. Conversely, if the

image of the new sample falls outside the optimal hypersphere in the feature space, the new sample is regarded as an outlier. In this way, the judgment of novelty or outlier detection is completed.

### 3. Simulations and Experiments

*3.1. Modelling and Analysis.* To carry out the research work and make the protocol feasible, the ANSYS simulation modelling shown in Figure 8(a) was completed to obtain the flow velocity distribution of the fluid within the CMF. According to the flow velocity distribution, the location of the CMF measuring tube that is most prone to wall-mounted failure is identified. The flow velocity of the measuring tube bend part of CMF is the greatest. When the flow body is viscous or contains impurities and flows through the bend pipe, it is not easy to appear viscous fluid or impurities deposition. At the location where the straight pipe intersects with the bend, the flow velocity of the fluid is the smallest, the probability of impurities hanging on the wall is the largest, and deposition is likely to occur.

Because the actual situation of the measuring tube impurity adhesion is complicated, the impurity adhesion's position and quality are difficult to accurately describe by the model, so this paper adopts a fixed-point wall-mounted study. Assuming that the density of impurities is greater than the density of the measured fluid, the location where the straight pipe intersects the bent pipe is taken as the location of impurity deposition. Blu-Tack is used to represent the impurities coated on the wall of the pipe to simulate the situation of impurities deposited and adhered in the measuring tube.

The Blu-Tack is pressed into a thin sheet and pasted on the pipe wall at the Figure 8(b) mark to simulate impurity deposition and adhesion to the pipe. The mass of plasticine pasted in a single position is 3 grams. There are a total of six conditions, respectively: (1) no impurity adhesion; (2) there is only one impurity adhesion; (3) there are two impurity adhesions on a measuring tube; (4) there is an impurity adhesion on each of the two measuring tubes; (5) there is one impurity adhesion on one measuring tube and two

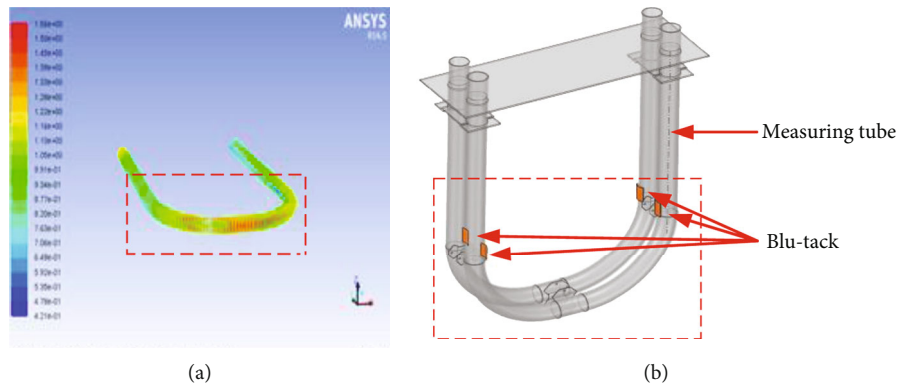


FIGURE 8: (a) CMF velocity simulation. (b) Experimental model of the CMF.

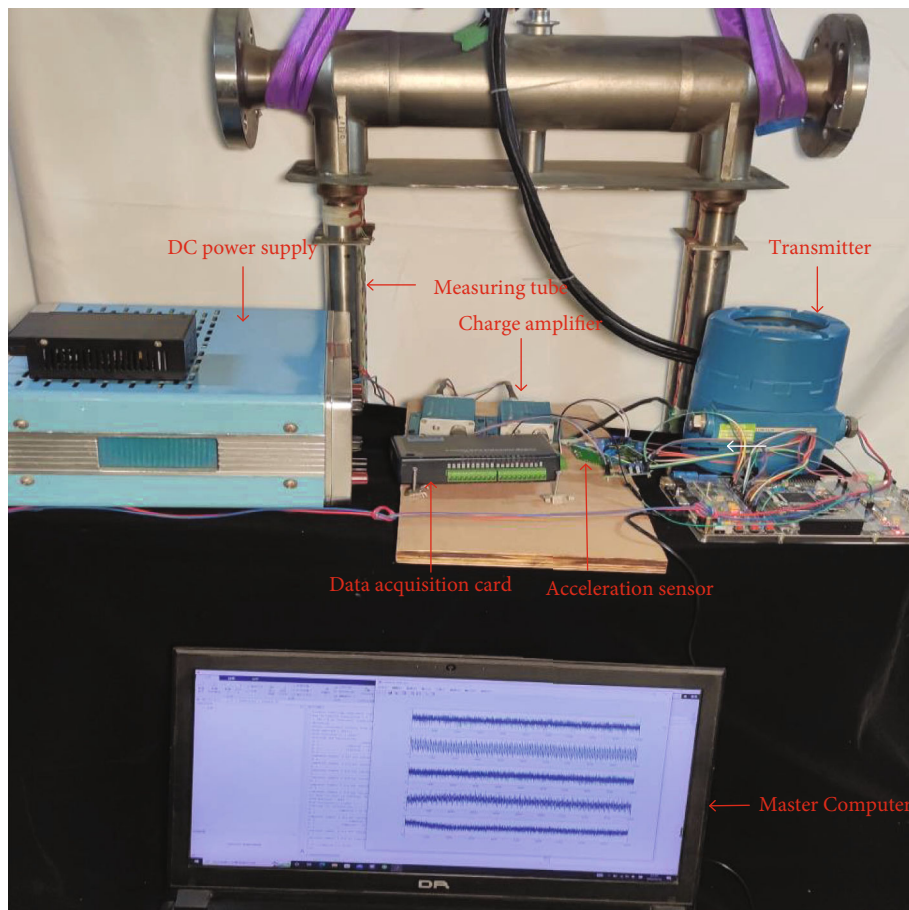


FIGURE 9: Experimental site device diagram.

impurities adhesion on the other measuring tube; (6) there are two impurity adhesions on both measuring tubes.

**3.2. Experimental Platform and Setups.** In this experiment, the required equipment includes N50 double U-shaped CMF and N50 double U-shaped CMF sensor matching DPT100 transmitter, Blu-Tack (used to simulate impurities), resolution of 0.01 electronic balance (weighing Blu-Tack), acceleration sensor of LC0403 vibration sensor, BVM-8101 microcharge amplifier, DC voltage regulator power supply,

data acquisition card USB-4716, and a master computer. The on-site device is shown in Figure 9.

A total of 30,000 sets of data were collected in this paper, including 20,000 sets of CMF normal operation data and 2000 sets of data of five wall-mounted experimental arrays, each with a length of 1 second. The contamination parameter is set to 0.1, indicating the proportion of contaminated data in the positive sample data set.

In the experiment, the sensor data of CMF under normal working conditions are collected first. Then, the FastICA is

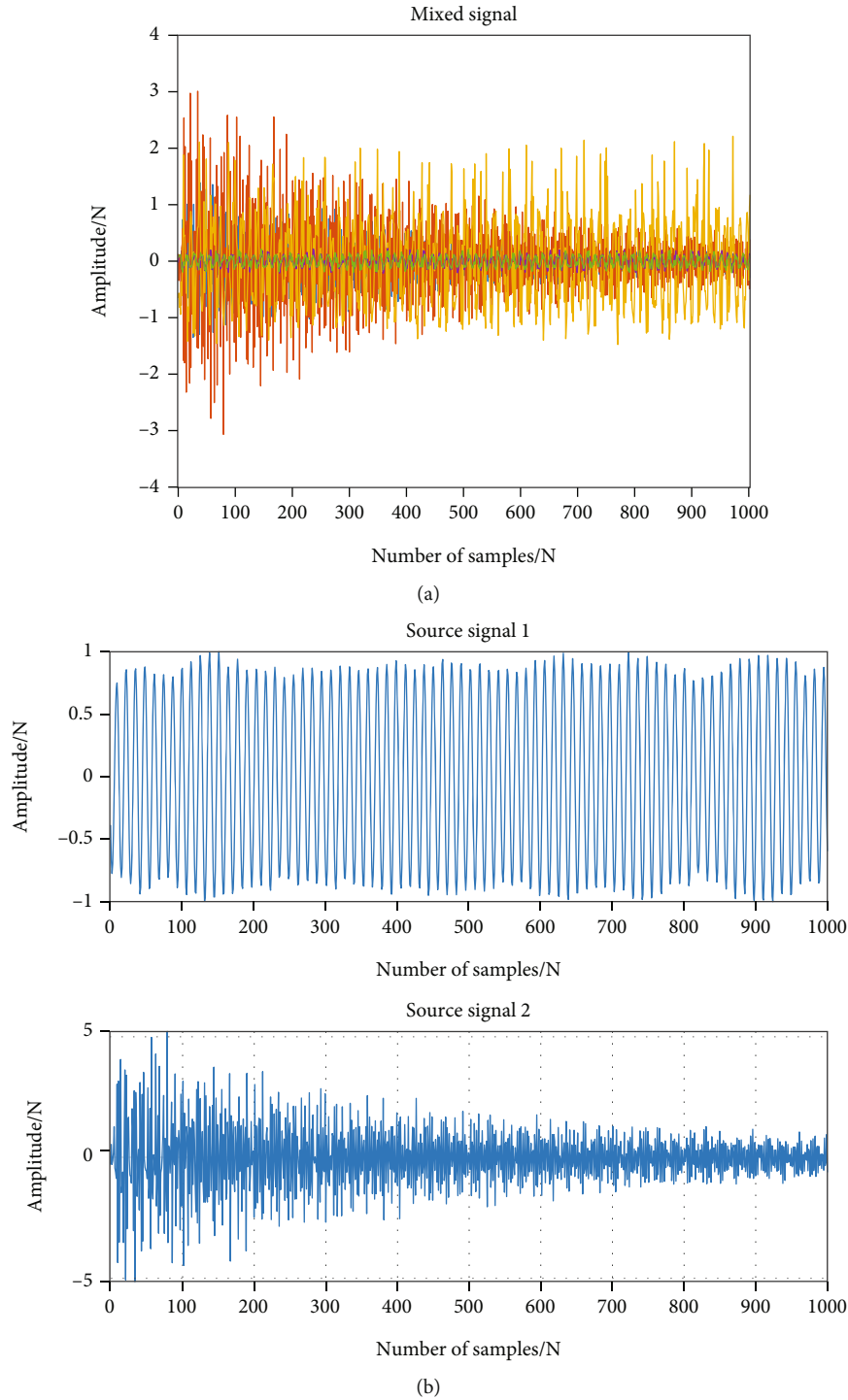


FIGURE 10: (a) Vibration signal of CMF. (b) FastICA decomposition results.

used to decompose the signal array, and the wavelet scattering features are extracted and selected. Finally, the detection model of SVDD is trained to obtain the spherical center and the decision boundary. If the collected sensor array data is outside the hypersphere after calculation, it can be considered that impurities are adhering to the pipe wall in CMF at this moment. On the contrary, it is considered that no impurities are adhering to the pipe wall in CMF at this

moment. Reasonable explanations of simulation results and experimental data are given at the end.

**3.3. Percussion Experiment of CMF.** The validity of the theory requires specific experiments to verify. Therefore, this percussion experiment is used to verify the effectiveness of the FastICA algorithm in CMF array signal decomposition. When CMF is in a normal working state, a slight percussion

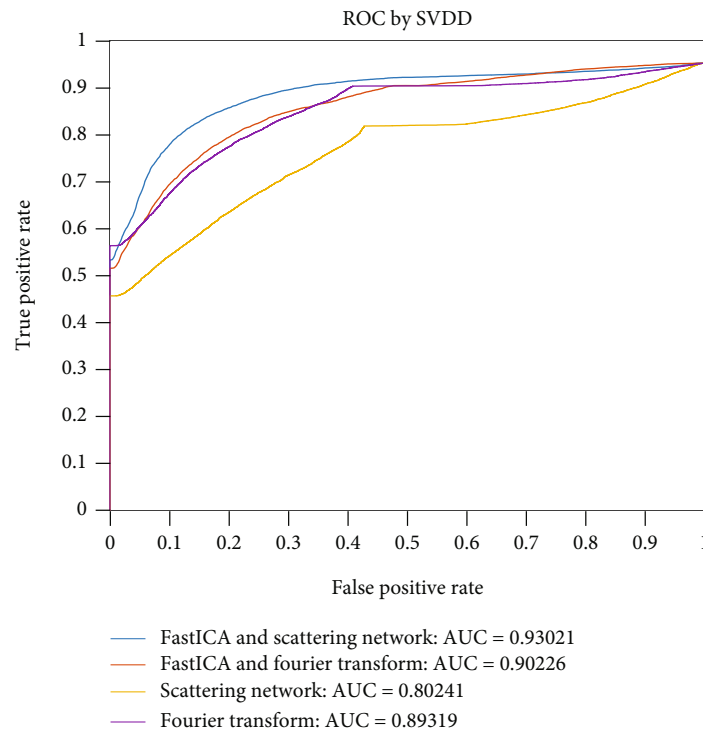


FIGURE 11: ROC curve of CMF fault detection.

TABLE 1: Confusion matrix.

	Predicted normally	Predicted anomaly
Actual normally	18000	2000
Actual anomaly	1124	8876

is given to the measuring tube, and the vibration signal of CMF is collected through the vibration data acquisition experimental platform.

The array signal of CMF is shown in Figure 10, where the  $x$ -axis is the number of sampling points while the  $y$ -axis is the amplitude. The CMF vibration signal waveform plot is shown in Figure 10(a), and the components obtained by FastICA decomposition are as shown in Figure 10(b). It can be concluded that source signal 1 is the signal transmitted to the outer shell by the vibration of the measuring tube during the normal operation of the CMF. Source signal 2 is the percussion signal to the measuring tube. The FastICA algorithm can effectively separate the mixed signals of CMF array signals through the analysis of experimental results.

**3.4. Results and Discussion.** The invariant convolution scattering networks and Fourier transform are used to extract features of the signal. Only the normal working data of CMF are used to train the anomaly detection model proposed in this paper. It can be divided into four cases according to whether to use the FastICA algorithm to decompose the array signal and whether to use the invariant convolutional scattering network or the Fourier transform to extract

the signal features. The receiver operating characteristic (ROC) curve is shown in Figure 11.

From the ROC curve, the FastICA algorithm to decompose the signal can improve the performance of the anomaly detection algorithm. The area under curve (AUC) metric significantly improved from 0.89319 to 0.93021 in the case of decomposing the signal by using the FastICA algorithm and extracting features by using an invariant convolutional scattering network. In this paper, the signal features extracted using the invariant convolutional scattering network are more efficient than the Fourier transform.

For the experiments, the array signal was processed using the anomaly detection algorithm in Figure 3, and the confusion matrix is shown in Table 1.

Even if few impurities adhere to the tube wall, the method could still be effectively monitored, and decent results can be achieved. Although the difference of the small additional mass reflected in the signal is very weak, the method proposed in this paper can reach the detection accuracy of 89.59%.

## 4. Conclusions

In this paper, the finite element analysis model of CMF is established based on the ANSYS Workbench platform, and a CMF wall-hanging fault detection algorithm based on an array sensor is proposed. 5 g plasticine is used to simulate impurities for experiments. Some conclusions can be derived according to the series of simulations and practical experiments.

- (1) *Fault Location Prediction*. The location most prone to wall-mounted failure is obtained by simulation, which is regarded as the location of the wall-mounted failure to establish the model
- (2) *Fault Detection Algorithm*. The wall-hanging fault detection algorithm of CMF based on an array sensor is proposed, and 5 g plasticine is used to simulate impurities for experiments. Finally, the accuracy of experimental results can reach 89.59%
- (3) *Application Advantages*. The algorithm proposed in this paper can detect whether there are impurities attached to the CMF wall in real-time. The detection effect is good, which further ensures the long-term efficient operation of CMF and reduces the cost of enterprises. At the same time, this method can be widely used in ultrasonic array detection signal processing, pattern recognition, anomaly detection, and data classification

## Data Availability

The data used to support the findings of this study are available from the corresponding author upon request.

## Conflicts of Interest

The authors declare that they have no conflicts of interest.

## Acknowledgments

This work was supported in part by the Key R & D Program of Shaanxi Province under Grant D5140190030 and in part by the National Natural Science Foundation of China under Grant 51875477.

## References

- [1] P. Zhang, M. C. Kang, and B. Wang, "The influencing factors on the vibrating tubes abrasion of Coriolis mass flowmeter," *Industrial instrumentation and automation equipment*, vol. 3, pp. 91–94, 2011.
- [2] J. X. Ren, Q. Sun, and P. Zhang, "Research on measurement technique of fluid viscosity and realization with ZLJC mass flowmeter," *Instrument Technique and Sensor*, vol. 10, pp. 31–34, 2013.
- [3] K. J. Xu, *Flow Sensor Signal Modeling, Processing and Implementation*, Science Press, 2011.
- [4] S. Q. Cao, H. T. Zhang, and Y. Q. Tu, "On-line detection method based on resonant frequency for dirt in U-shaped tube Coriolis mass flowmeter," *Instrument Technique Sensor*, vol. 6, pp. 30–33, 2017.
- [5] Y. T. Gao, M. Zhang, and J. X. Ren, "Analysis of Coriolis mass flowmeter life based on ANSYS," *Mechatronics*, vol. 20, no. 2, pp. 42–81, 2014.
- [6] C. Tan, X. Li, H. Liu, F. Dong, and F. Dong, "An ultrasonic transmission/reflection tomography system for industrial multiphase flow imaging," *IEEE Transactions on Industrial Electronics*, vol. 66, no. 12, pp. 9539–9548, 2019.
- [7] U. Ewert, "Current Trends in Digital Industrial Radiography - from Nano to Macro Scale," *2017 Far East NDT New Technology & Application Forum (FENDT)*, pp. 312–317, 2017.
- [8] C. P. Stark, A. T. Patten, M. A. Butler, and G. R. Duffel, *Diagnostic Equipment and Method for Coriolis Flowmeter*, CN101334305, USA, 2008.
- [9] J. Yang, M. Chen, and L. X. Zhang, "Fault detection and correction algorithm of section mass flowmeter," *Sensors and Microsystems*, vol. 23, no. 2, pp. 56–58, 2004.
- [10] Y. P. Gao, J. Yang, and M. Chen, "Study on fault detection and correction of Coriolis mass flowmeter," *Sensors and Microsystems*, 2005.
- [11] C. Sun and X. Q. Wang, "On-line and off-line verification of mass flowmeter," *Northwestern Industrial metrology*, vol. 17, no. 4, pp. 27–30, 2004.
- [12] M. G. Wheeler, D. F. Knowlman, M. J. Bell, and M. T. Crisfield, *Diagnostic Device and Method for Coriolis Flowmeter*, CN1860350, USA, 2006.
- [13] L. W. Wang, X. C. Luan, Y. D. Shua, and L. Yuan, "Fault extraction of roller bearing outer ring scratch in the complex path based on fast ICA," *Machinery Design and Manufacture*, vol. 12, pp. 77–81+87, 2021.
- [14] A. Hyvärinen, E. Oja, and E. Oja, "Independent component analysis: algorithms and applications," *Neural Networks*, vol. 13, no. 4–5, pp. 411–430, 2000.
- [15] Y. Yuan, W. Jiawen, Z. Desheng, W. Jiachen, W. Tonghai, and Y. Kehu, "Feature extraction and classification method of coal gangue acoustic signal during top coal caving," *Journal of Mining Science and Technology*, vol. 6, no. 6, pp. 711–720, 2021.
- [16] Y. Hu, X. T. Yuan, L. Y. Chen, Z. H. Jiang, and W. Liu, "GNSS-IR sea surface height inversion model based on wavelet transform and improved burg algorithm," *Geodesy and geodynamics*, vol. 42, no. 1, pp. 21–24+53, 2022.
- [17] T. Wang, M. C. Zhang, Q. H. Yu, and H. Y. Zhang, "Comparing the applications of EMD and EEMD on time-frequency analysis of the seismic signal," *IEEE Journal of Selected Topics in Applied Earth Observations and Remote Sensing*, p. 99, 2021.
- [18] M. Sifuzzaman, "Application of wavelet transform and its advantages compared to Fourier transform," *Journal of Physical Sciences*, 2009.
- [19] J. Xu, J. Yao, and L. Ni, "Fault detection based on SVDD and cluster algorithm," in *2011 International Conference on Electronics*, *2011 International Conference on Electronics, Communications and Control (ICECC)*, pp. 2050–2052, Ningbo, China, 2011.
- [20] C. Ji, Y. Yu, and P. Yu, "A new FastICA algorithm of Newton's iteration," in *2010 2nd International Conference on Education Technology and Computer*, p. V3-481, Shanghai, 2010.
- [21] M. Bressan, D. Guillet, and J. Vitria, "Using an ICA representation of high dimensional data for object recognition and classification," in *Proceedings of the 2001 IEEE computer society conference on computer vision and pattern recognition*, pp. I-1, Kauai, HI, USA, 2001.
- [22] A. Hyvärinen and E. Oja, "A fast fixed-point algorithm for independent component analysis," *Neural Computation*, vol. 9, no. 7, pp. 1483–1492, 1997.
- [23] J. Andén and S. Mallat, "Deep scattering spectrum," *IEEE Transactions on Signal Processing*, vol. 62, no. 16, pp. 4114–4128, 2014.
- [24] S. Mallat, "Understanding deep convolutional networks," *Philos Trans A Math Phys Eng*, vol. 374, p. 2065, 2016.



- [25] J. Bruna and S. Mallat, "Invariant scattering convolution networks," *IEEE Transactions on Pattern Analysis and Machine Intelligence*, vol. 35, no. 8, pp. 1872–1886, 2013.
- [26] F. Rashid and A. Miri, "User and event behavior analytics on differentially private data for anomaly detection," in *2021 7th IEEE Intl Conference on Big Data Security on Cloud (Big Data Security), IEEE Intl Conference on High Performance and Smart Computing (HPSC) and IEEE Intl Conference on Intelligent Data and Security (IDS)*, pp. 81–86, NY, USA, 2021.
- [27] S. Katsumata, D. Kanemoto, and M. Ohki, "Applying outlier detection and independent component analysis for compressed sensing EEG measurement framework," *Biomedical Circuits and Systems Conference (BioCAS)*, pp. 1–4, 2019.
- [28] D. M. J. Tax, R. P. W. Duin, and R. P. W. Duin, "Support vector domain description," *Pattern Recognition Letters*, vol. 20, no. 11-13, pp. 1191–1199, 1999.
- [29] M. Yao and H. Wang, "One-Class Support Vector Machine for Functional Data Novelty Detection," *2012Third Global Congress on Intelligent Systems*, pp. 172–175, 2012.

## Research Article

# Shape Reconstruction of Eccentric Defect in Cylindrical Component by Modified Born Approximation Method

Gangfeng Zheng <sup>1</sup>, Ze Li <sup>1</sup>, Songfeng Liu <sup>1</sup>, Hao Dong <sup>1</sup>, Bin Wu <sup>2</sup> and Cunfu He <sup>2</sup>

<sup>1</sup>School of Materials Science and Engineering, Anhui University of Science and Technology, Huainan 232001, China

<sup>2</sup>College of Mechanical Engineering and Applied Electronics Technology, Beijing University of Technology, Beijing 100022, China

Correspondence should be addressed to Gangfeng Zheng; 649811739@qq.com

Received 7 March 2022; Accepted 29 April 2022; Published 17 May 2022

Academic Editor: Nan Li

Copyright © 2022 Gangfeng Zheng et al. This is an open access article distributed under the Creative Commons Attribution License, which permits unrestricted use, distribution, and reproduction in any medium, provided the original work is properly cited.

In this paper, a cylindrical aluminum sample with an eccentric circular hole was prepared, and ultrasonic measurements were carried out by experimental means. The measurement area was limited to a plane edge perpendicular to the axis of the cylindrical component. The measured waveform data were input into the formula of approximate correction method, and the section image was obtained by using a modified Born approximation (MBA) method. Then, the three-dimensional (3D) shape of the defects in the aluminum sample was reconstructed by superimposing the cross-sectional images. Results showed that the defect reconstruction effect of the two-dimensional section and the 3D defect reconstruction effect were significantly improved by the MBA method.

## 1. Introduction

Nondestructive testing (NDT) and characterization of defects, such as cracks and voids, are important in many branches of industries [1–4]. Examples are the new types of bridges, grid structures, high-rise buildings, and aerospace crafts. The quality of the component directly affects the equipment performance and service life. Thus, NDT technology is continuously refined [5–9]. NDT of cylindrical components is essential. Cylindrical components have wide applications and considerable market potential. For several aperture geometries, exact inversion formulas can be derived under the assumption that scattering is sufficiently weak for Born approximation (BA) [10–13] to hold and that only backscattering is observed. The solution to this problem does not require far-field approximations. This condition is significant because the classical Born inversion procedure, which is perhaps the simplest and best-known embodiment of the inverse scattering problem, relies crucially on a far-field assumption.

Suitably dealing with the defect echo signal will greatly benefit the quantitative inversion of the defects of cylindrical components [14]. The task of deriving the structure of an object from scattered radiation is known as the inverse scattering problem. The inversion procedure acquires sufficient independent data to reconstruct the scattering parameter by varying the frequency and/or direction of illumination (or object orientation with respect to the source) while measuring the scattered waves over an aperture located beyond the scattering region [15]. If the measurements are performed on a far field with respect to the scattering region, and if the BA is applicable, then the scattering amplitude distribution and the measured time-domain data bear a simple Fourier transform relationship. However, the defect image is distorted when the defect inside the cylindrical component is inverted using the BA method. Therefore, based on the BA method for defect inversion, this paper proposes a quantitative inversion study of defects in cylindrical components using the backscatter echo amplitude correction method for the backscatter echo amplitudes corresponding to different integral wave numbers.

## 2. Modified Born Approximation (MBA) Method

### 2.1. Amplitude Correction Technique

**2.1.1. Acoustic Pressure of the Probe Emission Sound Field.** The application of the BA method is based on the condition that the incident wave is a plane wave. Therefore, as long as the vertical distance between the probe and defect is unchanged, the energy of the incident wave can be consistent, and the ideal result of defect reconstruction can be obtained. However, when the plane nonfocus probe is used to carry out the experimental research, the sound energy will attenuate with the propagation of sound waves in the measured medium due to the divergence of the sound beam emitted by the probe. At the same time, when the defect deviates from the center of the sound beam, its incident energy will change, affecting the amplitude of the backscattered echo signal (Figure 1). The acoustic pressure variation of the probe emission sound field  $p(\vec{r}, \omega)$  in space must therefore be studied to accurately correct the backscatter echo amplitude  $A_m$ . Here,  $r$  is the distance between the source and field points, and  $\omega$  is the angular frequency.

The probe crystal sheet is discretized into a series of point sources, and the response of the point sound source can be represented by Green's formula function, which can be substituted into the Helmholtz equation.

$$\nabla^2 G(r, \omega) + k^2 G(r, \omega) = -4\pi\delta(r), \quad (1)$$

where  $\delta(r)$  denotes the Dirac pulse function and  $k$  is the wave number. In accordance with the Kirchhoff boundary integral equation, only the sound field of the point source is required, and the scattered sound field produced by any sound source can be written as follows:

$$p(\vec{r}, \omega) = \iint_S \left[ G(\vec{r}, \omega) \frac{\partial p_0}{\partial n} - p_0 \frac{\partial G(\vec{r}, \omega)}{\partial n} \right] dS, \quad (2)$$

where  $r$  denotes the distance between the source and field points,  $dS$  denotes the discrete elements of the transducer surface, and  $n$  is the normal vector of the transducer surface.  $p_0$  denotes the acoustic pressure on the transducer surface. Green's formula for the sound source at the point in free space can be expressed as follows:

$$G(\vec{r}, \omega) = \frac{1}{4\pi} \frac{\exp(-ik_L r)}{r}, \quad (3)$$

where  $k_L$  is the longitudinal wave number and  $i$  is the imaginary unit,  $i^2 = -1$ .

$$p_0 = \rho c_L v_n, \quad (4)$$

where  $v_n = e^{ikr}$  is the surface vibration velocity of the probe crystal sheet,  $c_L$  is the longitudinal velocity, and  $\rho$  is the medium density.

On the boundary, the partial derivative of the sound pressure is calculated in the normal direction:

$$\frac{\partial p_0}{\partial n} = \rho c_L (i k e^{ikr}) \cos(r, n) = i \omega \rho v_n \cos(r, n). \quad (5)$$

Given that the surface vibration direction and normal angle of the probe crystal sheet are zero,  $\cos(r, n) = 1$ :

$$\begin{aligned} \frac{\partial p_0}{\partial n} &= i \omega \rho v_n, \\ \frac{\partial G(\vec{r}, \omega)}{\partial n} &= \left[ \frac{-ik_L \exp(-ik_L \vec{r})}{\vec{r}} - \frac{\exp(-ik_L \vec{r})}{\vec{r}^2} \right] \cos(r, n). \end{aligned} \quad (6)$$

In the remote area,  $r > \lambda$ , the normal derivative of Green's function can be approximated as follows:

$$\begin{aligned} \frac{\partial G(\vec{r}, \omega)}{\partial n} &= \frac{-ik_L \exp(-ik_L \vec{r})}{\vec{r}}, \\ p(\vec{r}, \omega) &= \iint_S \left[ G(\vec{r}, \omega) \frac{\partial p_0}{\partial n} - p_0 \frac{\partial G(\vec{r}, \omega)}{\partial n} \right] dS \\ &= \frac{1}{4\pi} \iint_S \left[ \frac{\exp(-ik_L \vec{r})}{\vec{r}} i \omega \rho v_n - \rho c_L v_n (-ik_L) \frac{\exp(-ik_L \vec{r})}{\vec{r}} \right] dS \\ &= \frac{1}{2\pi} \iint_S i \omega \rho v_n \frac{\exp(-ik_L \vec{r})}{\vec{r}} dS. \end{aligned} \quad (7)$$

**2.2. Amplitude Correction Method.** The ultrasonic used in the experiment has a certain bandwidth, and the calculation model  $p(\vec{r}, \omega)$  of sound field distribution is based on a single frequency. Therefore, the sound field distribution values at different frequencies in a series of bandwidth ranges must be calculated based on the probe bandwidth. By contrast, the reconstruction model should be used for integration. According to the backscattered echo amplitude  $A_m(k_L)$  corresponding to different integral wave numbers  $k_L$ , the correction coefficient composed of the sound field model  $p(\vec{r}, \omega)$  of the corresponding frequency is used to correct the amplitude.

The concrete implementation process assumes that the crossing time of the probe to the center of the measured component is  $t_0$  (which can be obtained by using the reference component measurement) and an eccentric circular hole defect exists in the measured component. As shown in Figure 2, when the probe is measured at position  $\theta_1$ , and the signal transit time is  $t_1 > t_0$ , the defect incident signal sound pressure value  $p_1(k_L)$  is less than the component center position sound pressure value  $p_0(k_L)$ ; that is,  $p_1(k_L) < p_0(k_L)$ . Given the weak incident energy, the amplitude  $A_m(k_L, \theta_1)$  of the backscatter echo measured is small. Thus, the ratio of the incident sound pressure  $p_1$  to the sound

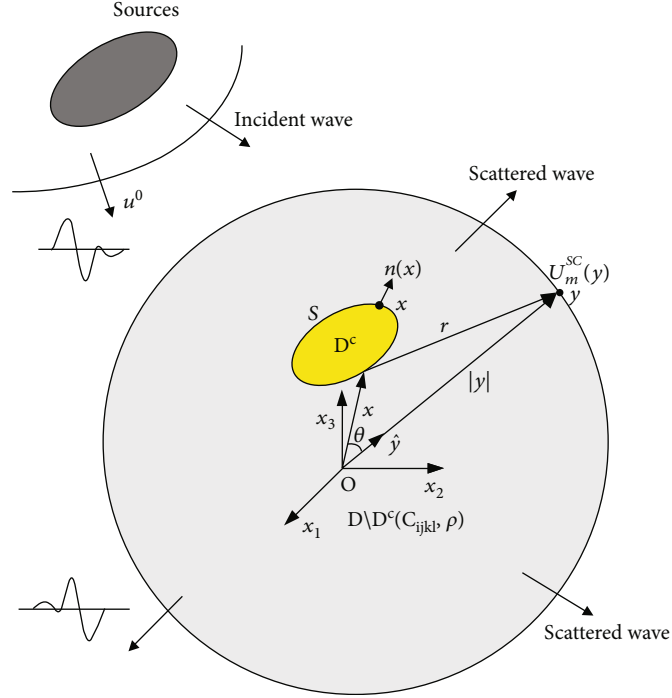


FIGURE 1: Incident waves scattered from a finite volume  $D^C$  in an infinite region.

pressure  $p_0$  at the center of the component should be used as the correction coefficient to correct the amplitude  $A_m(k_L, \theta_1)$  of the backscatter echo, as shown in

$$\tilde{A}_m(k_L, \theta_1) = \frac{A_m(k_L, \theta_1)}{(p_1(k_L)/p_0(k_L))} \dots \quad (8)$$

At different frequencies  $\omega$  (wave number  $k_L$ ), the resulting sound fields vary, and the corresponding  $p_0(k_L)$  is different from  $p_1(k_L)$ . Therefore, the sound field distribution map at different frequencies must be obtained by calculation, followed by the construction of the sound field matrix. In this way, thus, the position of the defect in the sound field can be assessed by time  $t$  of defect signal transition, and the sound pressure value  $p_n(k_L)$  (similar to the look-up table method) at different frequencies  $\omega$  (wave number  $k_L$ ) of the position can be obtained.

In the same way, as shown in Figure 3, when the probe is measured in position  $\theta_2$ , and the signal transit time is  $t_2 < t_0$ , the defect incident signal sound pressure value  $p_2$  is larger than the sound pressure value  $p_0$  of the central position of the component; that is,  $p_2 > p_0$ . The backscatter echo amplitude  $A_m(k_L, \theta_2)$  is also measured. Given that the incident energy is relatively strong, and  $A_m(k_L, \theta_2)$  is large, the ratio of the incident sound pressure  $p_2$  to the sound pressure  $p_0$  at the center position of the component must be used as

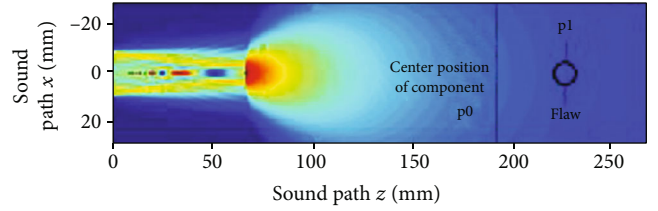


FIGURE 2: Relative position of probe and eccentric circular hole defect ( $t_1 > t_0$ ).

the correction coefficient to correct the amplitude of the backscattering echo  $A_m(k_L, \theta_2)$ , as shown in

$$\tilde{A}_m(k_L, \theta_2) = \frac{A_m(k_L, \theta_2)}{(p_2(k_L)/p_0(k_L))} \dots \quad (9)$$

**2.3. MBA Method.** The BA method is a low-frequency approximation method sensitive to bulk defects and insensitive to crack defects. Based on the BA method, the backscatter echo amplitude in the theoretical formula of the BA method is corrected. The corrected method is known as the MBA method.

The formula for reconstructing defects is given in [16] by BA methods.

$$\Gamma(x) = \frac{1}{(2\pi)^3} \int_0^{2\pi} \int_0^\pi \int_0^\infty \frac{\hat{y}_m}{2u^0 k_L^2} A_m(k_L, \theta, \varphi) e^{2ik_L(x_1 \sin \theta \cos \varphi + x_2 \sin \theta \sin \varphi + x_3 \cos \theta)} 8k_L^2 \sin \theta dk_L d\theta d\varphi. \quad (10)$$

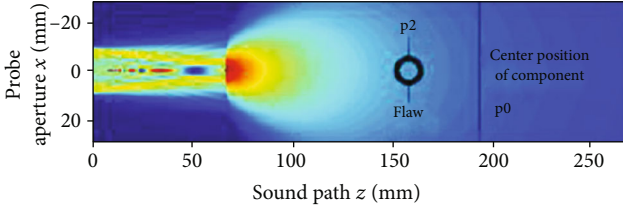


FIGURE 3: Relative position of the probe and eccentric circular hole defect ( $t_2 < t_0$ ).

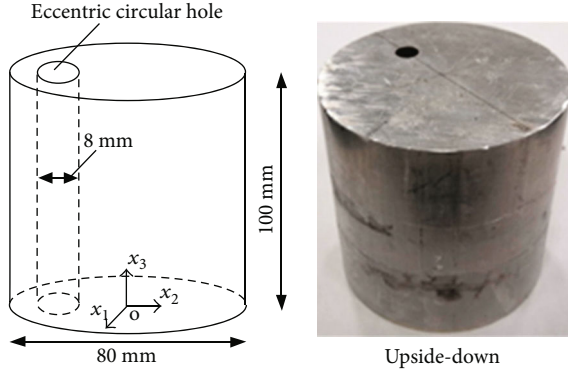


FIGURE 4: Cylindrical aluminum specimen with eccentric circular hole.



FIGURE 5: Ultrasonic testing equipment.

On this basis, the backscattering echo amplitude in the formula is corrected. After correction, the backscatte-

$$\tilde{\Gamma}(x) = \frac{1}{(2\pi)^3} \int_0^{2\pi} \int_0^{\pi} \int_0^{\infty} \frac{\hat{y}_m}{2u^0 k_L^2} \tilde{A}_m(k_L, \theta, \varphi) e^{2ik_L(x_1 \sin \theta \cos \varphi + x_2 \sin \theta \sin \varphi + x_3 \cos \theta)} 8k_L^2 \sin \theta dk_L d\theta d\varphi, \quad (11)$$

where

$$\tilde{A}_m(k_L, \theta) = \frac{A_m(k_L, \theta)}{(p(k_L)/p_0(k_L))}. \quad (12)$$

**2.4. Experimental Measurements.** An aluminum specimen with a diameter of 80 mm was prepared (Figure 4). The speci-

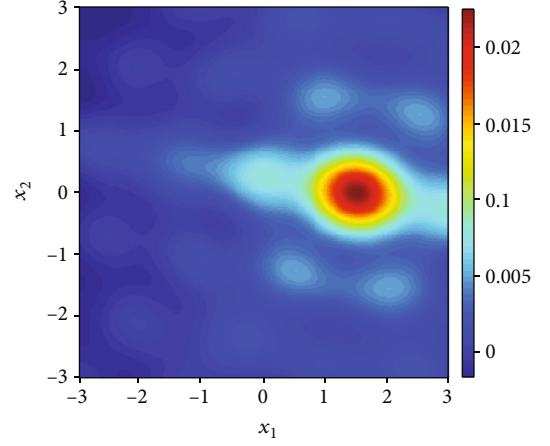


FIGURE 6: Reconstruction of two-dimensional (2D) section defect before amplitude correction.

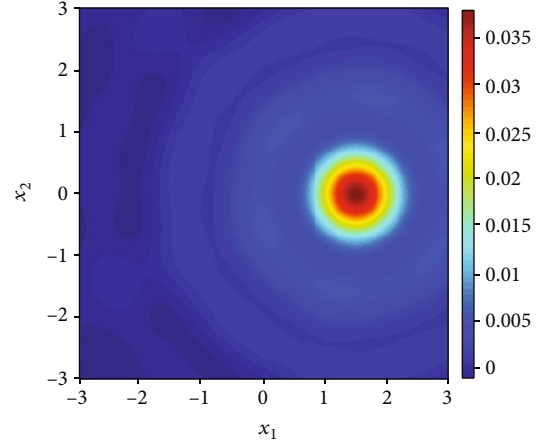


FIGURE 7: Reconstruction of 2D section defect after amplitude correction.

ring echo amplitude becomes  $\tilde{A}_m(k_L, \theta)$ . Thus, the theoretical formula about the MBA method is obtained as follows:

men includes a cylindrical eccentric circular hole (diameter: 8 mm) as a defect model. Figure 5 shows the experimental setup. The scattered wave from the defect model was measured by the longitudinal-longitudinal pulse-echo method. A contact type transducer with a diameter of 0.125 is moved to the surface of the specimen  $10^\circ$ , a step in the  $x_1$ - $x_2$  plane, and 10 mm, a step in the  $x_3$  direction from  $x_3 = 0$  mm to 100 mm.



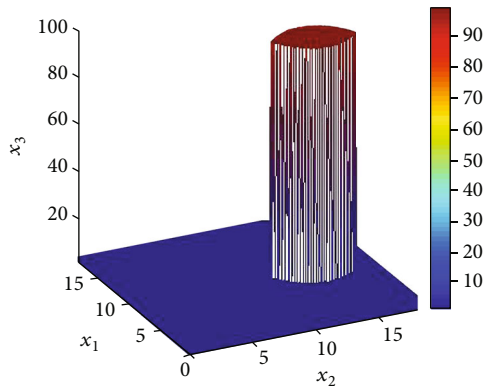


FIGURE 8: Reconstruction of three-dimensional (3D) defect before amplitude correction (unit: mm).

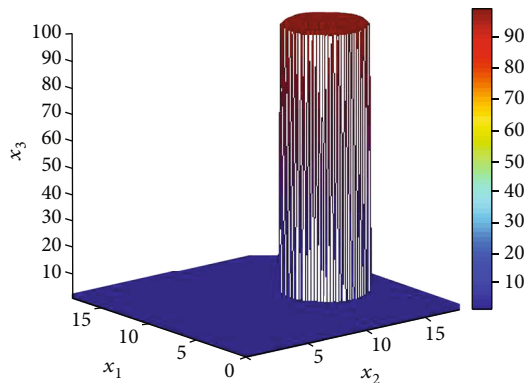


FIGURE 9: Reconstruction of 3D defect after amplitude correction (unit: mm).

An industrial-specific ultrasonic coupling agent was used as the couplant, resulting in good acoustic coupling and fixation of the transducer. The transducer was driven by a 300 V square wave pulser–receiver. A digital oscilloscope and PC were used for data processing and shape reconstruction. The center frequency of the transducer was 10 MHz, and frequencies ranging from 7.5 MHz to 12.5 MHz were used for defect inversion.

Figures 6 and 7 display the cross-sectional defect images obtained from  $\Gamma(x)$  and  $\bar{\Gamma}(x)$  for the eccentric circular hole, respectively. Given that we collected the data of the scattering amplitudes  $10^\circ$  a step on the surface of the specimen in the  $x_1$ – $x_2$  plane, each cross-sectional defect image was reconstructed by looping 36 times around a cross section. The type of data we processed is a Microsoft Office Excel Worksheet (.xlsx). Figures 6 and 7 show the results of shape reconstruction of BA and MBA, respectively. Total cross-sectional images were piled up, and 3D shape reconstruction was performed by introducing the interpolation for the piled-up cross-sectional images. Figures 8 and 9 reveal the results of 3D shape reconstructions of BA and MBA, respectively.

Figures 7 and 9 show the results after introducing the defect echo amplitude correction coefficient. After the defect amplitude correction, the reconstruction effects of 2D and 3D defects were significantly improved.

### 3. Conclusions

An MBA method for an eccentric defect in a cylindrical component was presented, and it can relate the backscattering signal distributed on the frequency domain to the geometrical information of defects. Therefore, shape reconstruction can be treated as an inverse problem. The ultrasonic field was calculated in a homogeneous and isotropic aluminum medium after its passage through a curved interface, which was used to correct the amplitude of pulse echoes. The reconstruction qualities before and after compensation were compared, and the results showed that the reconstruction effect can be improved effectively after compensation. We find the following:

- (1) The MBA method was proposed.
- (2) The shape of the eccentric void defect was reconstructed by the MBA method.
- (3) The results showed that the defect reconstruction effect of the 2D section and the 3D defect reconstruction effect were significantly improved by the MBA method.

### Data Availability

We confirm that the data supporting the findings of this study are available within the article [and/or] its supplementary materials. Supplementary material file shows the echo data of the first measurement point of the first cross section, and the data format of the other measurement points is the same as that of supplementary material file.

### Conflicts of Interest

We declare that there is no conflict of interest regarding the publication of this paper.

### Acknowledgments

This work was supported by the National Natural Science Foundation of China (Grant Nos. 51374015 and 10872001), the Key Scientific and Technological Research Project of the Ministry of Education (Grant No. 211076), and the Anhui Fund Project for Outstanding Youths (Grant No. 10040606Y26).

### Supplementary Materials

Supplementary material file shows the echo data of the first measurement point of the first cross section, and the data format of the other measurement points is the same as that of the supplementary material file. The supplementary material file corresponds to line 187 in the manuscript. (*Supplementary Materials*)

### References

- [1] X. F. Guan, J. J. He, and E. M. Rasselkorde, “A time-domain synthetic aperture ultrasound imaging method for material flaw quantification with validations on small-scale artificial and natural flaws,” *Ultrasonics*, vol. 56, pp. 487–496, 2015.

- [2] Q. I. Jinhao, T. A. Chongcong, J. I. Hongli, Z. H. Chao, and Z. H. Jinling, "Damage detection and material property reconstruction of composite laminates using laser ultrasonic technique," *Transactions of Nanjing University of Aeronautics and Astronautics*, vol. 36, no. 1, pp. 1–11, 2019.
- [3] V. F. Maria and F. Zheng, "Sizing of flaws using ultrasonic bulk wave testing: a review," *Ultrasonics*, vol. 88, pp. 26–42, 2018.
- [4] J. Rodríguez-Sendra, N. Jiménez, R. Picó, J. Faus, and F. Camarena, "Monitoring the setting of calcium sulfate bone-graft substitute using ultrasonic backscattering," *IEEE Transactions on Ultrasonics, Ferroelectrics, and Frequency Control*, vol. 66, no. 10, pp. 1658–1666, 2019.
- [5] A. Praveen, K. Vijayarekha, S. T. Abraham, and B. Venkatraman, "Signal quality enhancement using higher order wavelets for ultrasonic TOFD signals from austenitic stainless steel welds," *Ultrasonics*, vol. 53, no. 7, pp. 1288–1292, 2013.
- [6] A. Raza, W. Hassan, T. Ogay, I. Hwang, and S. Jeon, "Perceptually correct haptic rendering in mid-air using ultrasound phased array," *IEEE Transactions on Industrial Electronics*, vol. 67, no. 1, pp. 736–745, 2020.
- [7] H. Abrial, V. Lawrensius, D. Handayani, and E. Sugiarti, "Preparation of nano-sized particles from bacterial cellulose using ultrasonication and their characterization," *Carbohydrate Polymers*, vol. 191, pp. 161–167, 2018.
- [8] G. Bunget, B. Tilmon, A. Yee et al., "Novel approach of wavelet analysis for nonlinear ultrasonic measurements and fatigue," *Review of Quantitative Nondestructive Evaluation*, vol. 37, pp. 1–10, 2018.
- [9] H. Yamada, J. Yotsuji, and K. Ikushima, "Phase-sensitive detection of acoustically stimulated electromagnetic response in steel," *Japanese Journal of Applied Physics*, vol. 57, no. 7S1, p. 07LB09, 2018.
- [10] P. Zhang and S. Z. Wang, "Fast prediction of scattered sound field based on Fourier diffraction theory under second-order Born approximation," *Acoustical Physics*, vol. 60, no. 4, pp. 379–386, 2014.
- [11] M. Yamada and H. Miyakoshi, "Flow shape reconstruction by three-dimensional linearized inverse scattering method," *Review of Quantitative Nondestructive Evaluation*, vol. 25, pp. 752–759, 2006.
- [12] M. Yamada, K. Murakami, K. Nakahata, and M. Kitaharata, "Three dimensional Born and Kirchhoff inversions for shape reconstruction of defects," *Review of Quantitative Nondestructive Evaluation*, vol. 22, pp. 734–741, 2003.
- [13] G. F. Zheng, B. Wu, and C. F. He, "Shape reconstruction of mixed type void flaws using Born inversion method," *Measurement*, vol. 46, pp. 3136–3142, 2013.
- [14] H. Jin, E. Wu, Y. Han, K. Yang, and J. Chen, "Frequency domain synthetic aperture focusing technique for variable-diameter cylindrical components," *Journal of the Acoustical Society of America*, vol. 142, no. 3, pp. 1554–1562, 2017.
- [15] W. Kerr, P. Rowe, and S. G. Pierce, "Accurate 3D reconstruction of bony surfaces using ultrasonic synthetic aperture techniques for robotic knee arthroplasty," *Computerized Medical Imaging and Graphics*, vol. 58, pp. 23–32, 2017.
- [16] G. F. Zheng, B. Wu, and C. F. He, "Shape reconstruction of three-dimensional flaw from backscattering data," *Measurement*, vol. 40, no. 9-10, pp. 854–859, 2007.

## Research Article

# Optimization of Damage Equivalent Accelerated Test Spectrum Derivation Using Multiple Non-Gaussian Vibration Data

Fei Xu <sup>1</sup>, Kjell Ahlin,<sup>2</sup> and Binyi Wang<sup>3</sup>

<sup>1</sup>*School of Automotive Engineering, Yancheng Institute of Technology, Yancheng 224051, China*

<sup>2</sup>*Professor Emeritus Blekinge Tekniska Högskola, 371 79 Karlskrona, Sweden*

<sup>3</sup>*Northwest Institute of Mechanical and Electrical Engineering, Xianyang 712000 Shaanxi, China*

Correspondence should be addressed to Fei Xu; [luoyefeihen@163.com](mailto:luoyefeihen@163.com)

Received 10 July 2021; Accepted 15 August 2021; Published 6 September 2021

Academic Editor: Nan Li

Copyright © 2021 Fei Xu et al. This is an open access article distributed under the Creative Commons Attribution License, which permits unrestricted use, distribution, and reproduction in any medium, provided the original work is properly cited.

The response spectra are widely used in the damage assessment of non-Gaussian random vibration environments and the derivation of damage equivalent accelerated test spectrum. The effectiveness of the latter is strongly affected by modal parameter uncertainties, multiple field data processing, and the nonsmooth shape of the derived power spectral density (PSD). Optimization of accelerated test spectrum derivation based on dynamic parameter selection and iterative update of spectrum envelope is presented in this paper. The extreme response spectrum (ERS) envelope of the field data is firstly taken as the limiting spectrum, and the corresponding relationship between damping coefficient, fatigue exponent, and damage equivalent PSD under different test times is constructed to achieve the dynamic selection of uncertain parameters in the response spectrum model. Then, an iterative update model based on the weighted sum of fatigue damage spectrum (FDS) error is presented to reduce the error introduced by the nonsmooth shape of the derived PSD. The case study shows that undertest can be effectively avoided by the dynamic selection of model parameters. The weighted error is reduced from 80.1% to 7.5% after 7 iterations. Particularly, the error is close to 0 within the peak and valley frequency band.

## 1. Introduction

Random vibration tests are widely used to identify defects in product design and to evaluate the reliability and fatigue life of products. To simulate the mechanical environment experienced by products during their life cycle in the lab, the test spectrum is usually derived from the field measured data, which is collected using different sensors (e.g., ultrasonic transducer and accelerometer) [1]. With multiple and complicated field data, the accuracy of signal processing algorithms and data analysis methods are key factors when understanding the mechanical environment and facilitating the test spectrum derivation.

Power spectral density (PSD) is used by typical digital shaker controllers to describe the random vibration environment experienced by products, with an implicit assumption that the vibration data follows a Gaussian distribution. How-

ever, field recorded time histories, e.g., wind-induced vibration data [2] and road roughness-induced vehicle vibration data [3], usually present non-Gaussian characteristics. Since non-Gaussian (especially super-Gaussian) random vibration tends to shorten the fatigue life of products [4, 5], different vibration control methods were studied to simulate the non-Gaussian vibration environment in the lab. Steinwolf presented a phase manipulation method to simulate the non-Gaussian data [6]. In particular, the selected phase is transformed from random to deterministic in order to obtain a prescribed kurtosis. PSD and probability density function (PDF) are controlled independently. An analytical relation between kurtosis, amplitude, and phase at specific frequencies was presented later to make this method applicable in a closed-loop control [7]. From the perspective of time-varying PSD and PDF, a non-stationary non-Gaussian stochastic process simulation method based on

the zero-memory nonlinear translation relationship between non-Gaussian and Gaussian stochastic processes is proposed by Cui et al. [8]. Fei et al. [9] presented a method to synthesize non-Gaussian random vibration that is characterized by running RMS (root mean square). The essential idea is to model the non-Gaussian signal by a Gaussian signal multiplied by an amplitude modulation function (AMF). A two-parameter Weibull distribution is used to model the PDF of the running RMS and to create the AMF. Zheng et al. [10] presented a control method for multi-input multioutput stationary non-Gaussian random vibration test using time-domain randomization. The frequency-domain inverse system method is utilized to obtain the desired drive signals for dynamic inputs, and the skewness, kurtosis, and PSD of response signals are controlled efficiently and simultaneously.

The major drawback of these non-Gaussian vibration control methods, when used for fatigue life evaluation of high reliability and long-life products, is the long test time and high cost. To address this problem, the response spectrum method was utilized to evaluate the potential damage introduced by the vibration environment. An accelerated test spectrum was then synthesized from the response spectra based on the damage equivalence criterion [11–13]. To perform life cycle potential damage assessment and test tailoring, Lalanne [14] derived an equivalent PSD from multiple task profiles based on the frequency domain fatigue damage spectrum (FDS). Wijker [15] and Decker et al. [16] derived the accelerated test spectrum based on the extreme response spectrum (ERS). The effect of parameter uncertainties (damping coefficient and fatigue exponent) on the root mean square (RMS) value of the derived PSD was studied. Steinwolf and Wolfsteiner [17] indicated that to avoid changes in the failure mechanism and dynamic properties of products, the ERS of field data should be used to limit the accelerated PSD level. Xu et al. [18] showed that the FDS of non-Gaussian field data increases as the kurtosis increases. A significant error would be introduced if FDS and ERS were calculated in the frequency domain directly using PSD. Ahlin [19] calculated FDS and ERS in time domain using the ramp invariant digital filter method. Due to the low computational efficiency of FDS in the time domain, Wolfsteiner [20] decomposed the non-Gaussian load into a combination of Gaussian loads, so that the frequency domain method can be used to improve the computational efficiency. Assuming that the synthesized equivalent PSD is flat within the half-power bandwidth, Cianetti et al. [21] presented the equivalent PSD synthesis method for non-Gaussian data using FDS and Mile's Equation. These existing methods have demonstrated how to derive the equivalent accelerated test spectrum from a single set of non-Gaussian data and analyzed the influence of parameter uncertainties on the RMS value of test spectrum. However, how to select the correct model parameters using multiple non-Gaussian vibration data, so as to derive the equivalent accelerated test spectrum which can effectively avoid undertest, has not been studied. In addition, how to construct the objective function, so as to rapidly reduce the

error introduced by nonsmooth shape of the synthesized PSD, has not been demonstrated. To address these problems, an optimization design procedure of test spectrum derivation based on dynamic parameter selection and iterative spectrum envelope update technique is presented in this paper.

The remainder of the paper is organized as follows. Section 2 introduces the definition of Gaussian random vibration, non-Gaussian random vibration, FDS, and ERS. The optimized accelerated test spectrum derivation procedure is also presented. In Section 3, validation with field measured non-Gaussian vibration data is presented. Finally, the discussion and conclusions are summarized in Section 4.

## 2. Materials and Methods

**2.1. Gaussian and Non-Gaussian Random Vibration.** For the field measured discrete random vibration signal  $x(t)$ , the higher-order moments can be used to determine if it follows the Gaussian distribution:

$$m_n = \int_{-\infty}^{\infty} x^n p(x) dx = \frac{1}{N} \sum_{j=1}^N x_j^n, \quad (1)$$

where  $m_n$  is the  $n$ th order moments,  $p(x)$  is the probability density function (PDF), and  $N$  is the number of signals.

When the mean value is zero,

$$S = \frac{1}{N} \sum_{j=1}^N \frac{x_j^3}{\sigma_x^3} = \frac{m_3}{\sigma_x^3}, \quad (2)$$

$$K = \frac{1}{N} \sum_{j=1}^N \frac{x_j^4}{\sigma_x^4} = \frac{m_4}{\sigma_x^4},$$

where  $S$  is the skewness,  $K$  is the kurtosis, and  $\sigma_x$  is the root mean square (RMS) of  $x(t)$ .

For a Gaussian distributed signal, the skewness is 0 and the kurtosis is 3. Deviation from these values indicates that the signal follows a non-Gaussian distribution. From the perspective of response spectrum calculation of a non-Gaussian signal, kurtosis is more important than skewness, since it represents the probability of peak values in time history [22].

**2.2. Fatigue Damage Spectrum (FDS) and Extreme Response Spectrum (ERS).** The FDS and ERS are widely used response spectra for evaluating potential damage under random vibration environment. The FDS is essentially a plot that shows the response of a series of single-degree-of-freedom (SDOF) systems to the base input acceleration time history. Many SDOF systems tuned to a range of natural frequencies are assessed using the same input. The FDS shows the fatigue damage encountered for a particular SDOF system anywhere within the analyzed time. It has been shown that the stress is roughly proportional to pseudovelocity [23]. For a SDOF system with a natural frequency  $f_n$  and a damping ratio  $\xi$ , the output pseudovelocity  $x_{pv}$  to an input

acceleration  $x_a$  can be calculated using a ramp invariant digital filter method [19]:

$$\begin{aligned}
 x_{pv} &= F_{\text{filter}}(b, a, x_a), \\
 a &= [1, -2C, E^2], \\
 b &= \frac{-1}{w2\pi f_n} \left[ \frac{C-1}{Q} + qS + w, -2Cw + \frac{1-E^2}{Q} - 2qS, E^2 \left( w + \frac{1}{Q} \right) - \frac{C}{Q} + qS \right], \\
 w &= \frac{2\pi f_n}{f_s}, \\
 Q &= \frac{1}{2\zeta}, \\
 k_1 &= \sqrt{1 - \frac{1}{4Q^2}}, \\
 k_2 &= \frac{\pi}{Qf_s}, \\
 k_3 &= \frac{2\pi}{f_s} k_1, \\
 q &= \frac{(1/2/Q/Q - 1)}{k_1}, \\
 A &= k_2 f_n, \\
 B &= k_3 f_n, \\
 E &= \exp(-A), \\
 C &= E \cos(B), \\
 S &= E \sin(B),
 \end{aligned} \tag{3}$$

where  $f_s$  is the sampling frequency and  $F_{\text{filter}}$  indicates filtering the input signal with a ramp invariant digital filter.

With the output  $x_{pv}$ , the cumulative damage can be calculated in both time domain and frequency domain. In time domain, the rain flow cycle counting method is usually used for stress cycle counting. With cyclic numbers of different stress levels, the S-N curve and Miner's rule are combined to calculate the fatigue damage as follows [24]:

$$\begin{aligned}
 N_i &= cS_i^{-b}, \\
 D_t &= \sum_{i=1}^p n_i/N_i = \sum_{i=1}^p n_i k^b x_{pv,i}^b / c = k^b / c * \sum_{i=1}^p n_i x_{pv,i}^b,
 \end{aligned} \tag{4}$$

where  $N_i$  is the fatigue life at stress  $S_i$  ( $i = 1, 2, \dots, p$ ),  $p$  is the number of stress levels considered,  $n_i$  is the number of cycle exposure at  $S_i$ ,  $c$  is a constant,  $b$  is the fatigue exponent,  $k$  is the proportional coefficient of stress to pseudovelocity,  $D_t$  is the total damage index calculated in time domain, and  $x_{pv,i}$  is the output pseudovelocity at  $i$ th cycle.

In the frequency domain, Rayleigh distribution of response stress maxima is assumed and used to calculate



FIGURE 1: Test item.

the stress cycles:

$$p(S) = \frac{S}{\sigma_s^2} e^{-S^2/2\sigma_s^2}, \tag{5}$$

where  $S$  is the stress value of peaks and  $\sigma_s$  is the RMS of the stress time history.

The total damage can be calculated as

$$D_f = \frac{f_n T}{c} \int_0^{+\infty} p(S) S^b dS, \tag{6}$$

where  $T$  is the total time of exposure to the stress environment.

Substituting Equation (5) into Equation (6) leads to

$$D_f = \frac{f_n T}{c} k^b \left( 2\sigma_{pv}^2 \right)^{b/2} \Gamma \left( 1 + \frac{b}{2} \right), \tag{7}$$

where  $\Gamma$  is the gamma function and  $\sigma_{pv}$  is the RMS of pseudovelocity.

The RMS of pseudovelocity can be calculated using

$$\sigma_{pv} = \sqrt{\sum_{f=f_{\text{low}}}^{f=f_{\text{hi}}} (|H(f)|^2 * G_{xx}(f)) * df}, \tag{8}$$

where  $H(f)$  is the transmissibility of a SDOF system (pseudovelocity/acceleration),  $G_{xx}(f)$  is the input PSD,  $f_{\text{low}}$  is the lower limit, and  $f_{\text{hi}}$  is the higher limit.

If the input PSD is relatively flat in the half-power bandwidth of each SDOF system, then Mile's Equation can be used to calculate  $\sigma_{pv}$  in a closed form approximately as follows:

$$\sigma_{pv} = \sqrt{\frac{G_{xx}(f_n) Q}{8\pi f_n}}. \tag{9}$$

With Equations (7) and (9), the PSD at each natural frequency can be derived from the FDS at the corresponding



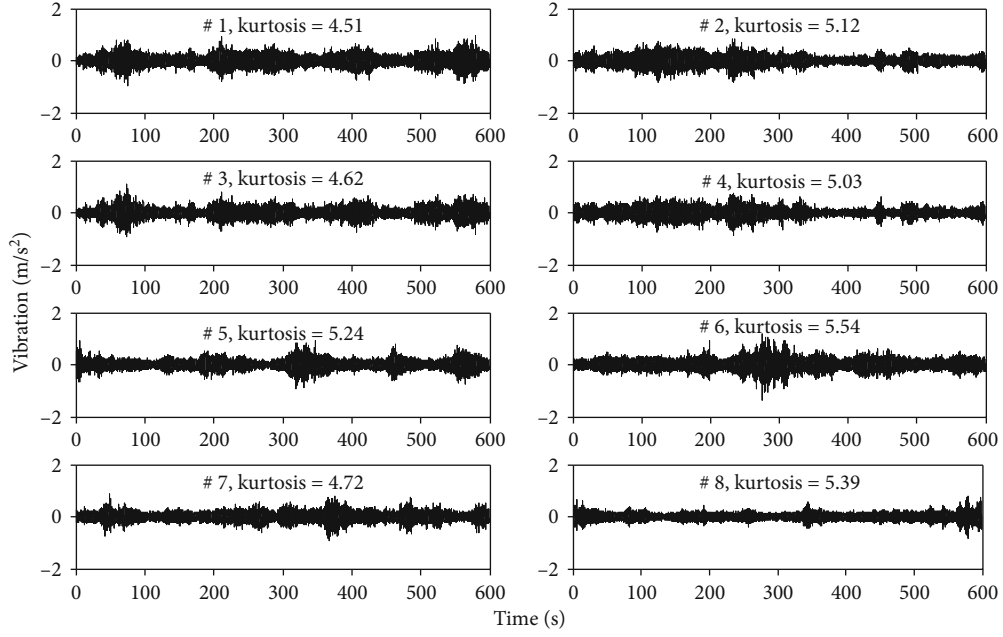


FIGURE 2: Field measured non-Gaussian signal induced by wind.

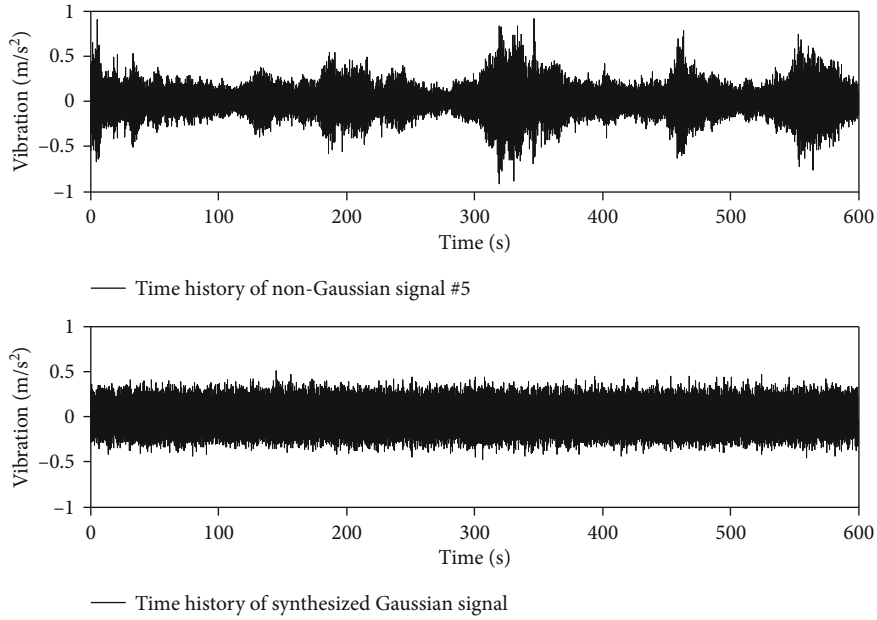


FIGURE 3: Comparison of time history between the measured non-Gaussian signal and the synthesized Gaussian signal.

natural frequency:

$$G_{xx}(f_n) = \left( \frac{D(f_n)}{\Gamma(1 + b/2)f_n T} \right)^{2/b} \frac{4\pi f_n}{Q}. \quad (10)$$

Note that if the flat PSD assumption does not hold around some natural frequencies, the FDS calculated with Equations (7) and (8) using the derived PSD in Equation (10) will deviate from the FDS calculated with Equations

(7) and (9). In such case, an iterative update procedure is needed to take the shape of PSD into account (see Section 4).

The ERS shows the damage caused by vibration from an overstress viewpoint. Like the FDS, the ERS is essentially a plot that shows the responses of a number of SDOF systems to a base input acceleration time history. The only difference is that the ERS is generated by calculating the maximum response of a SDOF system to the input. The final plot, the ERS, shows the largest response encountered for a particular SDOF system anywhere within the analyzed time. For a

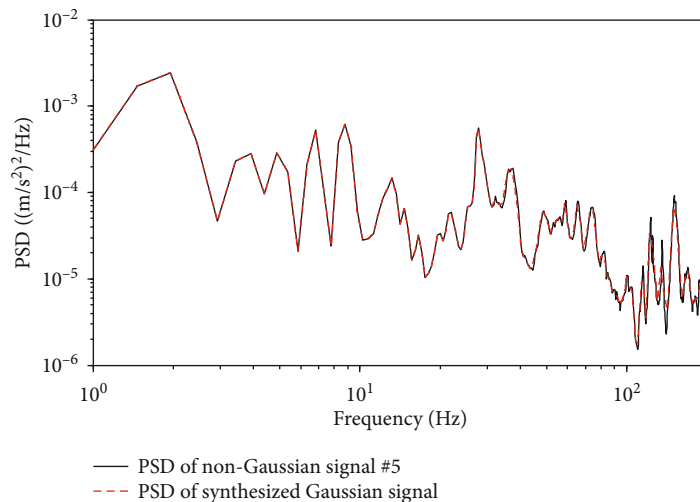


FIGURE 4: Comparison of PSD between the measured non-Gaussian signal and the synthesized Gaussian signal.

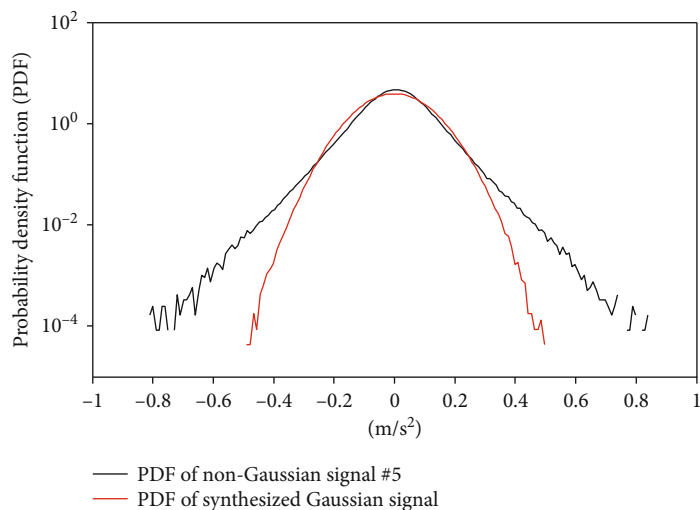


FIGURE 5: Comparison of PDF between the measured non-Gaussian signal and the synthesized Gaussian signal.

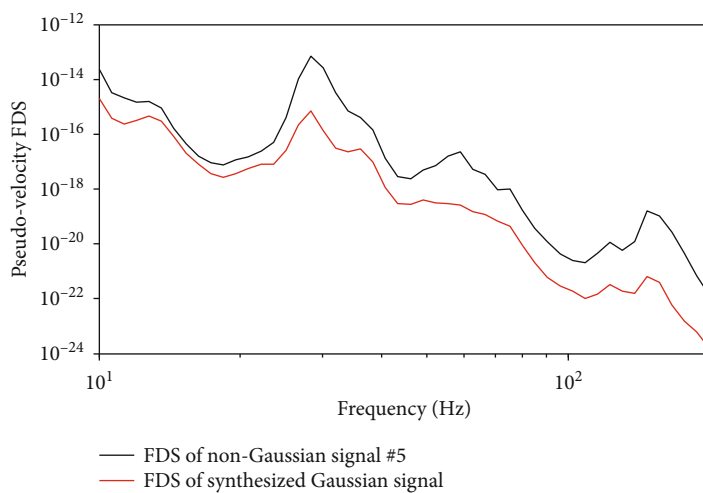


FIGURE 6: Comparison of FDS between the measured non-Gaussian signal and the synthesized Gaussian signal.

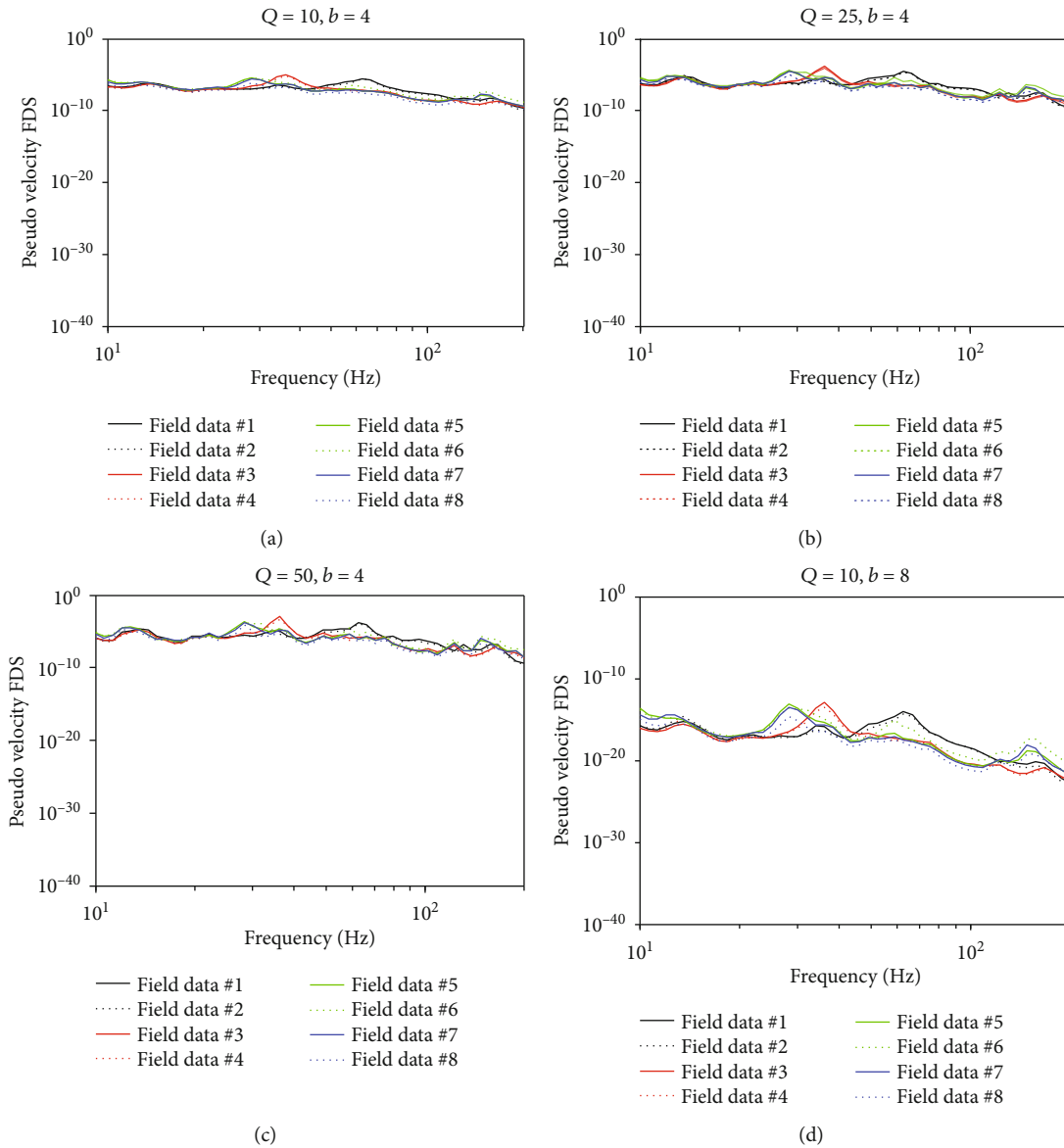


FIGURE 7: Continued.

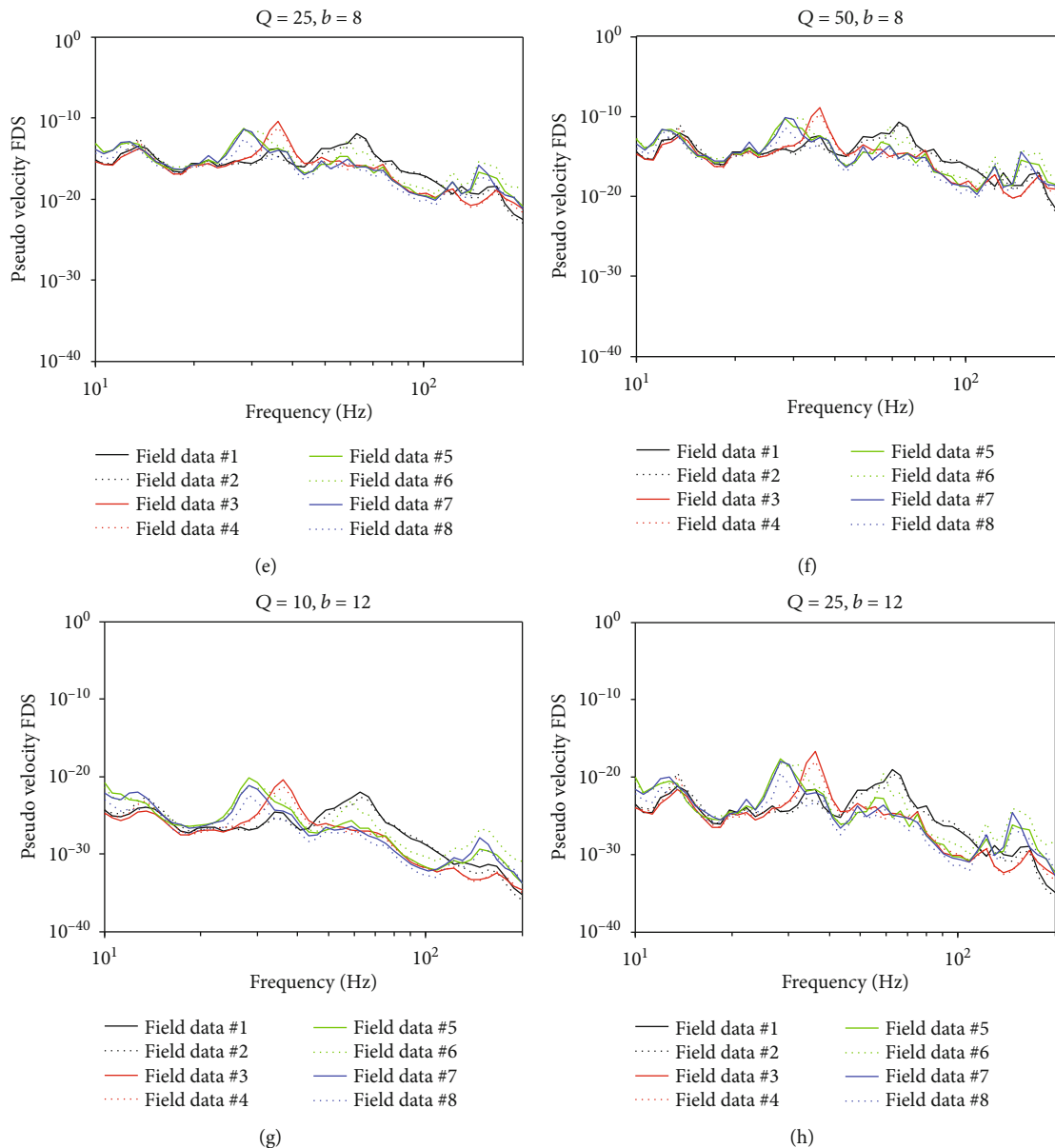


FIGURE 7: Continued.

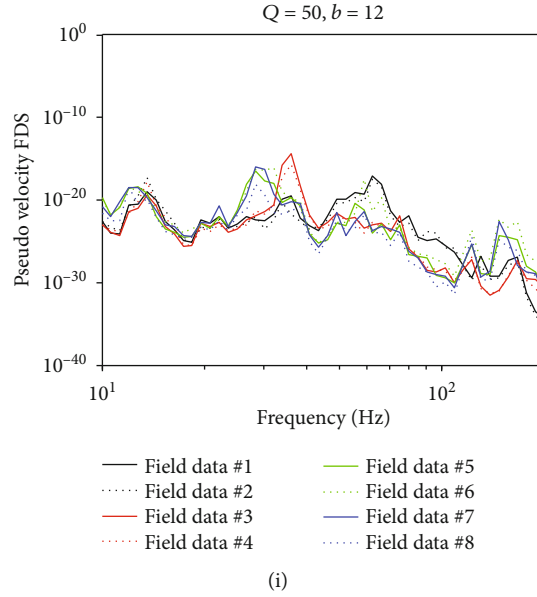


FIGURE 7: FDS of measured wind load under different  $Q$  and  $b$  values: (a)  $Q = 10, b = 4$ ; (b)  $Q = 25, b = 4$ ; (c)  $Q = 50, b = 4$ ; (d)  $Q = 10, b = 8$ ; (e)  $Q = 25, b = 8$ ; (f)  $Q = 50, b = 8$ ; (g)  $Q = 10, b = 12$ ; (h)  $Q = 25, b = 12$ ; (i)  $Q = 50, b = 12$ .

SDOF system with a natural frequency  $f_n$  and a damping ratio  $\xi$ , the ERS can also be calculated in both time domain and frequency domain as follows [14]:

$$ERS_t = \max (F_{\text{filter}}(b, a, x_a)), \quad (11)$$

$$ERS_f = \left( \sqrt{2 \ln f_n * T} + \frac{0.577}{\sqrt{2 \ln f_n * T}} \right) * \sqrt{\sum_{f=f_{\text{low}}}^{f=f_{\text{hi}}} (H(f)^2 * G_{xx}(f)) * df}. \quad (12)$$

2.3. *Derivation of Damage Equivalent Accelerated Test Spectrum.* Since the accuracy of the damage equivalent accelerated test spectrum is strongly affected by uncertain parameters, dispersion of multiple non-Gaussian samples, and the smoothness of the derived PSD, an optimum design procedure is presented as follows:

- (1) Calculate the FDS of multiple samples in time domain and take the envelope using different damping ratios (denoted by quality factor  $Q$ ) and fatigue exponent  $b$
- (2) Predetermine the accelerated test time, and synthesize the initial PSD using the FDS envelope and Equation (10)
- (3) Choose  $Q$  and  $b$  in a dynamic way, so that the most conservative PSD is derived
- (4) Calculate the FDS in the frequency domain using the derived PSD, Equation (7), and Equation (8)

- (5) Compare the calculated FDS in Step (1) and Step (4), and define the weighted sum of FDS errors:

$$W_{\text{error}} = \sum_{f_i=f_{\text{lowest}}}^{f_{\text{highest}}} \left[ \left| \frac{D_{\text{num}}(f_n) - D_{\text{env}}(f_n)}{D_{\text{env}}(f_n)} \right| * 100 * \frac{D_{\text{env}}(f_n)}{\sum_{f_i=f_{\text{lowest}}}^{f_{\text{highest}}} D_{\text{env}}(f_n)} \right], \quad (13)$$

where  $f_{\text{lowest}}$  is the lowest natural frequency,  $f_{\text{highest}}$  is the highest natural frequency,  $D_{\text{env}}(f_n)$  is the FDS envelope calculated in Step (1), and  $D_{\text{num}}(f_n)$  is the FDS calculated in Step (4)

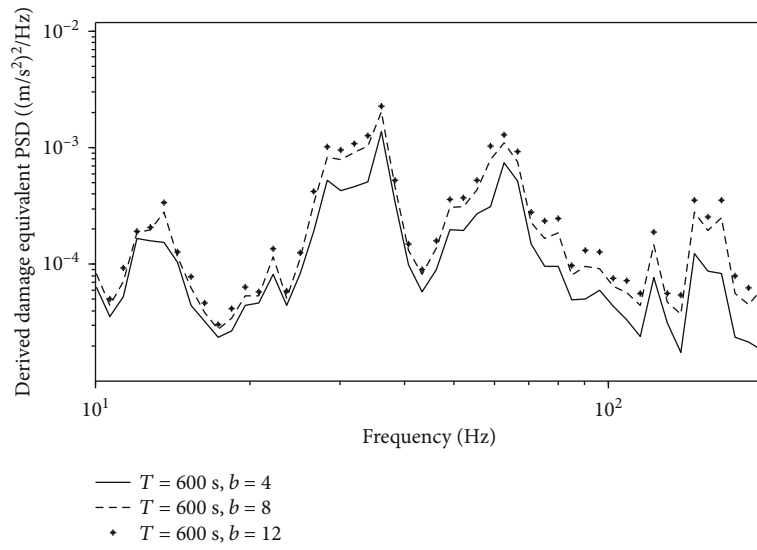
- (6) Update the PSD in Step (3) until a certain error is reached:

$$G_{m+1}(f_n) = G_m(f_n) * \left( \frac{D_{\text{env}}(f_n)}{D_{\text{num}}(f_n)} \right)^{2/b}, \quad (14)$$

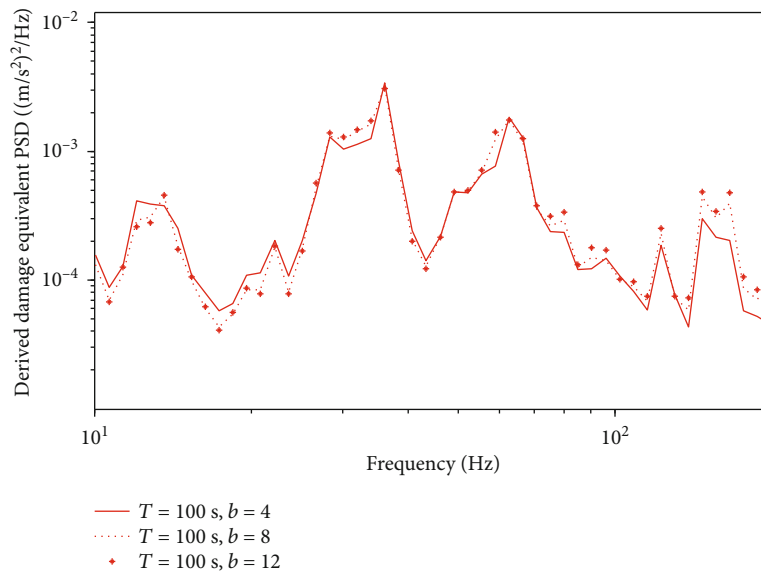
where  $G_m(f_n)$  is the damage equivalent PSD after  $m$  iterations

- (7) Calculate the ERS in frequency domain using the updated PSD and Equation (12) and compare with the ERS envelope calculated in time domain
- (8) Update the predetermined test time and PSD level to match both the FDS and ERS envelope of the field data





(a)



(b)

FIGURE 8: Continued.

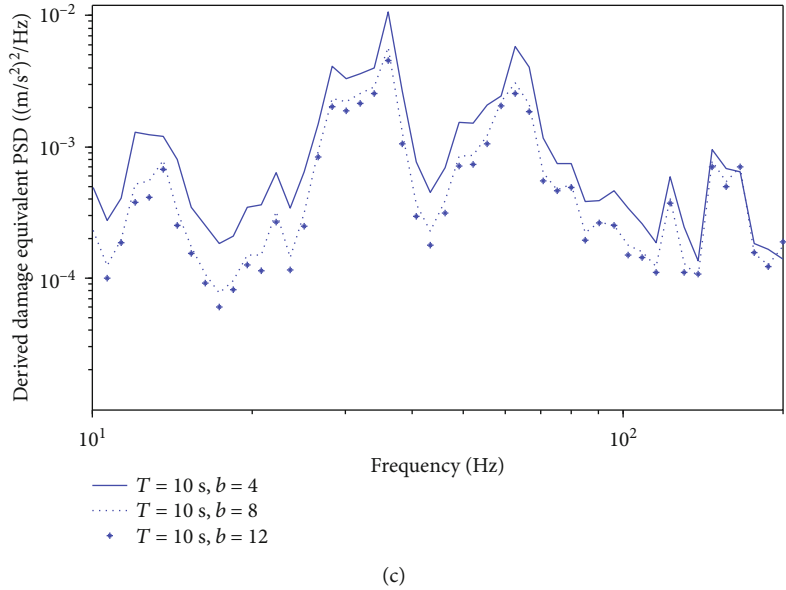


FIGURE 8: Equivalent PSD under different test times with different values of  $b$ : (a) test time 600 s; (b) test time 100 s; (c) test time 10s.

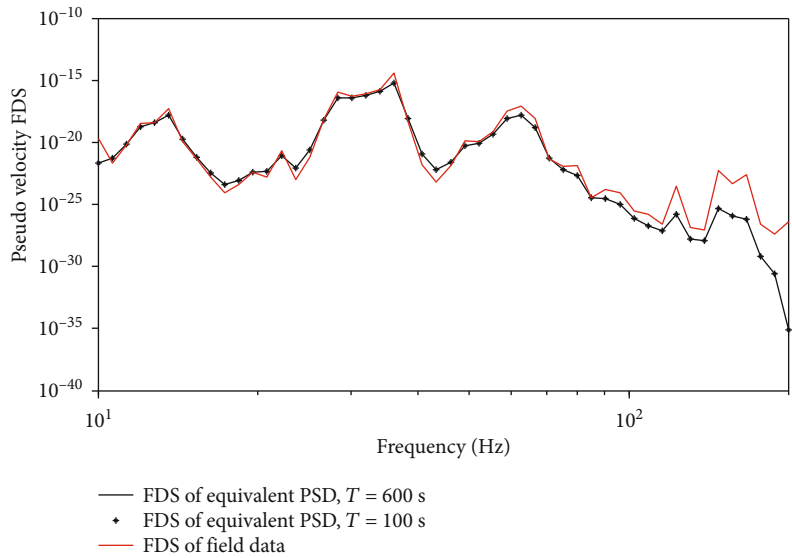


FIGURE 9: Comparison of FDS between field data and equivalent PSD before correction.

### 3. Results and Discussion

3.1. Case Study. Field measured non-Gaussian data are used to demonstrate the procedure in Section 4. The field data is from an Ericsson Mast Project. The random acceleration signal induced by wind is taken from a test item installed on a mast, as shown in Figure 1. The test item is a standard Ericsson Micro Radio Base equipment, manufactured in cast lightweight alloy with integrated heat sinks, equipped with B&K WB0179 triaxial accelerometer sets and a wind speed measuring device. The dimensions are 530 \* 400 \* 185 mm, and the weight is about 21 kg. The back side of the box was mounted to the mast at a height of 50 meters.

Acceleration signals were collected using 8 channels, as shown in Figure 2. From Figure 2, we can see that the kurtosis of each signal is greater than 3, indicating the non-Gaussianity. To show the error introduced by direct calculation of PSD from the non-Gaussian signal, the data collected from channel 5 is used here as an example. The PSD is calculated, and the Gaussian signal is synthesized, as shown in Figure 3. The PSD and the PDF are compared between the field data and the synthesized Gaussian signal, as shown in Figures 4 and 5, respectively. From Figures 4 and 5, we can see that the PDF of the field data is clearly different from that of the synthesized Gaussian signal, although the PSD are basically the same. The pseudovelocity FDS of the measured

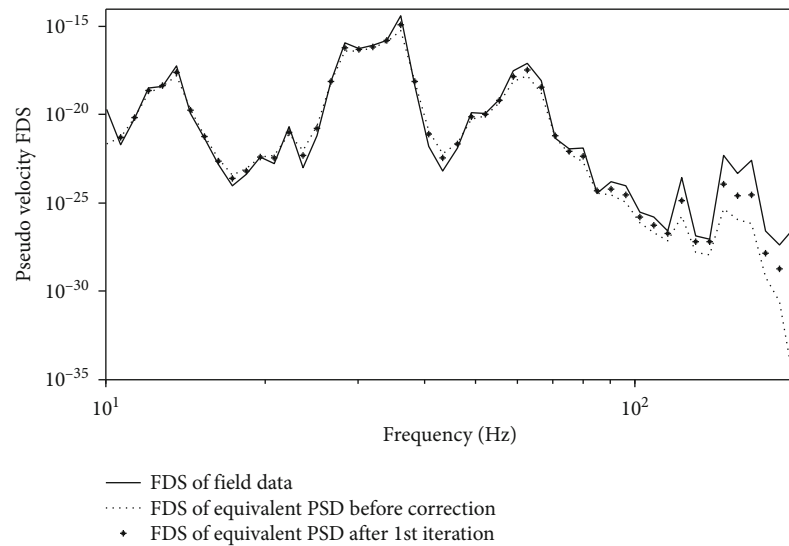


FIGURE 10: Comparison of FDS between field data and equivalent PSD before and after the first correction.

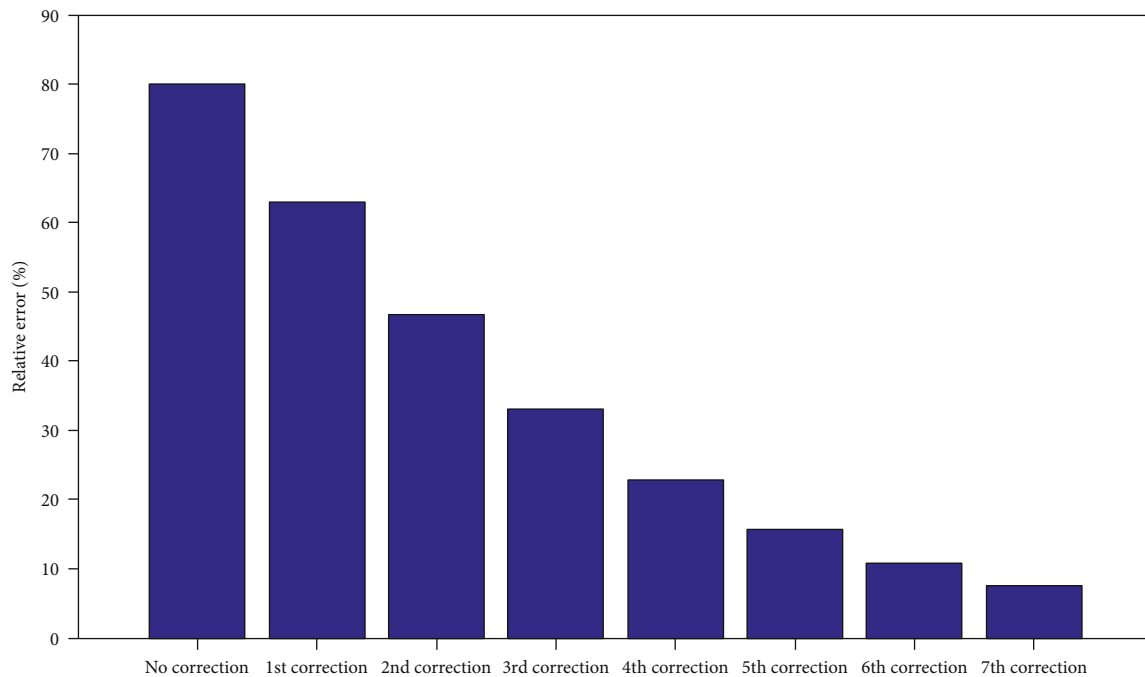


FIGURE 11: FDS error analysis before and after correction.

non-Gaussian signal is significantly higher than that of the synthesized Gaussian load, as shown in Figure 6. From Figures 3–6, we can see that the direct calculation of PSD from a non-Gaussian signal will lead to an obvious undertest.

To determine the effects of damping ratio and fatigue exponent on the calculation of response spectra and PSD synthesis, the pseudovelocity FDS of field data were calculated with different values of  $Q$  (10, 25, 50) and  $b$  (4, 8, 12), as shown in Figure 7. From Figure 7, we can see that the FDS decreases and the dispersion increases, as the value of  $b$  increases. The value of  $Q$  has little effects on FDS (compared with the effect of  $b$ ).

Set the value of  $Q$  to 50, calculate FDS with different values of  $b$ , and take the envelope. The equivalent PSD under different test times ( $T = 600$  s, 100 s, 10 s) are derived using the FDS envelope and Equation (10), as shown in Figure 8. From Figure 8, we can see that the equivalent PSD level increases as the test time decreases. The effects of the value of  $b$  on the equivalent PSD depend on the predetermined accelerated test time. With  $T$  equals to 600 s (not accelerated), the equivalent PSD increases as the value of  $b$  increases. With  $T$  equals to 100 s, the value of  $b$  has little effect on the equivalent PSD. With  $T$  equals to 10 s, however, the equivalent PSD decreases as the value of  $b$  increases.

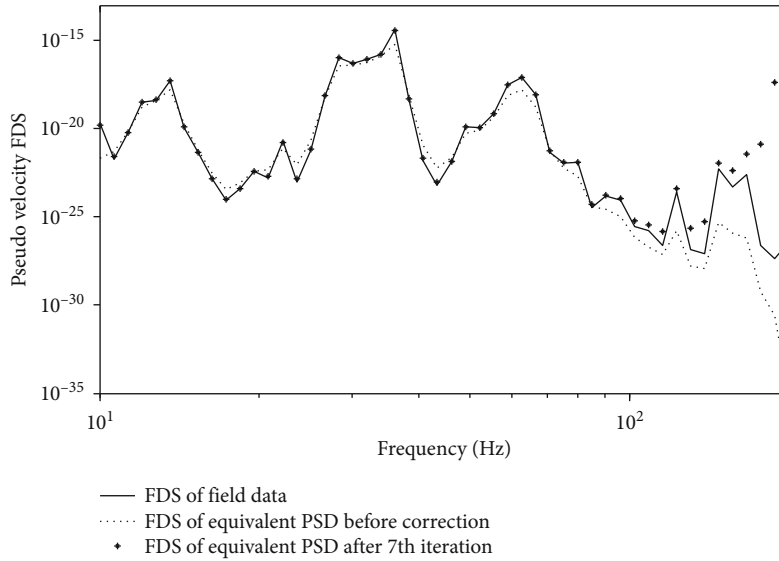


FIGURE 12: Comparison of FDS between field data and equivalent PSD before and after the 7th correction.

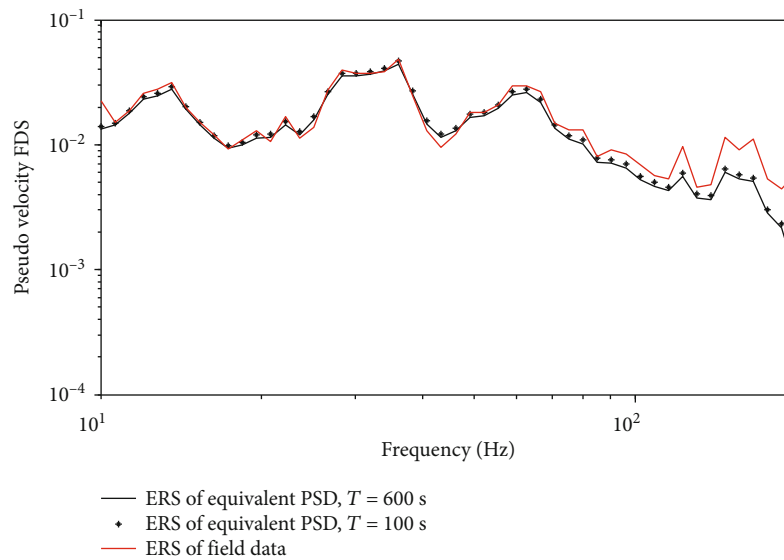


FIGURE 13: Comparison of ERS between equivalent PSD and field data.

The FDS of equivalent PSD for different test times remain the same, as shown in Figure 9. A comparison is made between the FDS of equivalent PSD and non-Gaussian field data. Due to the nonsmooth shape of the equivalent PSD, the mismatch is clearly seen, especially within the peak and valley frequency band. To account for the nonsmooth shape, the PSD is updated using Equation (14). A better match between the FDS of the field data and the equivalent PSD is reached after the first iteration, as shown in Figure 10.

The weighted sum of FDS error (see Equation (13)) calculated from the field data and equivalent PSD is reduced from 80.1% to 7.5% after 7 iterations. Particularly, the error is close to 0 within the peak and valley frequency band, as

shown in Figures 11 and 12. The deviation of PSD between 150 Hz and 200 Hz is trivial due to the low level.

A good match between the ERS calculated from the equivalent PSD and that calculated from the field data is shown in Figure 13. Note that although the PSD level can be further increased to reduce the test time, the test item may fail due to the peak response which will not be experienced in the field.

#### 4. Conclusions

Considering the effects of dispersion of field data, parameter uncertainties, and the nonsmooth shape of the PSD, on the accuracy of the derived damage equivalent accelerated test

spectrum, an optimized procedure for PSD synthesis using non-Gaussian data is presented in this paper. Conclusions are as follows:

- (1) Direct calculation of PSD from non-Gaussian field data leads to undertest. The envelope of FDS and ERS can be used to derive the damage equivalent PSD, considering the dispersion of multiple non-Gaussian field data
- (2) Model parameters must be selected dynamically if a priori information is unknown, i.e., the selection of model parameters depends on the predetermined accelerated test time, so as to avoid undertest
- (3) The damage equivalent PSD must be updated to account for its nonsmooth shape. The weighted sum of FDS error between field data and derived PSD can be reduced dramatically after only a few iterations. Particularly, the error can be reduced close to 0 within the peak and valley frequency band

## Data Availability

The (MATLAB data file “field data0707.mat”) data used to support the findings of this study are available from the corresponding author upon request.

## Conflicts of Interest

The authors declare that there is no conflict of interest regarding the publication of this paper.

## Acknowledgments

This research activity was partially supported by the National Natural Science Foundation of China (Grant No. 52102443) and a project (No. xjr2019036) entitled funding for school-level research projects of Yancheng Institute of Technology.

## References

- [1] N. Li, J. Sun, J. Jiao, B. Wu, and C. He, “Quantitative evaluation of micro-cracks using nonlinear ultrasonic modulation method,” *Ndt & E International*, vol. 79, pp. 63–72, 2016.
- [2] Y. Hui, B. Li, H. Kawai, and Q. Yang, “Non-stationary and non-Gaussian characteristics of wind speeds,” *Wind and Structures*, vol. 24, no. 1, pp. 59–78, 2017.
- [3] A. Steinwolf, “Vibration testing of vehicle components by random excitations with increased kurtosis,” *International Journal of Vehicle Noise and Vibration*, vol. 11, no. 1, pp. 39–66, 2015.
- [4] M. Palmieri, M. Česnik, J. Slavič, F. Cianetti, and M. Boltežar, “Non-Gaussianity and non-stationarity in vibration fatigue,” *International Journal of Fatigue*, vol. 97, pp. 9–19, 2017.
- [5] A. Niesłony, M. Bohm, T. Łagoda, and F. Cianetti, “The use of spectral method for fatigue life assessment for non-Gaussian random loads,” *acta mechanica et automatica*, vol. 10, no. 2, pp. 100–103, 2016.
- [6] A. Steinwolf, “Random vibration testing with kurtosis control by IFFT phase manipulation,” *Mechanical Systems and Signal Processing*, vol. 28, pp. 561–573, 2012.
- [7] J. Zhang, B. Cornelis, B. Peeters, K. Janssens, and P. Guillaume, “A new practical and intuitive method for kurtosis control in random vibration testing,” in *Proceedings of ISMA 2016 - International Conference on Noise and Vibration Engineering and USD 2016- International Conference on Uncertainty in Structural Dynamics*, Leuven, Belgium, 2016.
- [8] S. Cui, E. Zheng, and M. Kang, “A time-domain procedure for non-Gaussian stationary environmental testing using zero-memory nonlinear transformation,” *Journal of Vibration and Control*, vol. 26, no. 15-16, pp. 1197–1213, 2020.
- [9] X. Fei, L. Chuanri, J. Tongmin, and K. Ahlin, “Synthesis of running RMS-induced non-Gaussian random vibration based on Weibull distribution,” *Journal of Vibroengineering*, vol. 17, no. 7, pp. 3662–3674, 2015.
- [10] R. Zheng, H. Chen, D. Vandepitte, and Z. Luo, “Multi-exciter stationary non-Gaussian random vibration test with time domain randomization,” *Mechanical systems and signal processing*, vol. 122, pp. 103–116, 2019.
- [11] A. Angeli, B. Cornelis, and M. Troncosi, “Synthesis of Sine-on-Random vibration profiles for accelerated life tests based on fatigue damage spectrum equivalence,” *Mechanical systems and signal processing*, vol. 103, pp. 340–351, 2018.
- [12] F. Cianetti, A. Alvino, A. Bolognini, M. Palmieri, and C. Braccesi, “On field durability tests of mechanical systems. The use of the Fatigue Damage Spectrum,” *Procedia Structural Integrity*, vol. 3, pp. 176–190, 2017.
- [13] M. Bonato and D. Delaux, “Synthesis and validation of accelerated vibration durability tests for engine mounted components,” *Applied Reliability Durability Conference, Europe*, 2018.
- [14] C. Lalanne, *Mechanical Vibration and Shock Analysis—Volume 5: Specification Development*, John Wiley & Sons, Inc-ISTE, London, 3rd ed. edition, 2014.
- [15] J. Wijker, M. Ellenbroek, and A. D. Boer, “Characterization and synthesis of random acceleration vibration specifications,” in *4th International Conference on Computational Methods in Structural Dynamics & Earthquake Engineering*, pp. 101–130, Kos Island, Greece, 2013.
- [16] M. Decker, S. Kinscherf, N. Bauer, P. David, and M. Serifsoy, “Deriving fatigue equivalent power spectral density spectra for the vibration testing of engine components,” *Material Science and Engineering Technology*, vol. 49, no. 3, pp. 392–405, 2018.
- [17] A. Steinwolf and P. Wolfsteiner, “Vibration testing of vehicle components by fatigue damage spectrum control,” *International Journal of Vehicle Noise and Vibration*, vol. 15, no. 2/3, pp. 133–153, 2019.
- [18] F. Xu, C. Li, and T. Jiang, “On the shaker simulation of wind-induced non-Gaussian random vibration,” *Shock and Vibration*, vol. 2016, Article ID 5450865, 10 pages, 2016.
- [19] K. Ahlin, “Comparison of test specifications and measured field data,” *Sound and Vibration*, vol. 40, no. 9, pp. 22–25, 2006.
- [20] P. Wolfsteiner, “Fatigue assessment of non-stationary random vibrations by using decomposition in Gaussian portions,” *International Journal of Mechanical Sciences*, vol. 127, pp. 10–22, 2017.



- [21] F. Cianetti, A. Alvino, A. Bolognini, M. Palmieri, and C. Braccesi, "The design of durability tests by fatigue damage spectrum approach," *The design of durability tests by fatigue damage spectrum approach. Fatigue and Fracture of Engineering Materials and Structures*, vol. 41, no. 4, pp. 787–796, 2018.
- [22] P. V. Baren, "The missing knob on your random vibration controller," *Sound & vibration*, vol. 39, no. 10, pp. 10–16, 2005.
- [23] H. A. Gaberson, "Shock severity estimation," *Sound and Vibration*, vol. 46, no. 1, pp. 12–20, 2012.
- [24] G. R. Henderson and A. G. Piersol, "Fatigue damage related descriptor for random vibration test environments," *Sound and Vibration*, vol. 29, no. 10, pp. 20–24, 1995.